DEVELOPMENT OF A DYNAMIC MODEL FOR PIEZOELECTRIC RAINDROP ENERGY HARVESTING

by

WONG VOON KEAN, B.Eng(Hons)

Thesis submitted to the University of Nottingham
for the degree of Doctor of Philosophy

Feb 2017

Declaration of Authorship

I, Wong Voon Kean, hereby declare that this submission is my own work and that it has not been submitted previously for any other degree. To the best of my knowledge and belief, it contains no material previously published or written by another person, except where information reference is made.

Wong Voon Kean

23 FEB 2017

Abstract

Over the last decade, advancement of microelectronics has triggered a growing interest in ambient energy harvesting. Ambient energy can be found in various forms such as: thermoelectric, acoustic, solar, and mechanical vibrations. Most of the stated ambient energy sources have been thoroughly investigated. One of the relatively unexplored ambient energy sources is raindrop impact energy. Raindrop impact energy harvesting is achieved by converting the strain induced by an impinging raindrop on a piezoelectric beam into usable electrical energy. Most of the conducted research from the literature only considered single droplet impact on a piezoelectric beam. More interestingly, actual field test has yet to be conducted. These are the areas that the research will cover.

A commercial piezoelectric beam (Mide-v25w) is utilised for this research. In this work, the piezoelectric beam is modelled as a distributed parameter system. To describe the post impact behaviours and water layer formed on the piezoelectric beam, impact coefficient and added mass coefficient are introduced for respective cases. Excitation models for single droplet, multiple droplet, artificial rain, and actual rain are developed. The models presented here were validated via experimental results. A hybrid

bridge rectifier is designed and tested under actual rain. Experiment results showed that the half bridge rectifier is able to produce 95.12 % more energy than the full bridge rectifier during low voltage operation.

From the actual rain experiment, the raindrop impact energy harvester was able to produce 1564 μJ energy over a rain period of 3539 s. The maximum instantaneous power generated by the piezoelectric was found to be 3.75 mW. This is higher compared the highest instantaneous power recorded in the literatures, which was 23 μW.

List of publications

To date, publications originated from this work are listed below:

1. V.-K. Wong, J.-H. Ho and E.H. Yap. Experimental study of a piezoelectric rain energy harvester, Advanced Materials Research, 1043:263-267, 2014.

2. V.-K. Wong, J.-H. Ho and E.H. Yap. Dynamics of a piezoelectric beam subjected to water droplet impact with water layer formed on the surface, Journal of Intelligent Material Systems and Structures, 26(10):2170-2180, 2015.

3. V.-K. Wong, J.-H. Ho and A.-B. Chai. Piezoelectric energy harvesting in varying simulated rain conditions, ARPN Journal of Engineering and Applied Sciences. 11(1):110-114, 2016.

4. V.-K. Wong, J.-H. Ho and H.-K. Sam. On accumulation of water droplets in piezoelectric energy harvesting, Journal of Intelligent Material Systems and Structures. 1045389X16649702, 2016.

5. Z.-Z. Ong, V.-K. Wong and J.-H. Ho. Performance enhancement of a piezoelectric rain energy harvester Sensors and Actuators A: Physical. 252:154-164, 2016.

6. V.-K. Wong, J.-H. Ho and A.-B. Chai. Performance of a piezoelectric energy harvester in actual rain (accepted), ENERGY, 2017.

7. V.-K. Wong, J.-H. Ho, E.H. Yap and A.-B. Chai. Dynamics of a piezoelectric energy harvester in a simulated rain environment (submitted), Journal of Mechanical Engineering Science, 2017.

Acknowledgements

First and foremost, I offer my deepest gratitude to my supervisor, Dr. Ho Jee Hou, who has given me continually support and motivation throughout the research. It is with his patience and knowledge, I am given space and freedom to conduct the research in my own way. I would also like to express my appreciation to my Co-supervisor, Dr. Chai Ai Bao, for her inspirational comments on my work. I am very grateful to be given an opportunity to work with them.

Advices from Dr. Yap Eng Hwa, and Dr. Stewart McWilliam of the University of Nottingham Malaysia Campus are greatly appreciated. I would also wish to thank Dr. Cosmas Pandit Pagwiwoko for the insightful yearly review discussions. Their experience and expertise have greatly assisted me throughout the project.

I would like to thank the Ministry of Higher Education, Malaysia for the funding of this project under the Exploratory Research Grant Scheme and MyBrain15 Scholarship.

To all my friends who in one way or another shared their love and support, thank you. Without you, the journey of completing this dissertation would not be as joyful and pleasant. A special thank you to Mr. Chai Tong Yuen, who has given me moral support and advice, both personally and professionally.

Above all, I am greatly indebted to my family members, especially my Father and Mother. I am thankful for their endless love and support. Thank you for everything you have done for me over the years.

Contents

Declaration of Authorship **i**

Abstract **ii**

List of publications **iv**

Acknowledgements **vi**

List of Figures **xi**

List of Tables **xv**

Nomenclature **xvi**

Abbreviations **xxiv**

1 Introduction **1**
1.1 Background 1
1.2 Overview of piezoelectric energy harvesting 3
1.3 Motivation 6
1.4 Aim and Objectives 12
1.5 Summary of original contributions 13
1.6 Thesis overview 16

2 Mathematical modelling of the piezoelectric beam **18**
2.1 Introduction 18
2.2 Modal Analysis of a piezoelectric cantilever beam 20
2.2.1 Derivation of cantilever beam mode shape 20
2.2.2 Normalisation of mode shape 22
2.3 Modelling of the piezoelectric beam 23
2.3.1 Constitutive equation of linear piezoelectric material 25
2.3.2 Model derivation 27

2.3.3 Generalised excitation force due to base excitation . . 34
2.4 Numerical simulation 35
2.5 Experiment validation of the piezoelectric beam model . . . 38
2.5.1 Experiment methodology 39
2.5.2 Results and discussion 40
2.6 Chapter conclusion 44

3 Dynamics of the rain harvester subjected to water droplet impact 46
3.1 Introduction 46
3.2 Modelling of the piezoelectric beam with water layer 50
3.3 Modelling of piezoelectric beam subjected to single droplet impact 53
3.4 Experiment validation of the single droplet impact model . . 59
3.4.1 Experiment methodology 60
3.4.2 Estimation of the impact coefficient 62
3.4.3 Results and discussion 68
3.5 Dynamics of the harvester subjected to multiple droplets impact 75
3.6 Experiment validation of the multiple droplet impact model 77
3.6.1 Experiment methodology 79
3.6.2 Results and discussion 80
3.7 Chapter conclusion 87

4 Performance of the energy harvester in a simulated rain environment 90
4.1 Introduction 90
4.2 Artificial rain excitation model 92
4.3 Experiment methodology 96
4.4 Numerical simulation 98
4.5 Results and discussion 103
4.5.1 Drop size distribution 104
4.5.2 Performance of the rain energy harvester 106
4.6 Chapter Conclusion 111

5 Performance of the energy harvester in actual rain 112
5.1 Introduction 112
5.2 Actual rain excitation model 113
5.2.1 Actual rain excitation model 114
5.2.2 Drop size distribution model 117
5.3 Performance of the harvester in actual rain 122
5.3.1 Experiment methodology 123

5.3.2 Experiment results 125
5.4 Verification of the theoretical model 129
5.5 Implication of results 133
5.6 Chapter conclusion 135

6 Optimisation of the raindrop impact energy harvester 136
6.1 Introduction 136
6.2 Related work 137
6.3 Proposed optimisation method 143
6.4 Design of the hybrid bridge rectifier 148
6.5 Performance of the hybrid rectifier in actual rain 154
6.5.1 Methodology 154
6.5.2 Results and discussion 156
6.5.3 Implication of result 161
6.6 Chapter conclusion 163

7 Conclusions and future work 164
7.1 Conclusions and summary of findings 164
7.2 Future work 169

Bibliography 171

A Device Specifications 186
A.1 Data logger (NI-USB6008) 186
A.2 Peristaltic pump (Cole Palmer-Masterex L/S series) 189
A.3 Laser vibrometer(MicroEpsilon-ILD1700-10) 190
A.4 Laser precipitation monitor sensor (Thies CLIMA-5.4110.10.000) 192

B MATLAB code 194

C Actual rain voltage graphs 211

List of Figures

1.1 Voltage produced by a piezoelectric element due to compression and tension via direct piezoelectric effect. 6

2.1 Piezoelectric cube [57]. 26
2.2 Schematics of Mide-v25w layers. 27
2.3 Schematics of the experiment setup. 40
2.4 Experiment setup: (1) laptop; (2) data logger; (3) voltage regulator and signal interfacing circuit; (4) accelerometer; (5) piezoelectric beam; (6) electromagnetic shaker; (7) function generator; (8) power amplifier. 40
2.5 Enlarged view of (a) data logger: NI-USB6008; (b) 3.3 V voltage regulator and signal interfacing circuit; (c) accelerometer: MMA7361; (d) piezoelectric beam: v25w. 41
2.6 Frequency response graph (first mode) with base excitation of 0.5 g. 42
2.7 Voltage time response graphs with base excitation of: (a) 0.25 g; (b) 0.375 g; (c) 0.5 g; (d) 1 g. 43

3.1 Schematics diagram of the side view of the piezoelectric beam (a) moment before impact and (b) the after impact. . 57
3.2 The (a) schematics and (b) photograph of the experimental setup. 63
3.3 Damping ratio against droplet number. 64
3.4 Added mass coefficient against droplet number. 64
3.5 First mode natural frequency against droplet number. 65
3.6 (a) Impact coefficient and (b) magnitude of the average impact force against droplet number. 66
3.7 Impact coefficient against added mass coefficient. 68
3.8 Camera images of static water layer at different droplet numbers (n = 1, 48, 276, 361, and 576); the corresponding voltage time response graphs (y-axis: voltage, V; x-axis: time, s); and the corresponding frequency response graphs (y-axis: voltage, V; x-axis: frequency, Hz). 69

3.9 Comparison on the (a) experimental and (b) theoretical frequency response graphs with (n = 576) and without (n = 1) the presence of water layer. 71
3.10 The comparison of experimental and theoretical peak voltage with fitted damping. 73
3.11 The comparison of experimental and theoretical RMS voltage. 73
3.12 RMS voltage against added mass coefficient 74
3.13 Impact position on the piezoelectric beam, where $x1$ = 42 mm, $x2$ = 27 mm, $x3$ = 12 mm, which are measured from the clamp. 77
3.14 (a) Overview and (b) schematics diagram of the experimental setup for multiple droplet excitation. 79
3.15 Voltage time response (black) and added mass coefficient (red) graphs for: (a) LSR; (b) MSR; and (c) HT. 82
3.16 Experimental and theoretical voltage time response graphs of water droplet impinging on position: (a) $x1$; (b) $x2$; and (c) $x3$. 83
3.17 Voltage time response graphs (y-axis: voltage,V; x-axis: time, s) for experimental results: (a) LSR; (b) MSR; (c) HT and theoretical results: (d) LSR; (e) MSR; (f) HT. 87

4.1 Overview of rain simulator: (1) rain nozzles; (2) control box; (3) laptop; (4) data logger; (5) laser precipitation monitor sensor; (6) piezoelectric beam. 97
4.2 Boxplots consist of added mass coefficients for the four artificial rains (each group of added mass coefficient contains 300 samples). 99
4.3 Flow chart for computation of artificial rain model. 103
4.4 Experimental and theoretical (mean of 10 samples) drop size distributions (DSD) for: (a) rain 1; (b) rain 2; (c) rain 3; (d) rain 4. 105
4.5 The (a) experimental and (b) theoretical results for the four artificial rains, where the x-axis represents time (s); y-axis represents voltage produced by the piezoelectric energy harvester (V). 107
4.6 The experimental and theoretical voltage time response graphs for the first 1.5 s of: (a) rain 1, (b) rain 2, (c) rain 3, (d) rain 4; where the x-axis represents time (s); y-axis represents voltage produced by the piezoelectric energy harvester (V). . 108
4.7 Experimental (red dotted line) and theoretical (10 samples in grey lines) energy accumulation graphs for: (a) rain 1; (b) rain 2; (c) rain 3; (d) rain 4. 109

5.1 Flow chart of obtaining the average number of droplet($\overline{N}_d$), and two fitting parameters for the lognormal distribution model (σ and μ). 119
5.2 Rain DSD of different rain rate bins obtained from experiment 10 rain events. 120
5.3 Experiment data and fitted curve for: (a) fitting parameter, σ;(b) fitting parameter, μ; (c) average number of droplet, $\overline{N}_d$. 122
5.4 (a) Overview and (b) schematics of the actual rain experiment setup. 124
5.5 Time series graphs of (a) rain rate; (b) voltage. The time series graphs were segmented into four sections: S1($t \leq 360s$; S2($360s \leq t < 1080s$); S3($1080s \leq t < 2460s$); and S4($t \geq 2460s$). 125
5.6 Water layer formed on the piezoelectric beam. 127
5.7 Time series graph of added mass coefficient. 128
5.8 The theoretical and experimental DSD comparison graphs for different rain rate bins (y-axis: raindrop density ($m^{-3}mm^{-1}$; x-axis: raindrop diameter (mm). 130
5.9 The experimental, theoretical, and modified theoretical voltage time response graphs, where the y-axes represent Voltage (V). 132
5.10 The experimental (in red dotted line), theoretical (10 samples in grey lines), and modified theoretical (10 samples in grey lines) energy accumulation comparison graphs, where the y-axis is the energy accumulation (μJ). 133

6.1 Block diagram of a standard harvester circuit topology. . . . 144
6.2 Schematic diagram of: (a) half bridge rectifier; (b) full bridge rectifier. 146
6.3 Input voltage from the piezoelectric harvester (V_p) and output voltage of the (a) half bridge rectifier, and (b) full bridge rectifier, measured across the load resistor (V_{RL}). 147
6.4 Control diagram of the hybrid bridge rectifier. 148
6.5 Schematics diagram of the manual switching circuit. 149
6.6 (a) Overview and (b) schematics diagram of the experimental setup. 151
6.7 Scatter plots of RMS voltages for SHB and SFB. 153
6.8 Zoom-in view of the RMS voltages for SHB and SFB. 153
6.9 Schematics diagram of the hybrid bridge rectifier circuit. . . 154
6.10 Flowchart of the control circuit for the hybrid bridge rectifier circuit. 155
6.11 (a) Overview and (b) schematics of the actual rain experiment setup 156

6.12 Rain rate graph with duration of 700 s. 157
6.13 The voltage time response graphs for the: (a) full bridge rectifier (PZT-A); (b) hybrid bridge rectifier (PZT-B). . . . 158
6.14 Zoom-in view on the voltage time response when the hybrid bridge rectifier is operating in: (a) half bridge mode; (b) full bridge mode. 159
6.15 Energy accumulation graphs for the full bridge rectifier (PZT-A) and hybrid bridge rectifier (PZT-B). The graph is partitioned into S1 ($t < 440s$) and S2 ($440 \leq t \leq 700s$). 159
6.16 Energy accumulation graphs of the full bridge (PZT-A) and-hybrid bridge (PZT-B) rectifiers of: (a)S1 ($t < 440$ s); (b) S2(440 s $\leq t \leq 700$ s). 160

C.1 Voltage time response graphs recorded from 10 actual rains . 212

List of Tables

1.1 A list of rain impact energy harvesters, where, D_w, v_w, m_w, and H, are the diameter, impact velocity, mass, and drop height of the impinging water droplet respectively. 11

2.1 Eigenvalue of the first four modes. 22
2.2 Material properties of the piezoelectric beam Mide-v25w. . . 28
2.3 Common parameters (first mode) used in the simulation of the theoretical results. 38
2.4 The experimental and theoretical peak voltages of different G-force with its respective percentage difference. 44

3.1 Raindrop density and drop period for different rain type. . . 76
3.2 Experimental and theoretical results, and the percentage error for the peak voltage when water droplet impacts at position $x1$, $x2$ and $x3$ of the piezoelectric beam. 85
3.3 Experimental and theoretical results, and the percentage error for the RMS voltage when water droplet impacts at position $x1$, $x2$ and $x3$ of the piezoelectric beam. 85

4.1 List of different rain types produced by the rain simulator. . 98
4.2 Rain no., nozzle used, rain rate, lognormal parameters (μ and σ), total number of droplets, and drop period of the four artificial rains. 102
4.3 Experimental and theoretical power produced by the piezoelectric energy harvester from the four simulated artificial rains. 110

5.1 The rain rate range for respective rain rate bin. 120
5.2 Rain drop diameter class. 124

6.1 The root mean square voltage (average of 10 samples) of respective configurations when excited by single droplet impact of various average impact forces. 152

Nomenclature

A	Impact velocity constant
$\overline{\overline{A}}$	State matrix
a	Device area
$a_b(t)$	Base acceleration function
a_r	Scaling factor
$\overline{\overline{B}}$	Input matrix
C_a	Added mass coefficient
C_i	Impact coefficient
C_n	Normalisation constant
C_p	Capacitance matrix
$\overline{\overline{C}}$	Output matrix
c_f	Friction coefficient of the water droplet
D_n	The nth random water droplet diameter
D_w	Diameter of water droplet
d_{31}	Strain coefficient
$\underline{\underline{D}}$	Modal damping matrix

$\overline{D}$	Electrical displacement components
$\overline{\overline{D}}$	Feedforward matrix
$E(t)$	Total energy accumulated over time, t
$\overline{E}$	Electrical field components
e	Piezoelectric constant
e_{31}^{T}	Coupling coefficient
$F(t)$	Generalised excitation force
$F_a(t)$	Generalised excitation force due to artificial rain
$F_b(t)$	Generalised excitation force due to base excitation
$F_m(t)$	Generalised excitation force due to multiple droplet impact
$F_r(t)$	Generalised excitation force due to actual rain
$F_{s,n}(t)$	Generalised excitation force due to n^{th} water droplet impact
f_{avg}	Average impact force
f_k	Local inertia load on the kth element
f_n	Impact force exerted by the piezoelectric beam due to the nth water droplet
G	Applied G-force due to base excitation
g	Gravity constant
H	Water droplet drop height
h	Thickness

I	Cross-sectional area moment of inertia
I_D	Current that passes through a diode
I_o	Reverse saturation current of a diode
(KE)	Kinetic energy
Km	Impact parameter
$\underline{K}$	Modal stiffness matrix
L	Length of the cantilever beam
$\underline{M}$	Modal mass matrix
m	Mass per unit length
m_w	Water droplet mass
N_d	Total number of water droplets
N_f	Total number of discretised elements
N_r	Total number of raindrop that impacts on the piezoelectric beam during actual rain
N_T	Raindrop density
N_t	Total number of water droplet measured by the laser precipitation monitor sensor
$\overline{N}_d$	Average number of droplet n^{th} water droplet count
P	Instantaneous peak power
(PE)	Potential energy
p	Momentum of the water droplet
$\overline{p}$	Amplitude of the eight-term sum of sine model

Q_r	Virtual work of the mechanical force
Q_v	virtual work of the electric charge
$q(t)$	Electric charge output function
$\overline{q}$	Frequency of the eight-term sum of sine model
R_w	Water droplet radius
R	Load resistance
R_2	Coefficient of determination
Re	Reynolds Number
$\overline{r}$	Phase constant for the eight-term sum of sine model
r_n	Generalised coordinate of the nth vibration mode
$\overline{S}$	Strain components
T	Sampling rate
T_d	Drop period
T_n	Drop period of the n_{th} drop
t_T	Total duration of the experiment
$\underline{T}$	Time period of the voltage response
$\overline{T}$	Stress components
$\overline{u}$	Input vector
V	Voltage
V_D	Forward voltage drop of a diode
V_{RL}	Voltage measured across a load resistor, RL
V_T	Thermal voltage

V_p	Voltage generated by the piezoelectric beam
V_{rms}	Root mean square voltage
v	Volume
v_w	Impact velocity of an impinging water droplet
$w(x,t)$	Transverse displacement of the neutral axis of point x at time t
We	Weber Number
W_{ie}	Internal electrical energy
x_n	Drop position of the nth drop
$\overline{x}$	State vector
Y	Young's modulus
YI	Bending stiffness
$\overline{y}$	Output vector
$(.)_0$	Represents the portion of water droplet that sticks on the beam after impact
$(.)^{"}$	The second derivation of the corresponding parameter with respect to the longitudinal direction, x
$(.)^E$	The corresponding parameter is evaluated at constant electric field
$(.)^S$	The corresponding parameter is evaluated at constant strain

$(.)_a$	Indicates that the corresponding parameter matrix is inclusive of the water layer
$(.)_{np}$	The corresponding parameter is non-piezoelectric material
$(.)_p$	The corresponding parameter is piezoelectric material
$(.)_s$	Represents the portion of water droplet that spread of splashed after impact
$(.)^t$	The corresponding matrix is transposed
$(.)_w$	Represents the corresponding parameter is of the water layer
$\dot{(.)}$	First derivative of the corresponding parameter with respect to time, t
$\ddot{(.)}$	Second derivative of the corresponding parameter with respect to time, t
α	Constant, $\int_0^L \phi_i(x)\phi_j(x)dx$
β	Eigenvalue for the mode shape
Δx	Length of discretised elements
$\delta(.)$	Variation of the corresponding variable
δ_{ij}	Kronecker delta
$\underline{\delta}$	Logarithmic decrement
η	Ideality factor
$\eta_s(t)$	Pulse function for single droplet impact

$\eta_m(t)$	Pulse function for multiple droplet impact
$\eta_a(t)$	Pulse function for artificial rain
$\eta_r(t)$	Pulse function for actual rain
ε	Permittivity constant
ε_{33}^S	Dielectric constant
ε_0	Electric constant
$\varepsilon_{r\,33}^S$	Relative permittivity
μ_w	Dynamic viscosity
ω	Natural frequency of the piezoelectric beam
ω_b	Angular frequency of the sine wave
ω_d	Damped natural frequency of the piezoelectric beam
Φ	Heaviside function
ϕ_n	Mode shape of the nth vibration mode
φ_n	Normalised mode shape of the nth vibration mode
$\psi(z)$	Electric field across the thickness of the beam
ρ	Density
ρ_{air}	Air density
ρ_w	Water density
σ_n	Constant, $[sin(\beta L) - sinh(\beta L)]/[cos(\beta L) + cosh(\beta L)]$
σ_w	Ratio of inertial force to surface tension
θ	Modal coupling matrix
τ	Impact duration

ξ	Damping ratio
$\mathscr{L}(\mu, \sigma)$	Lognormal distributed random number generating function with the parameters μ and σ
$\mathscr{U}(0, L)$	Uniform distributed random number generating function that ranges from 0 to L

Abbreviations

AC	Alternative current
DC	Direct current
DSD	Drop size distribution
FEA	Finite elements analysis
FFT	Fast Fourier Transform
HT	Heavy thundershower
IEEE	Institute of Electrical and Electronics
LED	Light emitting diode
LSR	Light stratiform rain
MEMS	Microelectromechanical systems
MSR	Moderate stratiform rain
PFB	Parallel full bridge configuration
PHB	Parallel half bridge configuration
PVDF	Polyvinylidene fluoride
PZT	Lead zirconate titanate
RMS	Root mean square

SDOF	Single degree-of-freedom
SFB	Series full bridge configuration
SHB	Series half bridge configuration
SSHI	Synchronised switching harvesting on an inductor
SSDCI	Synchronised switching and discharging to a storage capacitor through an inductor
USB	Universal serial bus

Chapter 1

Introduction

1.1 Background

The advancement of microelectronics has resulted our daily devices becoming smaller and consume less power without compromising their functionality. Presently, devices have shrunk small enough to fit into our pocket, enabling everyone to stay connected any time at anywhere. Some examples include wireless sensors, biomedical implants, remote weather station, and military monitoring devices [1, 2].

Based on the present microelectronics technology, most of the microdevices are powered by batteries. Unfortunately, batteries are bulky and need to be recharged or replaced frequently [3]. This becomes a huge challenge especially when such systems are installed in a remote area, where

battery replacement is cost ineffective, difficult, and not accessible. Fortunately, as the power utilisation of microelectronics device grows smaller, it can be powered by an energy harvester. An energy harvester is a device that can scavenge ambient energies such as mechanical vibration, thermoelectric, acoustic, and solar energy into usable electrical energy [3]. As a result, energy harvester is found to be slowly integrating into our daily devices [4].

Piezoelectric material is a smart material that converts vibration into electrical energy. Energy harvesting using piezoelectric is possible due to its distinctive property, which is the direct piezoelectric effect. The piezoelectric effect was first discovered by Jacques Curie and Pierre Curie in 1880 [5]. Through direct piezoelectric effect, piezoelectric material is able to convert strain or vibrational energy to electrical energy. Due to this unique property, piezoelectric material has found its way into a myriad of applications. An overview on piezoelectric energy harvesting is presented in Section 1.2.

Presently, harvesting rain impact energy is being explored as another viable source of ambient energy harvesting using piezoelectric material. Rain impact energy harvesting operates by converting strain induced by the impinging raindrops on the piezoelectric beam surface into usable electrical energy. A detailed literature review on rain impact energy harvester is presented in Section 1.3. It is found in literature that most of the theoretical

and experimental work are conducted in controlled laboratory environment and only includes single water droplet excitation. This sparks the interest of this research, which is to explore the possibility of rain impact energy harvester under actual raining condition.

1.2 Overview of piezoelectric energy harvesting

There are three general types of mechanical-to-electric converters for vibration energy harvesting application, which are electrostatic [6], electromagnetic [7], and piezoelectric [8]. The comparison of these three converters can be found in the study conducted by Boisseau et al. [9]. Comparing to electrostatic and electromagnetic energy harvesters, piezoelectric energy harvester has less design constrains as it is easier to be integrated in to microelectromechanical systems (MEMS) [9]. Besides this, piezoelectric energy harvester is self-sustainable, unlike electrostatic energy harvester that requires the distance between the plates to be controlled and the electrets to be pre-charged. Due to the higher power density of a piezoelectric energy harvester when compared to electrostatic and electromagnetic energy harvesters [3, 10], piezoelectric energy harvester is often a preferred candidate for vibration energy harvesting.

In year 1880, the Curie brothers discovered piezoelectricity after noticing certain crystals such as Rochelle salt, topaz, and quartz, exhibited surface charge when strain is being induced [5]. This phenomenon is known as the direct piezoelectric effect. The direct piezoelectric effect is utilised in a piezoelectric energy harvester. Mechanical strain is generated when electrical field is applied across a piezoelectric material. Such effect is known as the converse piezoelectric effect, which is discovered by Lippman [11]. Hence, piezoelectric material can also be implemented as an actuator.

There are a wide variety of piezoelectric materials ranging from crystal, polymer, and ceramic. Examples for crystal are Langasite [12] and Quartz [13]; example for polymer is Polyvinylidene Fluoride (PVDF); example for ceramic is Lead Zirconate Titanate (PZT). The ability of a piezoelectric material to convert mechanical energy to electrical energy or vice versa is measured by coupling factor [14]. In comparison, crystal has lower coupling factor than polymer and ceramic. As a result, majority of the recent energy harvesting devices are designed using polymer or ceramic [8]. Comparing piezoelectric ceramic to piezoelectric polymer, piezoelectric ceramic offers higher coupling factor, which will produce higher energy, while piezoelectric polymer offers higher mechanical flexibility and lower stiffness, which will increase device lifetime by lowering chances of fatigue [14, 15].

For a material to possess piezoelectric properties, it has to be poled. Poling is a procedure of applying strong electric field across a material so

that it could exhibit piezoelectric properties [16]. During this process, the strong electric field aligns the dipoles in the material so that they are in the direction of the electric field. Most of the dipoles are locked in the same orientation when the electric field is removed, and the material is now permanently poled. Once a poled piezoelectric material experiences mechanical tension or compression, the positive and negative electrical charges within the structure will be separated. The movement of the positive and negative electrical charges is measured by dipole moment. The variation in dipole moment within the structure will allow the poled piezoelectric material to produce electrical charge [17].

A schematics diagram on the generation of voltage due to compression or tension on a piezoelectric material is illustrated in Figure 1.1. When a piezoelectric material is compressed along the direction of polarisation, voltage of the same polarity as the poling voltage will be produced. On the other hand, when tension is introduced along the direction of polarisation, voltage with opposite polarity as the poling voltage will be generated [16]. By exploiting the direct piezoelectric effect, a poled piezoelectric material can be utilised as an energy harvester to scavenge electrical energy from ambient vibration energy sources.

Piezoelectric energy harvesting has become a growing trend in the past few decades and has been introduced to a variety of industries and sectors

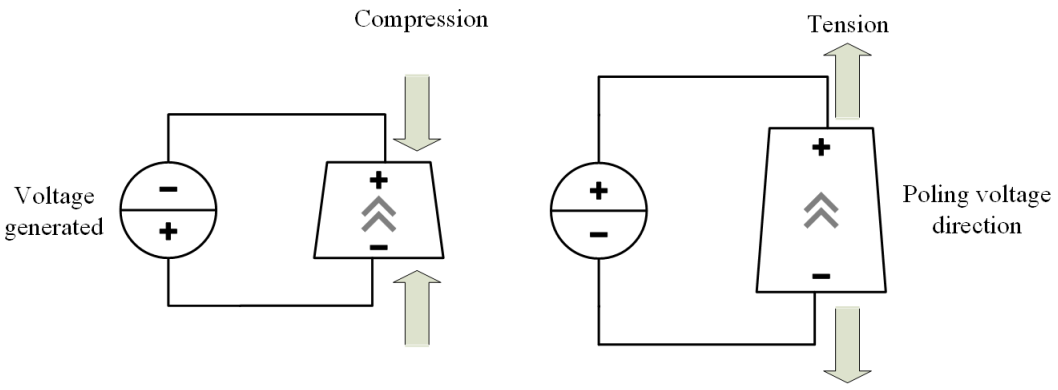


Figure 1.1: Voltage produced by a piezoelectric element due to compression and tension via direct piezoelectric effect.

[8]. This includes application of piezoelectric material in land vehicles [18–20], unmanned aerial vehicle [21], building [22], wearable devices [23–25], wind energy harvesting [26, 27], and ocean wave energy [28, 29].

1.3 Motivation

Tropical climate countries such as Malaysia, Indonesia, and Brazil benefit from abundant annual rainfall. Water vapour condenses in the atmosphere, forming raindrops. The height at which the raindrops formed provided substantial amount of potential energy. As the raindrops fall, the potential energy will be converted to kinetic energy gradually as the velocity increases. Due to air resistance and drag force, raindrops of different diameters can only reach certain maximum velocity, which is known as terminal velocity. This also limits the kinetic energy of the falling raindrops. By capturing

the kinetic energy of a falling raindrop before hitting the ground using a piezoelectric material, electrical energy can be harvested.

Raindrop impact energy harvesting is a feasible and sustainable form of alternative energy source for a tropical climate country. Many applications can be realised by such technology. Application such as powering up a light emitting diode (LED) for road sign, street light, and rain sensor that do not requires external power source can be accomplished by scavenging raindrop energy.

Biswas and Mandal [30] have shown the potential of harvesting rainfall energy in Bangladesh. According to the authors, solar home system is introduced in areas, which are not reached by the electric grid. One disadvantage of using solar as alternative energy is that it is not efficient during the monsoon month, where sun light is scarce due to rain season. As a result, integrating raindrop impact energy harvesting in to such home system shows promising potential.

Two types of raindrop energy harvesting methods were proposed by Tinaikar [31], which are by utilising the potential head available at building tops and the kinetic energy of the falling raindrop directly. The first method make use of the potential head of a multi-story buildings to generate electricity by using turbines while the latter uses piezoelectric materials

to directly produce electricity. Raindrop energy harvesting is a good alternative energy for rainy outdoor environments especially when solar energy is difficult to gather at night. However, as discussed by Tinaikar [31], there are several drawbacks for raindrop energy harvesting. Presently, the electricity generated by a raindrop energy harvester is less cost efficient than fossil fuels at their current costs. Secondly, the power generated by piezoelectric material is very low and could not be utilised directly. In addition, such system is only functional during rainy conditions, which will increase the payback period.

On the bright side, raindrop energy harvester can be coupled with other energy harvesters such as wind and solar to improve the overall system performance. In addition, raindrop impact energy harvester array can be implemented as suggested by Ilyas and Swingler [32] to improve the energy output of the harvester system. Raindrop energy harvesting is not a new concept. A list of raindrop energy harvester researches is compiled in Table 1.1. The study of single water droplet impact on a piezoelectric energy harvester is well established. Theoretical [33] and experimental [34] studies were conducted by impinging a single droplet on a PVDF membrane. The artificial raindrops were generated accurately by using a syringe pump. From the experiment results, a 3 mm diameter water droplet with an impact velocity of 4.5 m/s was able to produce an instantaneous power of 8.0 μW.

Vatansever et al. [35] had experimented with water droplets with masses

of 50 mg and 7.5 mg from different heights impinging on a PVDF and PZT composite structures. It is concluded that water droplet with larger mass and released from greater heights is able to generate higher peak voltage. Experimental results revealed that with a drop height of 0.1 m, the maximum peak voltage generated by the PVDF and PZT cantilever structure were approximately 12 V and 3 V respectively.

The response of a single water droplet impacting on a PVDF beam had been studied by Viola et al. [36]. A pipette was used to simulate a falling raindrop. The water droplet's fall speed was achieved by adjusting the height between the tip of the pipette and the impact plane. A peak voltage of 6 V was recorded when a 0.12 g water droplet falling from 0.8 m impacted the PVDF beam.

Another experimental study based on single water droplet impact on a five layers PZT cantilever beam was conducted by Al Ahmad [37]. The artificial raindrop was produced by using a micropump. The system was able to generate an instantaneous power of 23 μW when a 0.23 g water droplet with an impact velocity of 3.43 m/s was introduced.

A recent numerical simulation study conducted by Perera et al. [38] investigated the performance of a PVDF membrane under three rain types, which are light stratiform rain (LSR), moderate stratiform rain (MSR), and heavy thunderstorm (HT). From the numerical simulation results, a

maximum power of 2.231x10^{-29} W can be harvested from a 1 m^2 area of a PVDF membrane during heavy thundershower.

An innovative raindrop energy harvester by using a combination of diaphragm and PVDF cantilevers was studied by Chin-Hong et al. [39]. Parameters such as piezoelectric thickness, displacement induced by vibration, and maximum applicable pressure are analysed. Optimal design parameters were successfully obtained by obtaining Finite Elements Analysis (FEA). However the voltage or power output generation was not provided in the study. A literature review study on raindrop energy harvesting was performed by Wong et al. [40]. An experiment study was also conducted to demonstrate the feasibility of raindrop energy harvesting. The single water droplet test demonstrated that when a water droplet with diameter of 5.7 mm falling from height of 1 m was able to generate output voltage of 1.0 V and 3.5 V for a PVDF cantilever structure and a PVDF bridge structure respectively.

The behaviour of a piezoelectric beam due to water droplet impact is investigated by Ilyas and Swingler [32]. Raindrop was artificially generated in laboratory by using a burette. The artificial raindrop has a fixed drop size with diameter of 2 mm and it was tested at various fall heights. From the experiments, the mean power output of the investigated energy harvester is reported to be 1.8 μW. In addition, a model based on empirical data has

also been developed to demonstrate the viability of a rain energy harvester array.

Theoretical and experimental study for single droplet impact on a piezoelectric energy harvester had been reported repeatedly in the literature [32–40]. Besides this, the tests were conducted in laboratory conditions where the impact position, drop size and drop height were fixed. Having low drop height, the falling droplet could not reach its terminal velocity due to height constrain in the experiment setup. As a result, the reviewed studies could not capture the essence of actual raining condition, where the raindrops are falling with terminal velocity, the impact position of each raindrop is arbitrary, and the raindrop size [41] are stochastic in nature. Therefore, more work have to be conducted in order to realise a functional raindrop impact energy harvester, and this has became the main drive for the research.

Table 1.1: A list of rain impact energy harvesters, where, D_w, v_w, m_w, and H, are the diameter, impact velocity, mass, and drop height of the impinging water droplet respectively.

Researcher	**Year**	**Vibration source**	**Harvester type**	**Voltage output**	**Power output**
Guigon et al. [34]	2008	D_w: 3.0 mm v_w: 4.5 m/s	PVDF band	Peak: 4.68 V	Instantaneous: 8.0 μW
Vatansever et al. [35]	2011	m_w: 50.0 mg H: 0.1 m	PVDF cantilever PZT cantilever	Peak: 12.0 V Peak: 3.0 V	-
Al Ahmad [37]	2014	m_w: 0.23 g	PZT cantilever	Peak-to-peak: 0.8 V	Instantaneous: 23.0 μW

		v_w: 3.43 m/s			
Perera et al. [38]	2014	Thunder shower	PVDF membrane	-	Maximum: $2.23x10^{-29}$ W
Viola et al. [36]	2014	m_w: 0.12 g H: 0.8 m	PVDF cantilever	Peak: 6.0 V	-
Wong et al. [40]	2015	D_w: 5.7 mm H: 1.0 m	PVDF cantilever PVDF bridge	Peak: 1.0 V Peak: 3.5 V	-
Ilyas and Swingler [32]	2015	D_w: 2.0 mm H: 0.47 m	PVDF cantilever	-	Mean: 1.8 μW

1.4 Aim and Objectives

This project aims to investigate the performance of a raindrop impact energy harvester via theoretical and experimental studies.

The objectives of this research include:

1. To propose a mathematical model for a piezoelectric beam describing the harvesting mechanism of a raindrop impact energy harvester.
2. To carry out experiments to validate the theoretical models.
3. To propose a optimisation method for the existing harvester circuit for the application of raindrop impact energy harvesting.

1.5 Summary of original contributions

The novelty of this work is to expand the knowledge and technology on the development of the raindrop impact energy harvester. Most of the studies conducted to date involve single water droplet impact. Moreover, loss in energy generation is reported [33] due to splashing effect of a water droplet impact. In addition, the effect of water droplet accumulation on the piezoelectric beam is not outlined in the literature. The contributions of this work are to fill the knowledge gap in this area. A summary of original contributions is given as below.

The dynamics of the piezoelectric beam may change when the water droplets impact on the beam and start to accumulate on its surface. In this study, an added mass coefficient was introduced. The added mass coefficient is modelled as a discrete function of droplet number count. The added mass coefficient can be associated to the ratio of the modal mass of the water layer formed to the modal mass of the piezoelectric beam structure without any water layer. Theoretical study on the added mass effect revealed that the water layer formed on the piezoelectric beam surface will affect the modal mass, modal damping and modal excitation force of the piezoelectric beam.

The loss of energy generation due to splashing effect can be explained by loss of momentum due to the post impact behaviour of a water droplet impact. Momentum will be lost during spreading, recoiling, or splashing behaviour of a water droplet upon impact. Moreover, the spreading and recoiling stages are affected by the surface wettability and roughness [42–44]. In contemplation of

taking into account of the post impact behaviour of water droplet impact, an impact coefficient is proposed. Similar to the added mass coefficient, the impact coefficient is modelled as a discrete function of droplet number count. Experimental and theoretical results showed that after taking the added mass coefficient and impact coefficient into account, the peak and RMS voltage response of the system exhibited curvilinear behaviour when plotted against the droplet number count. Hence, it was clearly demonstrated that the added mass effect and impact coefficient had to be taken into account when designing a raindrop impact energy harvester.

In actual rain, raindrops will be impinging on different positions on the piezoelectric beam at different drop periods. A multiple droplet impact model is hence developed to incorporate excitation of fixed droplet diameter at different position on the piezoelectric beam with different drop periods. It has been shown that when the water droplet impacts further from the clamp, higher RMS voltage will be generated. In addition, as the rate of droplet impact increases , more energy will be produced by the energy harvester.

To simulate the raining conditions in laboratory, a rain simulator was developed to generate four types of rainfalls with different rain rates. This is to investigate the performance of the rain impact energy harvester under artificial rain with fixed rain rates. In an attempt of modelling the artificial rain excitation model, two random parameters are introduced, namely the raindrop size and the impact position on the piezoelectric beam. The raindrop size is governed by the drop size distribution (DSD) of the artificial rains. On the other

hand, the impact position on the piezoelectric beam is assumed to be uniformly distributed. Experimental and theoretical results revealed that as the rain rate increases, higher power is generated from the raindrop impact energy harvester.

The performance of the raindrop impact energy harvester was tested in actual rain. The excitation model for actual rain is devised by considering the variation of rain rate, DSD, and raindrop count. According to the theoretical model, the piezoelectric energy harvester will generate higher absolute peak voltage during higher rain rate. However such trend was not found in the experimental result. The theoretical model for actual rain is modified explicitly to the experimental result to demonstrate its practicability. The maximum instantaneous power generated by the harvester in experiment was measured to be 3.75 mW, this is higher than the maximum instantaneous power recorded in the literatures, which was 23 μW.

The voltage generated by a piezoelectric beam has to be processed by a harvester circuit so that it could be stored into a battery. It was found that most of the harvesting circuits utilised in piezoelectric energy harvesting considered harmonic excitation sources. In the case of raindrop impact energy harvesting, source of excitation is stochastic and impulsive in nature. To address this issue, hybrid bridge rectifier circuit is proposed. The hybrid bridge rectifier circuit consists of full bridge and half bridge rectifiers, which are controlled by microcontroller switching.

1.6 Thesis overview

Chapter One introduces the background study of piezoelectric energy harvesting. Literature survey on piezoelectric raindrop impact energy harvesting is also presented in this chapter.

Chapter Two presents the mathematical model for a piezoelectric beam. The model is evaluated through a shaker test using various G-forces.

Chapter Three studies the dynamical model of a raindrop impact energy harvester. The models discussed in this chapter include the effect of water droplet accumulation on the surface of the piezoelectric beam by using added mass coefficient; the description of the post impact behaviour of water droplet impact by using impact coefficient; and the modelling of multiple droplet excitation with the considerations of drop position and drop period. The dynamical models were validated by using experimental results in this chapter.

Chapter Four further extends the multiple droplet excitation model to incorporate raindrops with random sizes impinging at different position on the piezoelectric beam. Numerical simulation of the artificial rain excitation model is highlighted in this chapter. The experimental and theoretical study considers four rain rates generated by a rain simulator.

Chapter Five investigates the performance of the raindrop impact energy harvester in actual rain. Variation of rain rate, DSD, number of raindrops were considered in the actual rain excitation model. The theoretical model is validated through experimental result in this chapter.

Chapter Six highlights the optimisation of the harvester through the implementation of a hybrid bridge rectifier. The hybrid bridge rectifier consists of a full bridge and half bridge rectifier, controlled by a microcontroller.

Chapter Seven concludes this thesis and recommendations for future works are provided.

Chapter 2

Mathematical modelling of the piezoelectric beam

2.1 Introduction

The mathematical model of a piezoelectric beam is presented in this chapter. In this study, a Lead Zirconate Titanate (PZT) piezoelectric composite beam is used as a raindrop impact energy harvester. Mathematical model is essential for understanding the behaviour of the system when being excited with different excitation forces. In addition, the performance of the system could be optimised by applying parameter variation of the dynamic model.

In the subsequent analysis, the piezoelectric beam is modelled as a distributed parameter system. In a distributed system, the mass and stiffness

properties are considered to be distributed throughout the beam structure as a series of infinitely small elements. These small elements will move relative to each other in a continuous manner [45].

The distributed parameter beam model is established by conducting modal analysis of a cantilever beam. The mode shape of a cantilever beam can then be derived. To obtain the actual dynamic response, the orthogonality characteristic of the eigenfunctions is discussed and the normalisation of the mode shape is illustrated in Section 2.2. Next, the dynamics of the piezoelectric energy harvester is investigated. The mathematical model is developed by applying the constitutive equation of linear piezoelectric material, Rayleigh-Ritz Theorem and Lagranges equations for electromechanical systems. Base excitation is applied to the piezoelectric beam and it is described by summing up the discretised elements of the piezoelectric beam.

The mathematical model is simulated using MATLAB. An experiment by applying base excitation to the piezoelectric beam that consists of four different G-forces were conducted to validate the mathematical model. The first mode natural frequency of the experimental and theoretical results are in good agreement. Furthermore, both experimental and theoretical peak voltages increase as the G-force increases. Generally, the theoretical results are in good consensus with the experimental results. The percentage difference of the experimental and theoretical results range from 9.30 % to 25.45 %.

2.2 Modal Analysis of a piezoelectric cantilever beam

The piezoelectric cantilever beam used in this study consists of two layers of PZT material and other composite materials. A cantilever beam is defined as a beam that is free at one end and clamped at the other. Through modal analysis, the dynamical properties such as natural frequency and mode shape of a structure under external excitation can be examined. In this section, the mode shape of a cantilever beam is derived. Next, the orthogonality of the related eigenfunctions will be explored. The mode shape normalisation method is presented at the end of this section.

2.2.1 Derivation of cantilever beam mode shape

The governing equation of motion of a cantilever beam due to free vibration [46] can be expressed as:

$$YI\frac{\partial^4 w(x,t)}{\partial x^4} + m\frac{\partial^2 w(x,t)}{\partial t^2} = 0 \tag{2.1}$$

where,YI is the bending stiffness (Y is the Youngs modulus and I is the cross-sectional area moment of inertia); $w(x,t)$ is the transverse displacement relative to the neutral axis of point x at time t; m is the mass per unit length of the cantilever beam.

The boundary condition of the cantilever beam at the clamped end can be written as:

$$w(0,t)=0; \qquad \left.\frac{\partial w(x,t)}{\partial x}\right|_{x=0}=0; \qquad \left.\frac{\partial^2 w(x,t)}{\partial x^2}\right|_{x=L}=0; \qquad \left.\frac{\partial^3 w(x,t)}{\partial x^3}\right|_{x=L}=0 \tag{2.2}$$

where, L is the length of the cantilever beam.

As suggested by Rayleigh-Ritz method [47], the displacement of a beam can be expressed as a summation of vibration modes of the beam with generalised coordinates as:

$$w(x,t)=\sum_{\underline{n}=1}^{\infty}\varphi_{\underline{n}}(x)r_{\underline{n}}(t) \tag{2.3}$$

where, $\varphi_{\underline{n}}$ is the normalised mode shape of the $\underline{n}^{th}$ vibration mode; $r_{\underline{n}}$ is the generalised coordinate for the $\underline{n}^{th}$ vibration mode.

By using Equation (2.1-2.3), the mass normalised mode shape of a cantilever beam is derived as:

$$\varphi_{\underline{n}}(x)=C_n\phi_{\underline{n}}(x) \tag{2.4}$$

$$\phi_{\underline{n}}(x)=[cos(\beta_{\underline{n}}x)-cosh(\beta_{\underline{n}}x)]+\sigma_{\underline{n}}[sin(\beta_{\underline{n}}x)-sinh(\beta_{\underline{n}}x)]\} \tag{2.5}$$

where, C_n is the normalisation constant; $\phi_{\underline{n}}(x)$ is the mode shape of the $\underline{n}^{th}$ vibration mode; $\sigma_{\underline{n}}$ is written as: $\sigma_{\underline{n}}=[sin(\beta L)-sinh(\beta L)]/[cos(\beta L)+cosh(\beta L)]$; β is the dimensionless frequency numbers, or known as eigenvalue [45], which can be obtained from the characteristic equation as:

$cos(\beta L)cosh(\beta L)=-1$. The first four eigenvalues are presented in Table 2.1.

Table 2.1: Eigenvalue of the first four modes.

Mode	**Eigenvalue(β)**
1	1.87510407
2	4.69409113
3	7.85475744
4	10.9955407

2.2.2 Normalisation of mode shape

In order to obtain the response of a cantilever beam structure, the mode shape has to be normalised. This is because the mode shape itself only represents the structure of motion for the system and it is dimensionless [48].

The normalisation of the mode shape has to satisfy the orthogonality condition of the mode shape [49]:

$$\int_0^L \varphi_i(x) m \varphi_j(x) dx = \delta_{ij} \tag{2.6}$$

where, m is the mass per unit length of the cantilever beam, δ_{ij} is the Kronecker delta, which is defined as:

$$\delta_{ij} = \begin{cases} 1, & \text{when } i = j. \\ 0, & \text{when } i \neq j. \end{cases} \tag{2.7}$$

The normalised mode shape of a cantilever beam in Equation (2.4) is recalled as:

$$\varphi_{\underline{n}}(x) = C_n\{[cos(\beta_{\underline{n}}x) - cosh(\beta_{\underline{n}}x)] + \sigma_{\underline{n}}[sin(\beta_{\underline{n}}x) - sinh(\beta_{\underline{n}}x)]\} \tag{2.8}$$

The normalisation constant, C_n, can be solved by using the orthogonality condition of the mode shape, shown in Equation (2.6). The normalisation constant is solved as:

when $i = j$,

$$\int_0^L \varphi_i(x) m \varphi_j(x) dx = 1$$

by substituting Equation (2.4),

$$C_n^2 \int_0^L \phi_i(x) m \phi_j(x) dx = 1$$

$$C_n = \sqrt{\frac{1}{m\alpha}} \tag{2.9}$$

where, $\alpha = \int_0^L \phi_i(x)\phi_j(x)dx$

2.3 Modelling of the piezoelectric beam

The modelling of a piezoelectric beam had been studied in a substantial number of researches. The electromechanical behaviour of a piezoelectric beam can be modelled as a Single degree-of-freedom (SDOF) system by using lumped-parameter method [3, 50]. The model of a lumped parameter piezoelectric beam

consists of mechanical domain and electrical domain. The mechanical domain of a lumped parameter piezoelectric beam is described by a mass-spring-damper system. The electrical domain is made up of internal capacitance of the piezoelectric layers and the external load resistance [51]. Lumped parameter modelling provides a simple solution as the mechanical domain can be coupled into the electrical domain by using a transformer relation formulated by using the electric constitutive equation [45]. As a result, some important characteristics of the coupled dynamical system, such as the strain distribution along the beam, dynamics mode shape, and the effects of the mechanical domain on the electrical responses will be missed out [51].

In order to predict the electromechanical behaviour of a piezoelectric beam more accurately, a distributed parameter model is needed. Distributed parameter modelling discretises the system by applying the Rayleigh-Ritz discretisation method [46]. The Rayleigh-Ritz discretisation method provides a spatially discretised model for the distributed parameter system. A distributed parameter model describing piezoelectric actuation is developed by Hagood et al. [52] by applying the Rayleigh-Ritz discretisation method and Hamiltons principle for electromechanical system [53].

The piezoelectric beam modelled using distributed parameter system is more accurate than a lumped parameter system. This is because the distributed parameter system approximates the system as a discretised system by reducing the infinite mechanical degree-of-freedom to a finite dimension. For example,

models in [3, 54, 55] are developed by using Rayleigh-Ritz and Hamiltons principal based on the Euler-Bernoulli beam theory.

In this study, the piezoelectric beam model developed by Sodano et al. [54] is adopted. The model is developed based on the Rayleigh-Ritz discretisation method [52] and the extended Hamiltons Principle for electromechanical systems [53]. This section first presents the constitutive equation of linear piezoelectric material. This is followed by the derivation of the mathematical model of the piezoelectric beam using the Electromechanical Lagrange Equation, which is based on the extended Hamiltons Principle.

2.3.1 Constitutive equation of linear piezoelectric material

The linear constitutive equations of a piezoelectric material are derived based on the Institute of Electrical and Electronics (IEEE) Standard on Piezoelectricity [17]. Poled piezoelectric ceramics are usually transversely isotropic materials. Thus, their physical properties are symmetrical about the z-axis (indicated by the number 3 in Figure 2.1, which is normal to the xy-plane (also indicated as 12-plane in Figure 2.1. The z-axis here is also known as the poling axis of the material. The direction of the axes and planes is shown in represented by a piezoelectric cube in Figure 2.1.

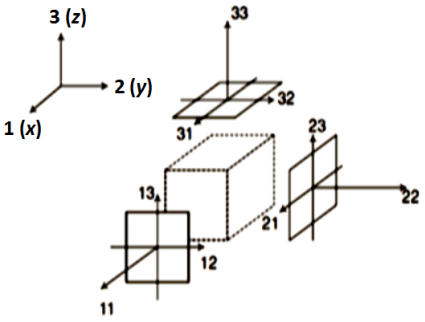


Figure 2.1: Piezoelectric cube [57].

The constitutive equations are defined by the following four field variables: stress components ($\overline{T}$), strain components ($\overline{S}$), electrical field components ($\overline{E}$), and electrical displacement components ($\overline{D}$). The piezoelectric constitutive equations are stablished by using either two of the four field variables as independent variables. In the case of a piezoelectric beam, 31-mode is considered. In 31-mode, stress is applied along the 1-axis direction, and the induced electric field is in the 3-axis direction [3]. The piezoelectric constitutive equations in the stress-electric displacement form for 31-mode is defined as [45]:

$$\begin{bmatrix} \overline{T}_1 \\ \overline{D}_3 \end{bmatrix} = \begin{bmatrix} Y_{11}^E & -e_{31} \\ e_{31} & \varepsilon_{33}^s \end{bmatrix} \begin{bmatrix} \overline{S}_1 \\ \overline{E}_3 \end{bmatrix} \tag{2.10}$$

where, e is the piezoelectric constant; Y is the Young's modulus; ε is the permittivity constant; $(.)^s$ indicates that the corresponding parameter is evaluated at constant strain; $(.)^E$ indicates that the corresponding parameter is evaluated at constant electric field.

2.3.2 Model derivation

In this study, an off-the-shelf piezoelectric beam (Mide-v25w) is used. The piezoelectric beam is made out of 11 layers of non-piezoelectric material and two layers of piezoelectric material (PZT). In the centre of the piezoelectric beam lies the ESPANEX layer, which is composed of a polyimide layer sandwiched by two copper layers. Figure 2.2 illustrates the piezoelectric beam composite layers. Throughout the study, x-axis, y-axis, and z-axis represent the length, width and thickness direction of the piezoelectric beam. The material properties are given in Table 2.2.

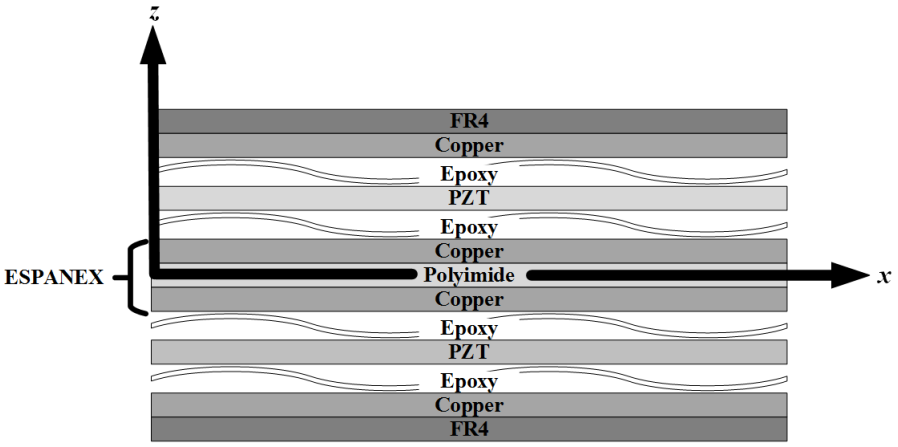


Figure 2.2: Schematics of Mide-v25w layers.

The model of a piezoelectric energy harvester is formulated from the electromechanical Lagrange equations based on the extended Hamiltons principle are given as [45]:

Table 2.2: Material properties of the piezoelectric beam Mide-v25w.

FR4		**PZT**	
Density (kg m^{-3})	1850	Density (kg m^{-3})	7800
Tensile modulus (GPa)	23.4	Tensile modulus (GPa)	67
Length (mm)	46.355	Length (mm)	45.974
Width (mm)	38.1	Width (mm)	33.274
Thickness (mm)	0.0762	Thickness (mm)	0.127
Copper		Relative permittivity	830
Density (kg m^{-3})	8960	Strain constant (pC N^{-3})	-190
Tensile modulus (GPa)	117	**ESPANEX**	
Length (mm)	46.355	Density of polyimide (kg m^{-3})	1430
Width (mm)	38.1	Density of copper (kg m^{-3})	8960
Thickness (mm)	0.0254	Tensile modulus of ESPANEX (GPa)	4.5
Epoxy		Length (mm)	46.355
Density (kg m^{-3})	1250	Width (mm)	38.1
Tensile modulus (GPa)	3.5	Thickness of ESPANEX (mm)	0.0762
Length (mm)	46.355	Thickness of polyimide (mm)	0.0254
Width (mm)	38.1	Thickness of copper (mm)	0.0254
Thickness (mm)	0.007		

$$\text{Mechanical Lagrange Equation: } \frac{d}{dt}\left[\frac{\partial(KE)}{\partial \dot{r}}\right] - \frac{\partial(KE)}{\partial r} + \frac{\partial(PE)}{\partial r} - \frac{\partial W_{ie}}{\partial r} = Q_r \tag{2.11}$$

$$\text{Electrical Lagrange Equation: } \frac{d}{dt}\left[\frac{\partial(KE)}{\partial \dot{V}}\right] - \frac{\partial(KE)}{\partial V} + \frac{\partial(PE)}{\partial V} - \frac{\partial W_{ie}}{\partial V} = Q_V \tag{2.12}$$

where, (KE) is the kinetic energy; (PE) is the potential energy; W_{ie} is the internal electrical energy; Q_r is the virtual work of the mechanical force; Q_V is the

virtual work of the electric charge; $(\dot{.})$ is the first derivative of the corresponding parameter with respect to time, t; V is voltage; r is the generalised coordinate.

The kinetic energy of the system is expressed as:

$$(KE) = \frac{1}{2}\int_{v_{np}} \rho_{np}\dot{w}^t(x,t)\dot{w}(x,t)dv_{np} + \frac{1}{2}\int_{v_p} \rho_p\dot{w}^t(x,t)\dot{w}(x,t)dv_p \tag{2.13}$$

where, v is volume; ρ is density; $(.)_{np}$ indicates that the corresponding parameter belongs to a non-piezoelectric material; $(.)_p$ indicates piezoelectric material; $(.)^t$ indicates that the corresponding matrix is transposed.

By applying the Rayleigh-Ritz method in Equation (2.3) into Equation (2.13), the kinetic energy of the system can be rearranged as:

$$(KE) = \frac{1}{2}\dot{r}^t(t)\dot{r}(t)[\underline{M}_{np} + \underline{M}_p] \tag{2.14}$$

The modal mass matrix ($\underline{M}$) of the piezoelectric beam, v25w, can be written as:

$$\begin{aligned}\underline{M} &= \int_{v_{np}} \rho_{np}\varphi^t(x)\varphi(x)dv_{np} + \int_{v_p} \rho_p\varphi^t(x)\varphi(x)dv_p \\ &= \int_{v_{esp}} \rho_{esp}\varphi^t(x)\varphi(x)dv_{esp} + 2\int_{v_c} \rho_c\varphi^t(x)\varphi(x)dv_c + \\ &\quad 2\int_{v_{fr4}} \rho_{fr4}\varphi^t(x)\varphi(x)dv_{fr4} + 4\int_{v_{ep}} \rho_{ep}\varphi^t(x)\varphi(x)dv_{ep} + \\ &\quad 2\int_{v_P} \rho_p\varphi^t(x)\varphi(x)dv_p\end{aligned} \tag{2.15}$$

where, the subscripts: esp, c, $fr4$, ep, and p indicate the corresponding parameter belongs to ESPANEX, copper, FR4, epoxy, and PZT layer respectively.

The potential energy of the system is written as:

$$(PE) = \frac{1}{2}\int_{v_{np}} \overline{S}_{np}^{t}\overline{T}_{np}dv_{np} + \frac{1}{2}\int_{v_p} \overline{S}_{p}^{t}\overline{T}_{p}dv_{p} \tag{2.16}$$

For a non-piezoelectric material, the stress parameter is defined by using Hookes Law as:

$$\overline{T}_{np} = Y\overline{S}_{np} \tag{2.17}$$

A few assumptions have to be established before the potential energy for the system can be fully defined. These assumptions are the Euler-Bernoulli Beam Theory, the constitutive equation for piezoelectric material, and the electric potential across the piezoelectric material.

The Euler-Bernoulli Beam Theory assumes that strain is the product of distance from the neutral axis (z), and the second derivative of displacement with respect to the position along the beam (x). The equation for strain is written as:

$$\overline{S} = -z\frac{\partial^2 w(x,t)}{\partial x^2} \tag{2.18}$$

By applying Rayleigh-Ritz method in Equation (2.3) to Equation (2.18), the following expression for strain can be obtained:

$$\overline{S} = -z\varphi(x)^{"}r(t) \tag{2.19}$$

where, $(.)^{"}$ indicates that the second derivation of the corresponding parameter with respect to the longitudinal direction, x.

The piezoelectric beam is an inactive material and during energy harvesting, no external electric field is applied to the beam. Therefore, the electric potential across the piezoelectric material can be assumed constant. The electric field across the composite piezoelectric beam is realised as:

$$E_3 = \psi(z)V = \begin{cases} 0, & \frac{h_{esp}}{2} + h_{ep} + h_p < z < \frac{h_{esp}}{2} + 2h_{ep} + h_p + h_c + h_{fr4} \\ -\frac{V}{h_p}, & \frac{h_{esp}}{2} + h_{ep} < z < \frac{h_{esp}}{2} + h_{ep} + h_p \\ 0, & -\frac{h_{esp}}{2} - h_{ep} < z < \frac{h_{esp}}{2} + h_{ep} \\ \frac{V}{h_p}, & -\frac{h_{esp}}{2} - h_{ep} < z < -\frac{h_{esp}}{2} - h_{ep} - h_p \\ 0, & -\frac{h_{esp}}{2} - h_{ep} - h_p < z - \frac{h_{esp}}{2} - 2h_{ep} - h_p - h_c - h_{fr4} \end{cases} \tag{2.20}$$

where, h is the thickness of the respective layer; ψ defines the electric field across the thickness of the beam.

By substituting Equation (2.10, 2.19, and 2.20) into Equation (2.16), the potential energy of the system can be rewritten as:

$$(PE) = \frac{1}{2} r^t(t) r(t) (\underline{K}_{np} + \underline{K}_p) + \frac{1}{2} r^t(t) \theta V(t) \tag{2.21}$$

where, the modal stiffness matrix ($\underline{K}$) of the piezoelectric beam, v25w, is written as:

$$\begin{aligned}\underline{K} &= \int_{v_{np}} z^2 \varphi^t(x)^{"} Y_{np} \varphi(x)^{"} dv_{np} + \int_{v_p} z^2 \varphi^t(x)^{"} Y_E^{11} \varphi(x)^{"} dv_p \\ &= \int_{v_{esp}} z^2 \varphi^t(x)^{"} Y_{esp} \varphi(x)^{"} dv_{esp} + 2\int_{v_c} z^2 \varphi^t(x)^{"} Y_c \varphi(x)^{"} dv_c + \\ &\quad 2\int_{v_{fr4}} z^2 \varphi^t(x)^{"} Y_{fr4} \varphi(x)^{"} dv_{fr4} + 4\int_{v_{ep}} z^2 \varphi^t(x)^{"} Y_{ep} \varphi(x)^{"} dv_{ep} + \\ &\quad 2\int_{v_p} z^2 \varphi^t(x)^{"} Y_E^{11} \varphi(x)^{"} dv_p\end{aligned} \tag{2.22}$$

The modal coupling matrix of the piezoelectric material is defined as:

$$\theta = \int_{v_p} z \varphi^t(x)^{"} e_{31}^T \psi(z) dv_p \tag{2.23}$$

The coupling coefficient is defined as follows:

$$e_{31}^T = d_{31} Y_{11}^E \tag{2.24}$$

where, d_{31} is the strain coefficient.

The internal electrical energy of the system can be expressed as:

$$W_{ie} = \frac{1}{2}\int_{v_p} \overline{E}_3^t \overline{D}_3 dv_p \tag{2.25}$$

Substitute the piezoelectric constitutive equations in Equation (2.10) into Equation (2.25), the internal electrical energy of the system can be rearrange as

$$W_{ie} = \frac{1}{2}[-r^t(t)\theta V(t) + V^2(t) C_p] \tag{2.26}$$

where, the capacitance matrix of the piezoelectric material is defined as:

$$C_p = \int_{v_p} \phi^t(z)\varepsilon^s_{33}\phi(z)dv_p \tag{2.27}$$

$$\varepsilon^s_{33} = \varepsilon^s_{r\,33} \times \varepsilon_0 \tag{2.28}$$

where, $\varepsilon^s_{r\,33}$ is the relative permittivity; ε^s_{33} is the dielectric constant; ε_0 is the electric constant.

The virtual work of the mechanical force includes generalised excitation force, $F(t)$, and the generalised resistive force due to damping effect, $\underline{D}\dot{r}(t)$, shown in Equation (2.29). The generalised excitation force is discussed in Section 2.3.3 of this chapter.

$$Q_r = F(t) - \underline{D}\dot{r}(t) \tag{2.29}$$

Damping is a dissipative energy, which attenuates the oscillation. The modal damping of the system is expressed as [56]:

$$\underline{D} = 2\xi\sqrt{\underline{MK}} \tag{2.30}$$

where, ξ is the damping ratio of the system, which is determined by using logarithmic decrement ($\underline{\delta}$) as shown in Equation 2.32 [57].

$$\xi = \frac{1}{\sqrt{1 + (\frac{2\pi}{\underline{\delta}})^2}} \tag{2.31}$$

$$\underline{\delta} = \frac{1}{k} ln \left| \frac{w(x,t)}{w(x,t+kT)} \right| \tag{2.32}$$

where, $w(x,t)$ is the peak displacement amplitude in time t, measured at, $L = x$; $x(x, t + kT)$ is the peak displacement amplitude at k periods away; T is the sampling rate.

The virtual work of the electric charge is:

$$Q_v = q(t)\delta V(t) \tag{2.33}$$

where, $q(t)$ is the electric charge output function; $V(t)$ is the voltage output function; $\delta(.)$ is the variation of the corresponding variable.

By substituting the kinetic energy in Equation (2.14), potential energy in Equation (2.21), internal electrical energy in Equation (2.26), and generalised excitation force and electrical domain in Equation (2.29) and (2.33) respectively into the electromechanical Lagrange equations in Equation (2.11) and (2.12) respectively, the equation of motion for the piezoelectric beam is presented as:

$$\underline{M}\ddot{r}(t) + \underline{D}\dot{r}(t) + \underline{K}r(t) - \theta V(t) = F(t) \tag{2.34}$$

$$\theta^t r(t) + C_p V(t) = q(t) \tag{2.35}$$

2.3.3 Generalised excitation force due to base excitation

To determine the vibration characteristics of the piezoelectric beam, a standard shaker test with base excitation is often applied. It is achieved by inducing

vibration at the clamp of a piezoelectric beam, allowing the beam to produce strain due to the inertia load of its own mass. To model the base excitation as an external force to the system, the cantilever beam is discretised to N_f elements with equal length Δx [3]. The base excitation motion will produce local inertia load that is applied on the kth element, which is expressed as:

$$f_k(t) = m\Delta x a_b(t) \tag{2.36}$$

where, m is the unit length mass of the piezoelectric beam; $a_b(t)$ is the base acceleration function. The base acceleration function is represented by a sine wave described as:

$$a(t) = G \times 9.81 sin(\omega_b t) \tag{2.37}$$

where, G is the applied G-force; ω_b is the angular frequency of the sine wave. In order to delineate the inertia load of the whole cantilever beam, the local inertia load along the beam is summed up. This study considers only the first mode of operation. The generalised excitation force due to base excitation can then be expressed as:

$$F_b(t) = a(t) \sum_{k=1}^{N_f} m\varphi(x_k) \tag{2.38}$$

2.4 Numerical simulation

The mathematical model developed in Section 2.3 is simulated in MATLAB using the function 'lsim', which is able to simulate time response of a dynamic

system based on arbitrary inputs. The equation of motion shown in Equation (2.34) and (2.35) have to be converted into state-space model in order to comply with the format of the MATLAB function. The state-space model format for the 'lsim' function is given as:

$$\dot{\overline{x}} = \overline{\overline{A}}\overline{x} + \overline{\overline{B}}\overline{u} \tag{2.39}$$

$$\overline{y} = \overline{\overline{C}}\overline{x} + \overline{\overline{D}}\overline{u} \tag{2.40}$$

where, $\overline{x}$, $\overline{y}$, and $\overline{u}$ are the state, output, and input vector respectively; $\overline{\overline{A}}$, $\overline{\overline{B}}$, $\overline{\overline{C}}$, and $\overline{\overline{D}}$ are the state, input, output, and feedforward matrix respectively. The mechanical domain of the equation of motion for the piezoelectric beam presented in Equation (2.34) can be rearranged as:

$$\ddot{r}(t) = \underline{M}^{-1}F(t) - \underline{M}^{-1}\underline{D}\dot{r}(t) - \underline{M}^{-1}\underline{K}r(t) + \underline{M}^{-1}\theta V(t) \tag{2.41}$$

By performing differentiation with respect to time for both side of the electrical domain of the equation of motion for the piezoelectric beam in Equation (2.35), it can be rewritten as:

$$\dot{V}(t) = C_p^{-1}\dot{q}(t) - C_p^{-1}\theta^t\dot{r}(t) = C_p^{-1}R^{-1}V(t) - C_p^{-1}\theta^t\dot{r}(t) \tag{2.42}$$

where, the rate of electric charge flow, $\dot{q}(t)$, equals to electric current, which can be written as voltage (V) over resistance (R):

$$\dot{q}(t) = R^{-1}V(t) \tag{2.43}$$

The rearranged piezoelectric beam equation of motion shown in Equation (2.41) and (2.42) can be converted to state-space model as follows:

$$\overline{x} = \begin{bmatrix} r(t) \\ \dot{r}(t) \\ V_1 \\ V_2 \end{bmatrix} \tag{2.44}$$

$$\overline{u} = F \tag{2.45}$$

$$\overline{y} = \begin{bmatrix} V_1 & V_2 \end{bmatrix} \tag{2.46}$$

$$\overline{\overline{A}} = \begin{bmatrix} 0 & 1 & 0 & 0 \\ -\underline{M}^{-1}\underline{K} & -\underline{M}^{-1}\underline{D} & \underline{M}^{-1}\theta & \underline{M}^{-1}\theta \\ 0 & -C_p^{-1}\theta^t & C_p^{-1}R^{-1} & 0 \\ 0 & -C_p^{-1}\theta^t & 0 & C_p^{-1}R^{-1} \end{bmatrix} \tag{2.47}$$

$$\overline{\overline{B}} = \begin{bmatrix} 0 \\ \underline{M}^{-1} \\ 0 \\ 0 \end{bmatrix} \tag{2.48}$$

$$\overline{\overline{C}} = \begin{bmatrix} 0 & 0 & 1 & 1 \end{bmatrix} \tag{2.49}$$

$$\overline{\overline{D}} = 0 \tag{2.50}$$

where, V_1 and V_2 are the voltages generated by the two piezoelectric layers; F is the generalised excitation force. A table of the parameters used in the simulation

is provided in Table 2.3. The dynamical response of the system subjected to an externally applied force could then be simulated.

Table 2.3: Common parameters (first mode) used in the simulation of the theoretical results.

Parameter	**Symbol**	**Value**
Modal mass	$\underline{M}$	0.97587
Modal stiffness	$\underline{K}$	5.8161×10^5
Modal damping	$\underline{D}$	18.08
Modal coupling	θ	0.0381
Capacitance	C_p	8.8518×10^{-8}

2.5 Experiment validation of the piezoelectric beam model

The validation of the piezoelectric beam model presented in Section 2.3 is conducted here through experimental studies. Numerical simulation is performed in MATLAB using the state-space model derived in Equations (2.44 - 2.50). Base excitation is introduced to the clamped piezoelectric beam using a shaker. This section presents the experiment methodology and this is followed by results and discussions section.

2.5.1 Experiment methodology

An off-the-shelf bimorph PZT piezoelectric beam (Mide-v25w) is utilised in this study. The piezoelectric layers are connected in series and the voltage measured is under open circuit condition. The piezoelectric beam is clamped on an electromagnetic shaker (Bruel & Kjaer, Modal Exciter-Type 4824) that produces vibration of different G-forces as base excitation motion to the piezoelectric beam. A function generator outputs sine waves of different frequencies. The sine wave signal is amplified by a power amplifier to drive the electromagnetic shaker and provide different G-forces.

To measure the frequency and G-force of the sine wave, an accelerometer (Myduino-Triple Axis Accelerometer MMA7361) is mounted on top of the piezoelectric beam clamp. The accelerometer is powered by a supply voltage of 3.3 V, which is regulated by a voltage regulator installed in the signal interfacing circuit. The signal interfacing circuit acts as a signal interface medium between the data logger (NI-USB6008), piezoelectric beam, and accelerometer. The specifications for the data logger is given in Appendix A.1. The signals from the accelerometer and piezoelectric beam are recorded by the data logger and the results are stored in a laptop using a software provided by LabView, Signal Express. The sampling rate of the accelerometer and voltage produced by the piezoelectric beam is set as 1 kHz.

The experiment setup schematics and the experiment setup overview are depicted in Figure 2.3 and Figure 2.4 respectively. The enlarged view of the

data logger, voltage regulator and signal interfacing circuit, accelerometer and piezoelectric beam is presented in Figure 2.5.

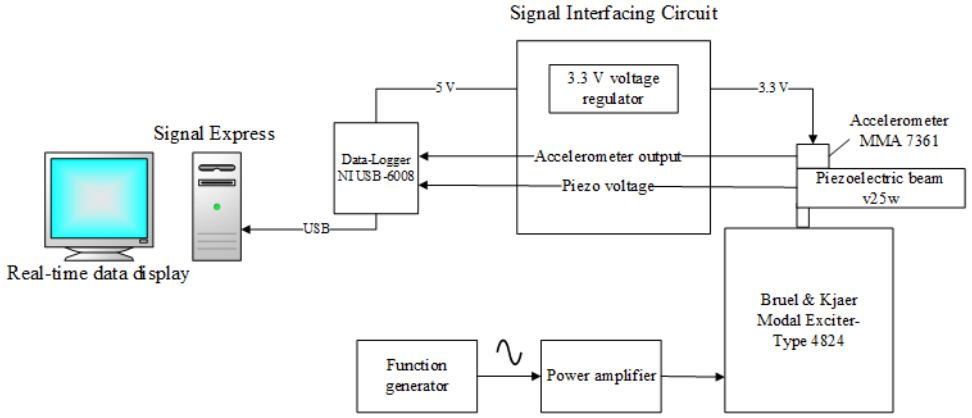


Figure 2.3: Schematics of the experiment setup.

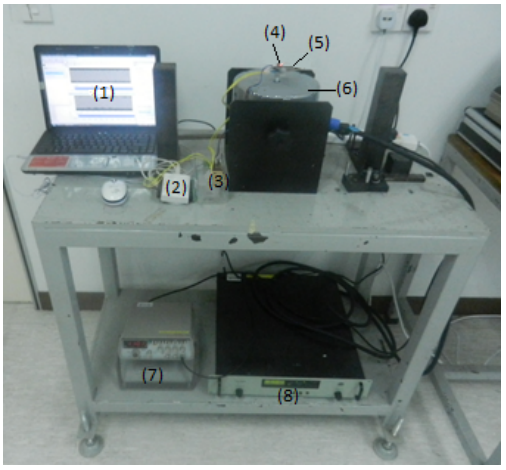


Figure 2.4: Experiment setup: (1) laptop; (2) data logger; (3) voltage regulator and signal interfacing circuit; (4) accelerometer; (5) piezoelectric beam; (6) electromagnetic shaker; (7) function generator; (8) power amplifier.

2.5.2 Results and discussion

The first mode natural frequency of the piezoelectric beam and the voltage produced by the piezoelectric beam are investigated in this section. The first mode

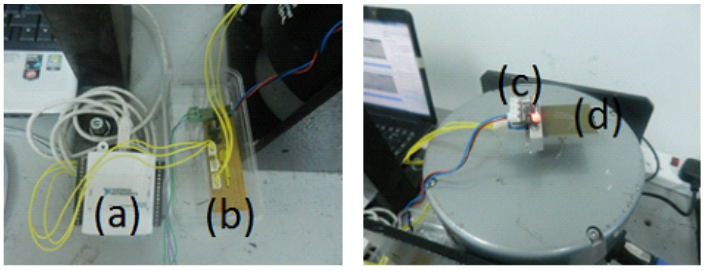


Figure 2.5: Enlarged view of (a) data logger: NI-USB6008; (b) 3.3 V voltage regulator and signal interfacing circuit; (c) accelerometer: MMA7361; (d) piezoelectric beam: v25w.

natural frequency of the piezoelectric beam was achieved by tuning the function generator until a local maximum point is observed in the generated voltage. On the other hand, the first mode natural frequency of the theoretical results can be obtained from the frequency response graph by performing Fast Fourier Transform (FFT) on the voltage time response graph simulated from the theory using MATLAB.

In order to compare the experimental and theoretical frequency response graphs, results obtained from excitation force of 0.5 g are chosen for discussion purpose. The experimental and theoretical frequency response graphs due to 0.5 g base excitation are given in Figure 2.6. The first mode natural frequency of the experimental and theoretical result is 120.1 Hz and 122.6 Hz respectively. From Figure 2.6, the theoretical result showed good agreement with the experimental result, with a percentage error in first mode natural frequency of 2.04 %.

In order to validate the mathematical model, base excitation of four different G-forces (0.25 g, 0.375 g, 0.5 g, and 1 g) are conducted in the experiment and simulation. The values of G-force utilised in this study are based on the datasheet of the piezoelectric beam (Mide-v25w). The voltage time response

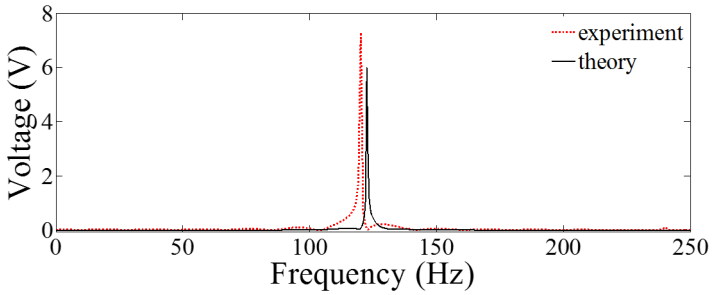


Figure 2.6: Frequency response graph (first mode) with base excitation of 0.5 g.

graphs for the experimental and theoretical results are depicted in Figure 2.7. The experimental and theoretical peak voltage output along with the percentage error of the respective G-forces are tabulated in Table 2.4.

From Table 2.4, the peak voltages recorded from the experiment and estimated by the numerical simulation showed a positive trend as the G-force increases. As the vibration amplitude increases, more strain will be induced to the beam structure and more voltage will be generated. The percentage differences between the experimental and theoretical results for the four G-forces can be found in Table 2.4. The highest percentage difference (25.45 %) is found when 1 g of base excitation was induced to the piezoelectric beam. In overall, the theoretical results were in good consensus with the experimental results.

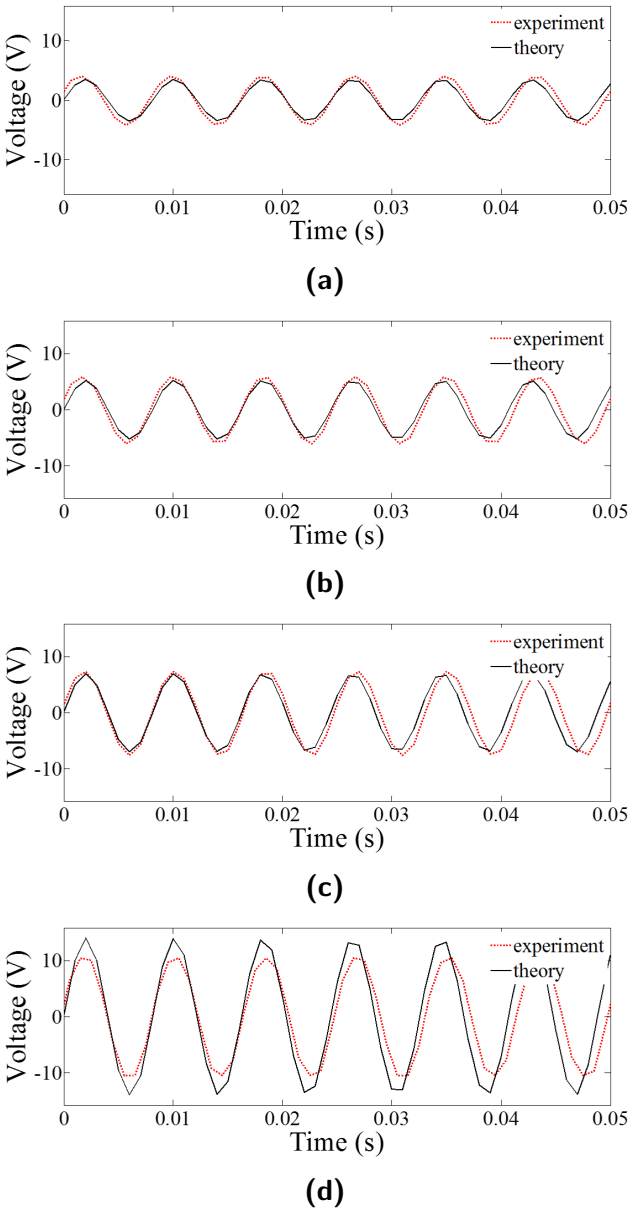


Figure 2.7: Voltage time response graphs with base excitation of: (a) 0.25 g; (b) 0.375 g; (c) 0.5 g; (d) 1 g.

For base excitation application, a piezoelectric beam has to operate at its resonant state in order to produce maximum power output. When the vibration source is out of resonance with the piezoelectric beam, the performance of the energy harvester could deteriorate [58]. To overcome this issue, several methods

Table 2.4: The experimental and theoretical peak voltages of different G-force with its respective percentage difference.

G-force (g)	**Experiment (V)**	**Theory (V)**	**Percentage difference (%)**
0.250	4.16	3.48	19.54
0.375	6.03	5.25	14.86
0.500	7.64	6.99	9.30
1.000	10.43	13.99	25.45

were proposed in literature to optimise the piezoelectric beam energy harvester under base excitation, such as bandwidth widening [59] and frequency tuning [60].

In the case of raindrop impact energy harvesting using piezoelectric beam, the piezoelectric beam is impact-driven. When the raindrop impacts the surface of the piezoelectric beam, it oscillates in resonant frequency. After the impact, the output voltage will exhibit two distinct stages, first with a logarithmic growth and followed by an exponential decay [32]. The dynamical response of a piezoelectric beam subjected to raindrop impact is covered in Chapter 3.

2.6 Chapter conclusion

In this chapter, detailed derivation on the piezoelectric beam model is presented. Modal analysis of a cantilever beam is studied and the mode shape is derived. The mass normalisation is performed by using the orthogonality condition of the mode shape. The piezoelectric beam model is developed by applying the

constitutive equation of a linear piezoelectric material, Rayleigh-Ritz Theorem, and Lagranges equations for electromechanical systems. The final form of the developed piezoelectric beam model is able to predict the voltage output response of the piezoelectric layers, and able to describe the dynamical response of the piezoelectric beam structure. Furthermore, the generalised excitation force due to base excitation is derived to facilitate the study of vibration characteristics in a shaker test.

The piezoelectric beam model is validated by performing an experiment test using an electromagnetic shaker. Results revealed that the first mode natural frequency of the piezoelectric beam when measured in open circuit is 122.6 Hz. Voltage time response graphs were obtained by applying four different G-forces in the experiment and simulation model. Overall, the experimental results showed good agreement with the theoretical results, with a percentage difference range of 9.30 % to 25.45 %.

Chapter 3

Dynamics of the rain harvester subjected to water droplet impact

3.1 Introduction

In Chapter 2, the equation of motion for the piezoelectric beam is developed. This chapter will investigate the dynamics of water droplet impact on the surface of a piezoelectric beam. Water droplet impact on a surface is a well-established research field. This study has been applied in myriads of fields, to name a few: ink-jet printing, and spray coating [61, 62]. In droplet impact energy harvesting using piezoelectric beam, the dynamics of a water droplet impact will affect

the electrical energy generation. Water droplet impact on a piezoelectric beam can be modelled by following the analogy of a ball impacting a plate and such impact can be assumed to be perfectly inelastic impact [33, 38]. In actual case, the water droplets do not stick to the piezoelectric beam, as suggested by the perfectly inelastic impact model. The water droplet will spread, recoil, or splash upon impact. Guigon et al. [33] reported that the reduction in energy generation by the piezoelectric energy harvester is caused by the splashing phenomenon.

Mao et al. [42] showed that the water droplet energy before impact is not fully converted to strain and electrical energy after the impact. Energy is lost due to spreading, recoiling, and splashing events. According to Mao et al. [42], water droplet impact exhibits four stages: (a) before impact, (b) maximum spread, (c) maximum recoil/rebound, and (d) equilibrium. Before impact, the droplet impact energy consists of kinetic energy, surface energy, and potential energy. As the water droplet reaches the maximum spread diameter after impact, the liquid flow direction changes from spreading outwards to recoiling inwards. During the maximum spread, the kinetic energy is converted to surface energy. The droplet contains maximum surface energy as it reaches maximum spread diameter. This will cause the water droplet to recoil. In the maximum recoil/rebound stage, the droplet possesses potential and surface energy but no kinetic energy as it is at its maximum height. In the final stage, the equilibrium stage, the water droplet has minimum energy, which equals to the static surface energy. Several studies demonstrated that the surface wettability and roughness [42–44] will affect the spreading and recoil stages. This has increased the difficulty in the modelling of

the droplet impact force.

Various analytical models such as hertz contact theory, elastic foundation model, potential flow theory, and average momentum force were studied by Mangili et al. [44]. Among the impact force estimated by the analytical models, variation of one or two orders of magnitude are reported. Moreover, the result estimated by the numerical simulation using Finite Element Method had over-estimated the maximum deformation of the substrate by approximately seven times compared to the experimental data. Hence, the dynamics of water droplet impact on a deformable surface requires further investigation.

The impact force of an impinging water droplet could be measured by using a calibrated piezoelectric beam via bead drop impact method [63]. The calibration was conducted by using a high-speed photography technique to measure the rebound height of the bead impacted on a PVDF piezoelectric film. However, when the bead impacts on the piezoelectric beam, the beam will deform and the bead will not rebound vertically. This causes complication in estimating the impact coefficient by using photography technique.

In this chapter, the dynamics of the piezoelectric beam subjected to water droplet impact is investigated. It is observed that as more water droplets are introduced, they will merge and accumulate on the surface of the piezoelectric beam. The water droplet accumulation is modelled as a discrete function of droplet number count. Added mass coefficient is introduced to describe the amount of water droplet accumulated. The added mass coefficient can be related

to the ratio of the modal mass of the water layer formed to the modal mass of the piezoelectric beam structure without any water layer.

The dynamics of a single water droplet impact is studied in this chapter. Impulse Momentum Theorem is used to model the average impact force of a water droplet impact. In order to incorporate the post impact behaviour of a water droplet impact, an impact coefficient is introduced. The impact coefficient is modelled as a discrete function of droplet number count. This is because the impact coefficient varies when the modal mass of the water layer formed on the surface of the piezoelectric beam varies. The model is validated through experimental studies in this chapter.

Subsequently, the model is further extended to multiple water droplet impact model by incorporating the analysis of varying drop period and position. According to the literature, most of the experimental and theoretical works conducted considered only single droplet test [33–35, 37]. Single droplet test could not fully capture the behaviour of a raindrop impact energy harvester in actual rain scenario. During actual rain, raindrops will accumulate on the surface of the piezoelectric beam, and a water layer will be formed. The water layer formed on the surface of the piezoelectric beam will change the dynamic response of the piezoelectric beam and has yet to be studied.

In this chapter, the multiple droplet impact model captures the response of the piezoelectric beam when it is excited by water droplet impinging at different locations on the piezoelectric beam at different time. The impact position study is conducted by fixing the water droplet size and impact height. To validate the

model, three different rain rates were investigated and they are categorised as light stratiform rain (LSR), moderate stratiform rain (MSR), and heavy thundershower (HT). The performance of the energy harvester is evaluated by using root mean square (RMS) voltage and energy accumulated over a fixed time period of 12 s.

This chapter is organised as follows: Section 3.2 presents the modelling of the piezoelectric beam with water layer; the modelling of the piezoelectric beam subjected to single droplet impact is discussed in Section 3.3; the single droplet impact model is validated using experimental result in Section 3.4; Section 3.5 highlights the dynamics of the harvester subjected to multiple droplet impact; the experiment validation of the multiple droplet impact model is presented in Section 3.6; lastly, Section 3.7 concludes this chapter.

3.2 Modelling of the piezoelectric beam with water layer

The water layer accumulation on the surface of the piezoelectric beam is modelled as an added mass effect. The water layer formed on the surface of the beam acts as a resistive force and an artificial mass on the piezoelectric beam. This can be treated as an added-mass effect [64]. Additional parameter matrices due to the formed water layer are added into the mechanical domain of the equation of

motion in Equation (2.34) as:

$$(\underline{M} + \underline{M}_w)\ddot{r}(t) + (\underline{D} + \underline{D}_w)\dot{r}(t) + (\underline{K} + \underline{K}_w)r(t) - \theta V(t) = F(t) \tag{3.1}$$

where, $(.)_w$ indicates that the corresponding parameter matrix is of the water layer. The modal parameter matrices are related to the mode shape of the piezoelectric beam. Moreover, the shape of the water layer formed on the surface of the piezoelectric beam is irregular. Therefore, it is difficult to estimate the parameter matrices of the water layer. Furthermore, the modal parameter matrices do not have a unique value due to different scaling method utilised to define the mode shape [65]. Since the ratios between the modal parameters are unique, they are listed as:

$$\omega^2 = \frac{\underline{K}}{\underline{M}} \tag{3.2}$$

$$\omega_d = \omega\sqrt{1 - \zeta^2} \tag{3.3}$$

$$\zeta = \frac{\underline{D}}{2\sqrt{\underline{K}\underline{M}}} \tag{3.4}$$

where, ω is the natural frequency of the piezoelectric beam; ω_d is the damped natural frequency of the piezoelectric beam. To simplify the derivation process the following parameters are introduced:

$$\underline{M}_a = \underline{M} + \underline{M}_w$$

$$\underline{D}_a = \underline{D} + \underline{D}_w$$

$$\underline{K}_a = \underline{K} + \underline{K}_w \tag{3.5}$$

$$\omega_a^2 = \frac{\underline{K}_a}{\underline{M}_a} \tag{3.6}$$

where, $(.)_a$ indicates that the corresponding parameter matrix is inclusive of the water layer. By dividing Equation (3.6) with Equation (3.2):

$$\frac{\omega_a^2}{\omega^2} = \left(1 + \frac{\underline{K}_w}{\underline{K}}\right)\left(1 + \frac{\underline{M}_w}{\underline{M}}\right)^{-1} \tag{3.7}$$

By taking the modal stiffness matrix of the water layer as zero ($\underline{K}_w = 0$), which is a reasonable assumption to most structures according to Sedlar et al. [65], Equation (3.7) can then be rewritten as:

$$\frac{\omega_a^2}{\omega^2} = \left(1 + \frac{\underline{M}_w}{\underline{M}}\right)^{-1} \tag{3.8}$$

By substituting Equation (3.3) into Equation (3.8):

$$\frac{\omega_a^2}{\omega^2} = \frac{\omega_{da}^2}{\omega_d^2} \times \frac{1-\zeta^2}{1-\zeta_a^2} = \left(1 + \frac{\underline{M}_w}{\underline{M}}\right)^{-1} \tag{3.9}$$

After some rearrangements, the added mass coefficient can be obtained as:

$$C_a = \frac{\underline{M}_w}{\underline{M}} = \frac{\omega_d^2(1-\zeta_a^2)}{\omega_{da}^2(1-\zeta^2)} - 1 \tag{3.10}$$

By substituting the added mass coefficient into the modal damping matrix in Equation (2.30), the modal damping matrix that incorporates the added mass effect is written as:

$$\underline{D}_a = 2\zeta\sqrt{(1+C_a)\underline{MK}} \tag{3.11}$$

Similarly, the mechanical domain of the equation of motion, Equation (2.34), with added mass effect can be rewritten as:

$$(1 + C_a)\underline{M}\ddot{r}(t) + \underline{D}_a\dot{r}(t) + \underline{K}r(t) - \theta V(t) = F(t) \tag{3.12}$$

To accommodate the analysis of the water layer accumulation process, the added mass coefficient, modal damping matrix, and mechanical domain of the equation of motion with added mass effect in Equation (2.10), (2.11), and (2.12) respectively are discretised with a function of drop count 'n' as:

$$C_a(n) = \frac{[1 - \zeta_a^2(n)]\omega_d^2(1)}{[1 - \zeta^2(1)]\omega_d^2(n)} - 1 \tag{3.13}$$

$$\underline{D}_a(n) = 2\zeta(n)\sqrt{[1 + C_a(n)]\underline{MK}} \tag{3.14}$$

$$\underline{M}_a(n)\ddot{r}_n(t) + \underline{D}_a(n)\dot{r}_n(t) + \underline{K}r_n(t) - \theta V_n(t) = F_n(t) \tag{3.15}$$

3.3 Modelling of piezoelectric beam subjected to single droplet impact

This section presents a mathematical model of piezoelectric energy harvester subjected to single droplet impact. The modelling of generalised excitation force due to the nth water droplet impinging the piezoelectric beam is presented. The impact is modelled by using the Impulse Momentum Theorem. This is followed

by the description of the water droplet behaviour before and after the impact. Lastly, a novel method is introduced to determine the impact coefficient.

The generalised excitation force due to the nth water droplet impacting at length position, x, on the piezoelectric beam can be written as:

$$F_{s,n}(t) = f_{avg}(n)\varphi(x)\eta_s(t) \tag{3.16}$$

$$\eta_s(t) = \begin{cases} 1, & 0 \leq t \leq \tau \\ 0, & otherwise \end{cases} \tag{3.17}$$

where, $\eta_s(t)$ is the pulse function for single droplet impact; f_{avg} is the average impact force; τ is the impact duration.

The impact duration of the impinging water droplet is written as [66]:

$$\tau = \frac{D_w}{v_w} \tag{3.18}$$

where, D_w is the water droplet diameter; v_w is the water droplet impact velocity. The impact duration expression shown in Equation (3.18) is a fundamental expression with some simplified assumptions of the impact phenomena [66].

The impact velocity of a free falling water droplet is dependent on its drop height. The impact velocity (v_w) of the impinging water droplet with a radius of R_w, falling from a drop height of H, is given as [43]:

$$v_w(H) = \sqrt{\frac{g}{A}(1 - e^{-2AH})} \tag{3.19}$$

$$A = \frac{3c_f \rho_{air}}{8R_w \rho_w} \tag{3.20}$$

where, A is a constant; g is the gravity constant; ρ_{air} and ρ_w are the density of air and water respectively; c_f is the friction coefficient of the water droplet.

The average impact force of an impinging water droplet is derived by using the Impulse Momentum Theorem. According to the Impulse Momentum Theorem, the change in momentum of an object is due to the impulsive force acting on it.

Assume the time of a water droplet hitting the beam is at t_1, and the time after impact is at t_2, where $(t_2 = t_1 + \tau)$. By relating to the Impulse Momentum Theorem, the change in momentum of the nth impinging water droplet is due to the impulsive force exerted by the piezoelectric beam, f_n, which is written as:

$$\int_{t_1}^{t_2} f_n(t)dt = \Delta p = p_2 - p_1 \tag{3.21}$$

where, p_1 and p_2 are the momentum of water droplet before impact and after impact respectively.

When water droplet impacts on a surface, momentum loss will occur as portion of it is not absorbed by the piezoelectric beam. The lost in momentum for a water droplet impact can be related to splashing, spreading and partial recoil motion of the water droplet after impact. Splashing can be determined by using the impact parameter, Km [67]. The impact parameter governs the mode

of water droplet deformation after impact, which is given as:

$$Km = We^{0.5} Re^{0.25}$$

$$We = \rho_w D_w v_w^2 / \sigma_w \tag{3.22}$$

$$Re = \rho_w D_w v_w / \mu_w$$

where, We is Weber Number; Re is Reynolds Number; σ_w is the ratio of inertial force to surface tension ($\sigma_w = 0.07$ Nm^{-2}); μ_w is dynamic viscosity ($\mu_w = 0.001$ Pa s); D_w is diameter of water droplet. The impinging water droplet will splash if the impact parameter, Km, is higher than 57.7. During splashing, the impinging water droplet will be separate into multiple satellite droplets and splash out from the point of impact. When splashing occurs, the momentum of the water droplet impact will not be conserved.

Spreading of a water droplet after impact will cause loss in momentum of the impinging water droplet after impact. The loss in momentum is due to viscous effect, surface energy, and kinetic energy contributed by the liquid motion during spreading [44]. Water droplet will recoil when the droplet reaches maximum spread diameter due to the excessive surface energy. The behaviour of water droplet recoil after impact can be related to the impact surface roughness [44]. According to Mangili et al. [44], the recoil phase of the droplet on a hard substrate is shorter when compared to a softer substrate.

Figure 3.1 illustrates the moment before and after impact, where portion of

the water droplet will spread or splash, while the remaining portion of the water droplet will stick on the beam and travel with it.

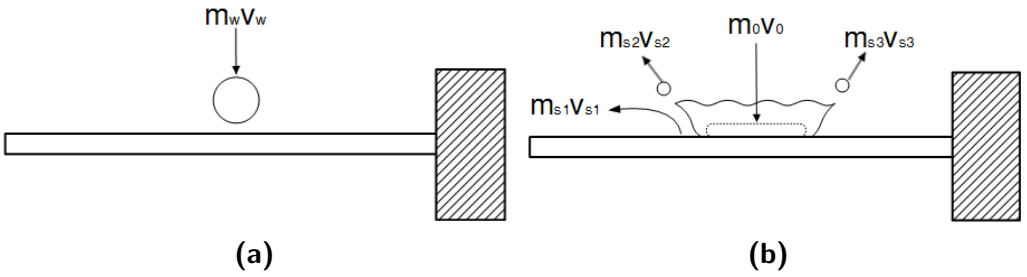


Figure 3.1: Schematics diagram of the side view of the piezoelectric beam (a) moment before impact and (b) the after impact.

The momentum of the water droplet before and after impact is written as:

$$p_1 = m_w v_w$$

$$p_2 = m_0 v_0 + \sum(m_s v_s) \tag{3.23}$$

where, m_w is the water droplet mass; $(.)_0$ indicates the portion of water droplet that sticks on the beam after the impact, with $v_0 = 0$; $(.)_s$ indicates the portion of water droplet that spread or splashed after the impact.

The mass and velocity of the satellite droplets are hard to determine as they will spread or splash radially outwards from the point of impact. The mass of the impinging water droplet is conserved after the impact ($m_w = m_0 + \sum m_s$). Since the satellite droplets do not travel in the same direction of the beam, it is safe to assume that the sum of momentum after the impact are less than the

momentum before the impact ($p_2 < p_1$). As a result, an impact coefficient (C_i) is introduced as shown in Equation (3.24) to describe the loss of momentum of the impinging water droplet after impact due to spreading, splashing, spreading, or recoil.

$$p_2 = C_i p_1 \tag{3.24}$$

By substituting Equation (3.24) into Equation (3.21), the impact force exerted by the piezoelectric beam is rewritten as:

$$\int_{t_1}^{t_2} f_n(t)dt = (C_i - 1)p_1 \tag{3.25}$$

The impact force exerted by the piezoelectric beam to the water droplet can be rewritten as an average force applied over the impact duration, τ:

$$\int_{t_1}^{t_2} f_n(t)dt = f_{avg}(n)\tau \tag{3.26}$$

By substituting Equation (3.23) and (3.26) to Equation (3.25), and applying Newtons third law of motion, the average force applied to the piezoelectric beam by the impinging water droplet is expressed as:

$$f_{avg}(n) = \frac{(1 - C_i)m_w v_w}{\tau} \tag{3.27}$$

The average impact force can be modelled as a discrete function of droplet number, n, Equation (3.27) is written as:

$$f_{avg}(n) = \frac{[1 - C_i(n)]m_w v_w}{\tau} \tag{3.28}$$

By considering only the first mode of vibration and substituting Equation (3.28) into the mechanical domain of the equation of motion for the piezoelectric beam, Equation (3.15), the impact coefficient can be derived as:

$$C_i(n) = \frac{1}{b_{max}} \sum_{b=1}^{b_{max}} \left\{ 1 - \frac{[\underline{M}_a(n)\ddot{r}_n(bT) + \underline{D}_a(n)\dot{r}_n(bT) + \underline{K}r_n(bT) - \theta V_n(bt)]\tau}{m_w v_w \varphi(x)\eta(bT)} \right\} \tag{3.29}$$

where, b is the number of sampling element, T is the sampling rate, and $b_{max}T = \tau$; the voltage output (V_n) as well as the generalised coordinates for displacement (r_n), velocity ($\dot{r}_n$), and acceleration ($\ddot{r}_n$) are determined experimentally. The generalised coordinates are written respectively as:

$$r_n(t) = \frac{w_n(x,t)}{\varphi(x)}; \qquad \dot{r}_n(t) = \frac{\dot{w}_n(x,t)}{\varphi(x)}; \qquad \ddot{r}_n(t) = \frac{\ddot{w}_n(x,t)}{\varphi(x)} \tag{3.30}$$

3.4 Experiment validation of the single droplet impact model

When a water droplet collides on the surface of a piezoelectric beam, it will splash, spread, or recoil. It is discussed in the previous section that the post-impact behaviour of the water droplet will result in the loss of momentum. The

loss of momentum is described by using an impact coefficient. To obtain the impact coefficient, a time course study on the successive water droplet impact on the piezoelectric beam was conducted.

In this section, the theoretical model developed in Section 3.3 is validated by both simulation and experimental studies. The dynamical response is simulated in MATLAB. In this study, successive water droplet impacts were treated as individual excitation. It considered the first mode of vibration only. This is to facilitate the analysis of each individual water droplet impact. Damping ratio and damped natural frequency were extracted from the individual voltage responses to calculate the added mass coefficient using Equation (3.10). The impact coefficient for every droplet can be estimated by using Equation (3.29).

The post impact behaviour of water droplet impact is investigated through the accumulation of water droplets. Static camera images of different drop occasions, voltage response graphs, and frequency response graphs are utilised to analyse the post impact behaviour of the water droplet impact. In addition, the peak and root mean square (RMS) voltage of each drop are computed.

3.4.1 Experiment methodology

The schematics and photograph of the experimental setup are provided in Figure 3.2. In order to conduct a time course study on the successive water droplet impact, a steady flow of water droplet is produced by using a peristaltic pump (Cole Parmer-Masterflex L/S series). The specifications of the peristaltic pump is

provided in Appendix A.2. The peristaltic pump is able to produce a consistent water droplet size with a fixed time interval by pumping water from a water reservoir. The flow of the water droplet is set in a way that the water droplets would impact on the same location every one second time interval. In order to generate a consistent water droplet size, a 21G gauge syringe needle is installed on a retort stand with a silicon tube. The 21G gauge syringe is able to produce a consistent water droplet with diameter of 2.96 mm. The tip of the syringe is elevated 0.25 m above the piezoelectric beam and it is positioned so that water droplets could impact the centre of beam. The impact velocity is estimated as 2.15 m/s by using Equation (3.19).

The water droplet diameter and impact velocity were measured using a laser precipitation monitor sensor (Thies CLIMA-5.14100.10.000). The specifications of the laser precipitation monitor sensor is presented in Appendix A.4. A rig was fabricated by using slotted angle bar. This serves as the sensor mounting rig for the laser precipitation monitor sensor. The laser precipitation monitor sensor measures the size of the water droplets by using an infrared beam via laser diode and optics. The receiver, which consists of a photo diode with a lens, is able to capture the optical intensity and transform the information into electrical signal. The signal is converted from RS-485 cable to Universal Serial Bus (USB) before conveying to a computer. A data-logging program is developed using MATLAB to record the water droplet diameter and its respective impact velocity.

The voltage generated by the piezoelectric beam is recorded using a data logger (NI-USB6008). The PZT layers of the piezoelectric beam (Mide-v25w)

are connected in series and it is measured across a 15 kΩ load resistor.

A laser vibrometer (MicroEpsilon-ILD1700-10) is installed directly under the piezoelectric beam to measure the tip displacement of the beam. The laser vibrometer measures the tip displacement of the beam by using the principle of optical triangulation, where a visible and modulated point of light is projected onto the target surface. The recorded signal is delivered into laptop via RS-485 cable in real time and it is recorded by using a software, ILD1700 Tool. The specifications of the laser vibrometer is provided in Appendix A.3.

3.4.2 Estimation of the impact coefficient

In order to obtain the impact coefficient for every cycle of water droplet impact, the added mass coefficient and the damping ratio of every cycle have to be known. The damping ratio of each droplet number can be estimated using logarithmic decrement from the voltage response graphs using Equation (2.31). The damping ratio obtained from experiment results are fitted with an eight-term sum of sine model using MATLAB:

$$\xi(n) = \sum_{i=1}^{8} \overline{p}_i sin(\overline{q}_i n + \overline{r}_i) \tag{3.31}$$

where, '$\overline{p}$' is the amplitude; '$\overline{q}$' is the frequency; '$\overline{r}$' is the phase constant for each sine wave term.

The damping ratio of each water droplet impact shown in Figure 3.3 demonstrates that the fitted curve is able to describe the approximate trend of the

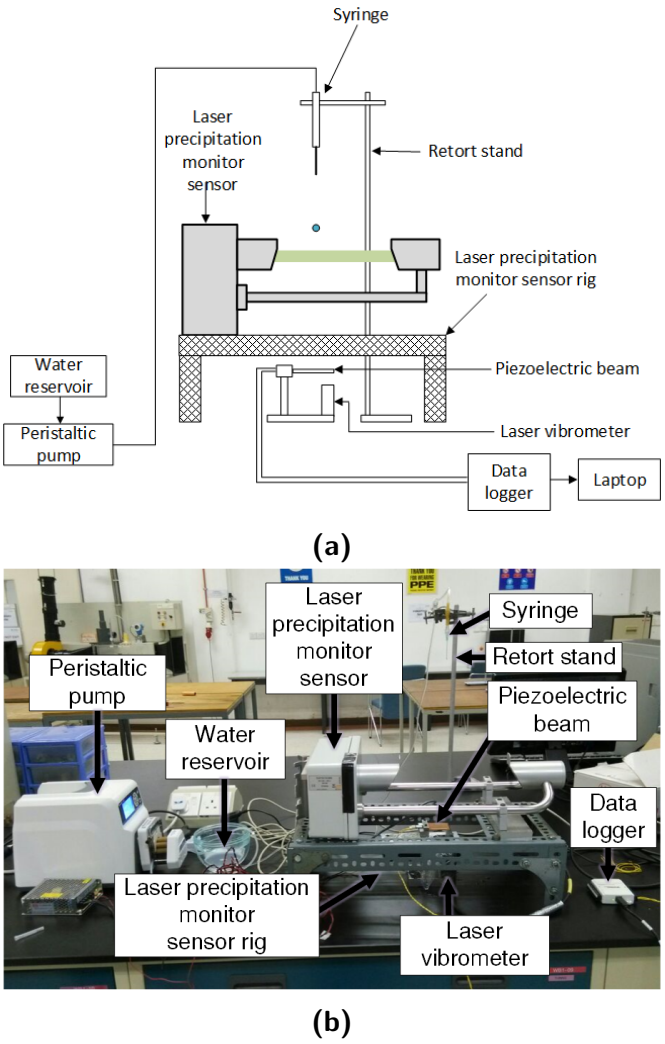


Figure 3.2: The (a) schematics and (b) photograph of the experimental setup.

damping ratio well. The oscillatory trend of the damping ratio can be attributed to the change in the water layer thickness as it was accumulating. When the water droplet was accumulating at $n < 274$, the water layer formed on the surface would experience a prompt change in thickness and expand radially when its surface tension could not hold its shape. As a result, more fluctuation in damping ratio was observed at this region. At $n \geq 274$, the surface area of the water layer was larger when comparing to $n < 274$. As a result, less fluctuation

in damping ratio was observed when $n \geq 274$.

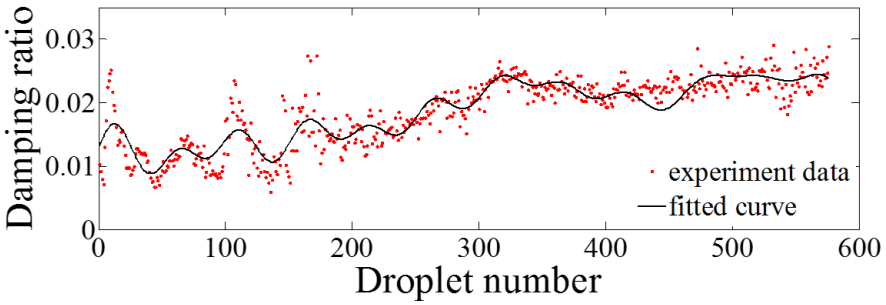


Figure 3.3: Damping ratio against droplet number.

According to Equation (2.31), damping ratio and damped natural frequency for each droplet impact have to be known in order to obtain the added mass coefficient. The damped natural frequency can be extracted by performing Fast Fourier Transform (FFT) on the voltage time response graphs of respective droplet number to obtain the frequency response graph. The added mass coefficient and the first mode damped natural frequency for the investigated droplet number are plotted in Figure 3.4 and Figure 3.5 respectively.

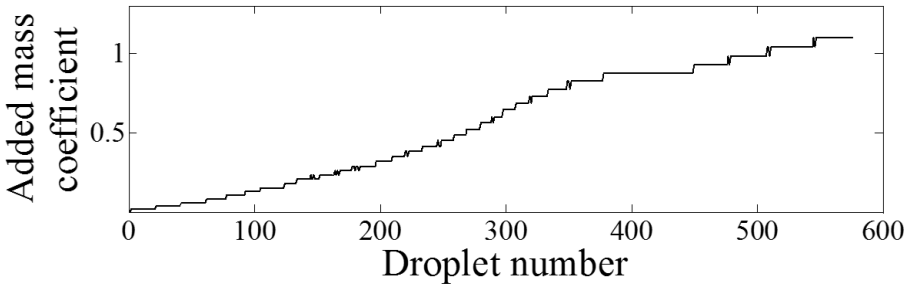


Figure 3.4: Added mass coefficient against droplet number.

The added mass coefficient is defined as a ratio of the modal mass of the water layer and the modal mass of the piezoelectric beam without water layer

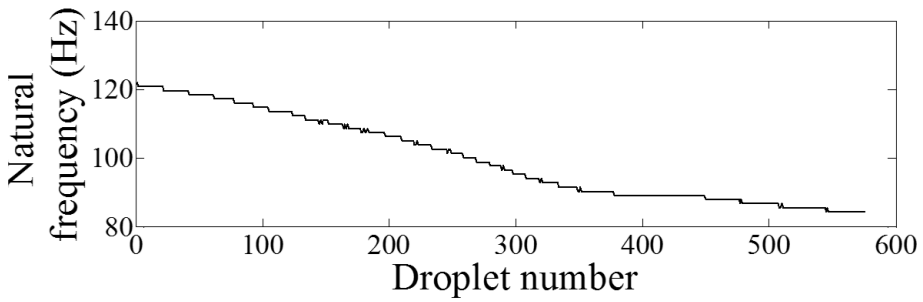


Figure 3.5: First mode natural frequency against droplet number.

in Equation (3.10). As the droplet number increases, the modal mass of the water layer increases as well. Therefore an increase in added mass coefficient can be observed in Figure 3.4. As the modal mass of the water layer increases, the damped natural frequency of the system will decrease, as shown in Figure 3.5. The maximum added mass coefficient and the lowest first mode damped natural frequency were measured to be 1.1 and 84.23 Hz respectively. A plateau was observed in both Figure 3.4 and Figure 3.5 at $378 < n < 449$. This can be explained by the geometry and the thickness of the formed water layer. As the surface area of the water layer became higher, more water droplets are needed in order to increase the modal mass of the water layer. Therefore, a plateau was observed at this region. After $n = 449$, the added mass coefficient was found to be increasing while the damped natural frequency of the system is decreasing before the water layer started to spill at $n = 576$.

By using Equation (3.29), the impact coefficient was obtained and shown in Figure 3.6(a). The coefficient is fitted with a two-term power series model:

$$C_i(n) = -0.384n^{0.097} + 0.880 \tag{3.32}$$

The average impact force can be calculated after obtaining the impact coefficient by using Equation (3.28). Figure 3.6(b) plots the average impact force magnitude against the droplet number.

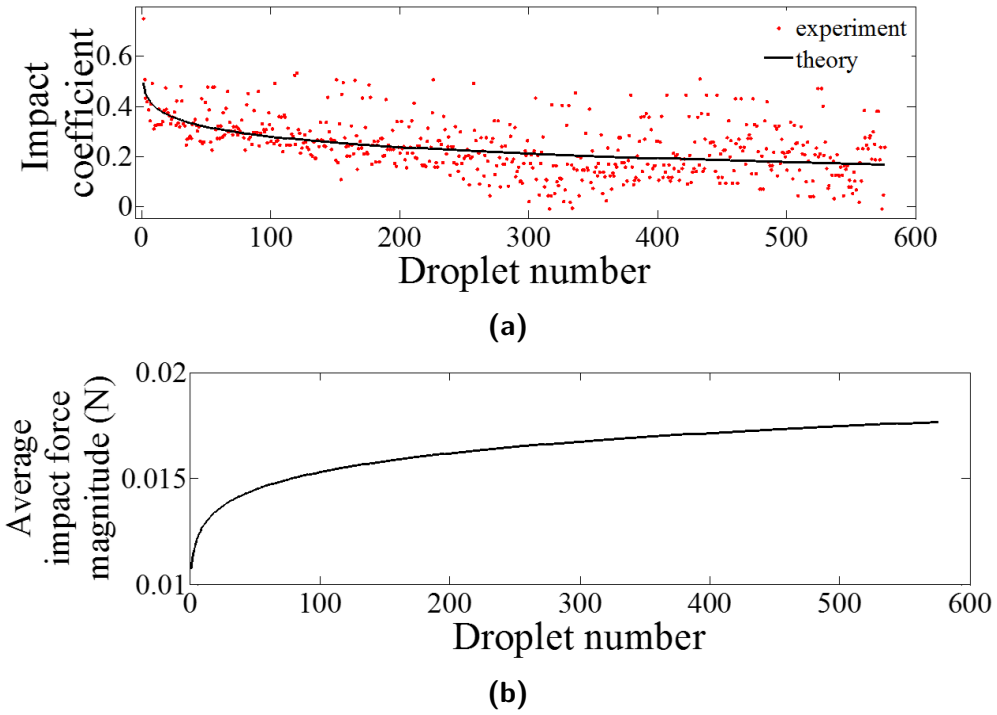


Figure 3.6: (a) Impact coefficient and (b) magnitude of the average impact force against droplet number.

From the experimental data in Figure 3.6(a), the impact coefficient decreased rapidly at $n < 40$. This is due to the sudden spreading or splashing of the water droplet after the impact on the surface of the piezoelectric beam. As the water layer accumulates, the impact surface became softer and the recoil motion is slower in comparison to a harder impact surface [44]. As a result, the impact coefficient was observed to decrease at a slower rate at $n > 40$. The relationship of the impact coefficient and average impact force magnitude is inversely proportional by comparing both graphs in Figure 3.6. This is due to the

average impact force equation shown in Equation (3.28).

According to Figure 3.6(a), the impact coefficient from the experimental data started to spread when $n > 200$. As the volume of the water layer accumulated grows, the momentum of the impinging water droplet will not be directly transferred to the beam or dissipated as loss of momentum as described by the impact coefficient in Equation (3.28). Part of the impact momentum will be converted to water ripple motion, as water ripple was found to be more noticeable as the water layer volume increases. Such loss in momentum is hard to be quantified. Nonetheless, the fitted curve using the two-term power series model is able to describe the trend of the impact coefficient well.

The impact coefficient can be correlated to the added mass coefficient by using a curve fitted impact coefficient against the empirical added mass coefficient graph depicted in Figure 3.7. The fitted curve exhibits a good correlation between the two parameters. The numerical sample points were fitted by using a two term exponential model using MATLAB:

$$C_i(n) = 0.1923e^{-21.94C_a(n)} + 0.2773e^{-0.4458C_a(n)} \tag{3.33}$$

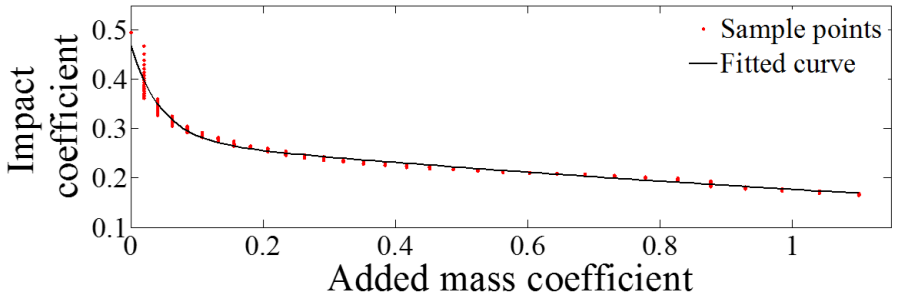


Figure 3.7: Impact coefficient against added mass coefficient.

3.4.3 Results and discussion

The MATLAB code for a single droplet impact when there is no water layer is given in Appendix B. To demonstrate the process of water droplet accumulation, camera images of the static water layer accumulated on the surface of the piezoelectric beam are inspected in 3.8. The theoretical results for both time and frequency spectrum were found to be underestimating voltage magnitudes when comparing with the experimental results. The reason for this underestimation was due to the damping ratio, shown in Figure 3.3, where the theoretical damping ratio underestimated the oscillations of the damping ratio obtained from experiment when $n < 274$. At $n = 274$, the water layer formed on the surface has reached the maximum width of both sides of the piezoelectric beam. Further increase in droplet number would expand the water layer in the length direction of the piezoelectric beam. The water layer reached the clamp end and the tip of the piezoelectric beam when $n = 361$. Subsequently, the water layer slowly filled up the rest of the piezoelectric beam surface and started to spill after reaching its optimum volume at $n = 576$.

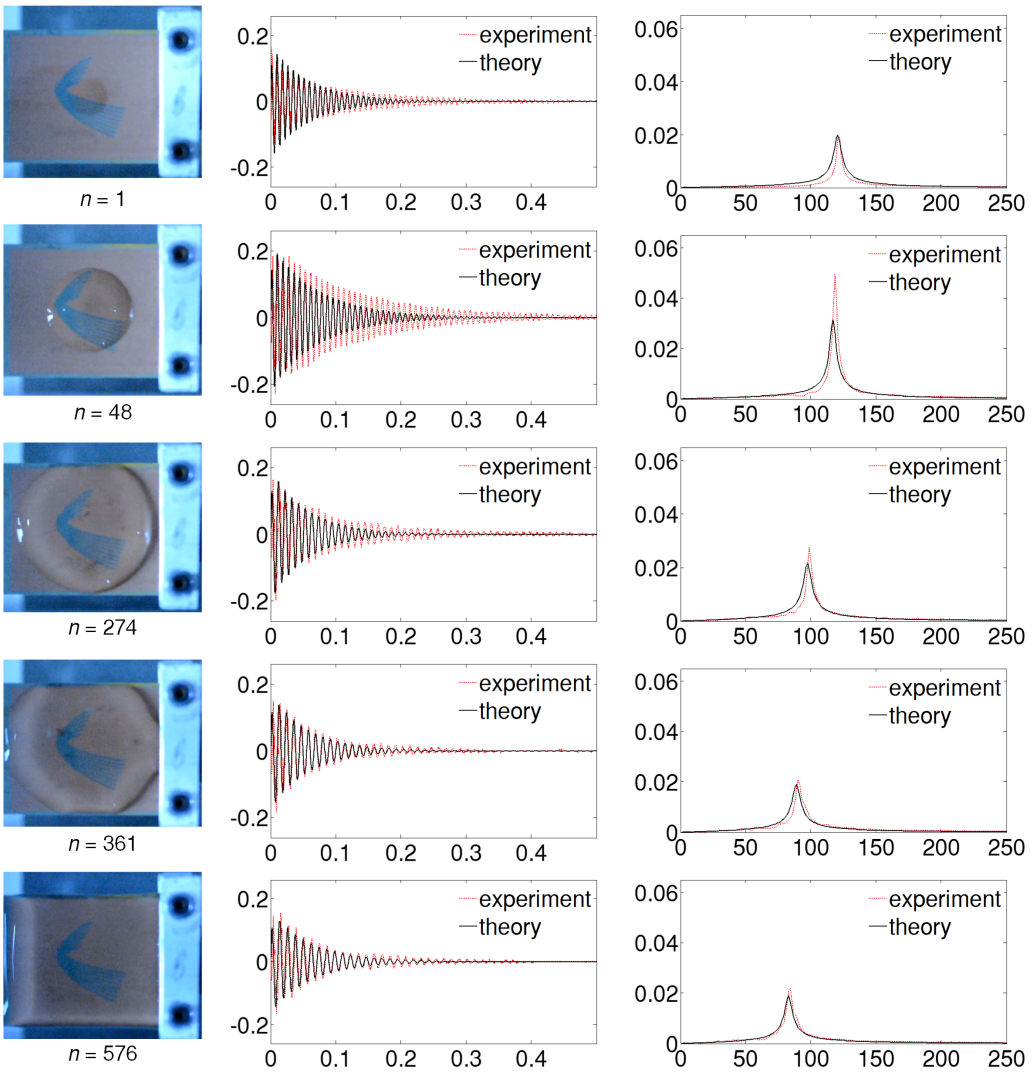


Figure 3.8: Camera images of static water layer at different droplet numbers ($n = 1$, 48, 276, 361, and 576); the corresponding voltage time response graphs (y-axis: voltage, V; x-axis: time, s); and the corresponding frequency response graphs (y-axis: voltage, V; x-axis: frequency, Hz).

By comparing the theoretical results for the case of water layer at its optimum volume (when $n = 576$) and without water layer ($n = 1$), the peak voltage recorded was 147.1 mV and 146.3 mV respectively. The generated peak voltage was increased by 0.8 mV when the volume of the water layer formed on the surface of the beam is at optimum volume. This can be explained by the lower

impact coefficient at $n = 576$ when compared to $n = 1$, which gives a higher average impact force magnitude according to Figure 3.6.

To obtain a quantitative comparison between the voltage generated by the piezoelectric beam at $n = 1$ and $n = 576$, the root mean square (RMS) voltage is calculated:

$$V_{rms} = \sqrt{\frac{1}{\underline{T}} \int_0^{\underline{T}} V^2(t) dt} \tag{3.34}$$

where, $\underline{T}$ is the time period of the voltage response.

The theoretical RMS voltages at $n = 1$ and $n = 576$ were estimated to be 28.46 mV and 26.95 mV respectively. The RMS voltage when the water layer is at its optimum volume was found to be lower than the instance where there is no water layer. Although the theoretical peak voltage is higher at $n = 576$, the increase in damping ratio (illustrated in Figure 3.3) reduces the performance of the harvester as the voltage oscillation reaches steady state at a faster pace.

The comparison of the experimental and theoretical frequency response graphs when $n = 1$ and $n = 576$ are plotted in Figure 3.9. The experimental result showed that the first mode natural frequency decreased from 122.1 Hz to 84.23 Hz where the theoretical value decreased from 120.8 Hz to 83.1 Hz. Both experimental and theoretical results showed a reduction in first mode natural frequency when the water layer was at its optimum volume. The shift in the first mode natural frequency is due to the increase in the overall modal mass due to the introduction of the water layer. This is reflected in Equation (3.2),

where the square of the first mode natural frequency is inversely proportional to the overall modal mass of the system.

On another note, a series of peaks in the lower frequency region were observed in the experimental frequency response graph with water layer in Figure 3.9a. Interestingly the series of peaks were not present in the experimental frequency response graph without water layer in Figure 3.9a. These peaks may be attributed to the water ripple motion [68]. Since the voltage contribution of the water ripple is relatively low, it is not included in the theoretical studies.

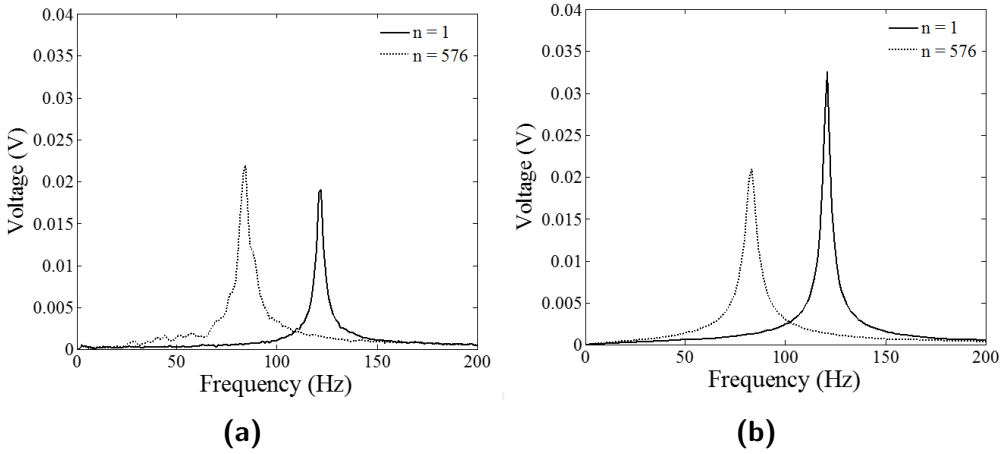


Figure 3.9: Comparison on the (a) experimental and (b) theoretical frequency response graphs with (n = 576) and without (n = 1) the presence of water layer.

To evaluate the performance of the energy harvester over the course of water layer accumulation, peak voltage and RMS voltage of the respective droplet impact were considered. The peak voltage graph provided in Figure 3.10 was obtained by extracting the instantaneous maximum voltage value and plotted with its respective droplet number. The RMS voltage plotted in Figure 3.11 was

obtained by estimating the RMS voltage of each droplet number using Equation (3.34), where the maximum time period for each voltage response is $\underline{T} = 0.5$ s.

The experimental results of both peak voltage and RMS voltage showed similar trend. This is the result of the oscillatory trend found in the damping ratio (Figure 3.3), where the data oscillates as the droplet number increases. In general, the agreement between the theoretical and experimental results for both peak and RMS voltage is good.

The peak and RMS voltage were found to increase initially at $n < 48$ for the experimental results and at $n < 41$ for the theoretical results. This is due to the loss in momentum as described by the impact coefficient, shown in Figure 3.6a. The decrease in impact coefficient will increase the average impact force magnitude of the impinging water droplet. As the average impact force magnitude increases, the peak and RMS voltage will increase as well.

According to Figure 3.10 and Figure 3.11, the peak and RMS voltage started to decrease shortly after they had reached their respective peak values. The decrease in peak and RMS voltage were due to the increase of the overall system modal mass and modal damping. As the modal damping increases, the system will experience higher resistive force. This can be observed from the voltage time response graphs in Figure 3.8 , where the voltage was damped quicker with a higher damping ratio (Figure 3.3).

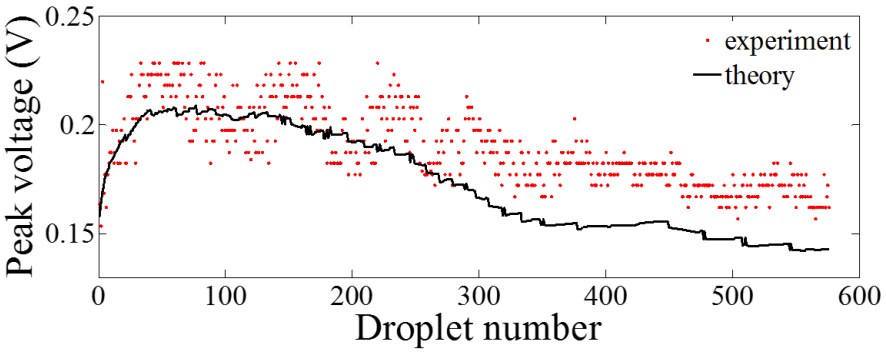


Figure 3.10: The comparison of experimental and theoretical peak voltage with fitted damping.

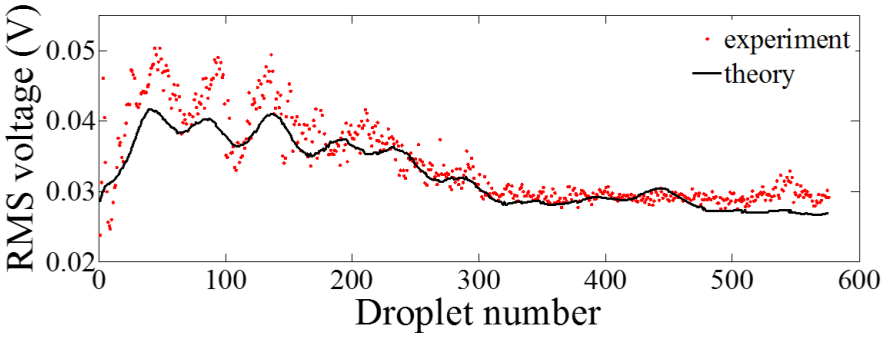


Figure 3.11: The comparison of experimental and theoretical RMS voltage.

The average percentage error between the experimental and theoretical results for the peak and RMS voltage were 11.48 % and 6.94 % respectively. The RMS voltage is directly affected by the damping ratio as some discrepancies were observed between the fitted and actual damping ratio, shown in Figure 3.3. Nevertheless, the theoretical peak and RMS voltages are able to predict the trend of the experimental results.

The highest recorded peak voltage from the experimental and theoretical results were 0.23 V and 0.21 V respectively. The instantaneous peak power can be estimated by using, $P = V^2/R$. Therefore, the instantaneous peak power from the experimental and theoretical results were calculated to be 3.53 μW and

2.94 μW respectively. The highest recorded RMS voltage from the experimental and theoretical results were 0.05 V and 0.04 V respectively. The mean value for the RMS voltage from the experimental and theoretical results were estimated to be 0.034 V and 0.032 V respectively.

The RMS voltage can be plotted against added mass coefficient, given in Figure 3.12. By using the mean value of the RMS voltage, an optimal operating region can be obtained. The optimal operating region is where the experimental or theoretical RMS voltage has a higher value than the respective mean RMS voltage. From Figure 3.12, the experimental and theoretical optimal operating regions were found to be at $0.03423 < C_a < 0.4396$ interval and at $0.03223 < C_a < 0.4698$ interval respectively. By checking the camera images in Figure 3.8, the optimal operating region happens before the accumulated water layer reaches the width ends of the piezoelectric beam. When the energy harvester is operating at this region, more energy will be harvested. Therefore, it is interesting to look into surface treatment for the piezoelectric beam in order for it to operate at this region all the time.

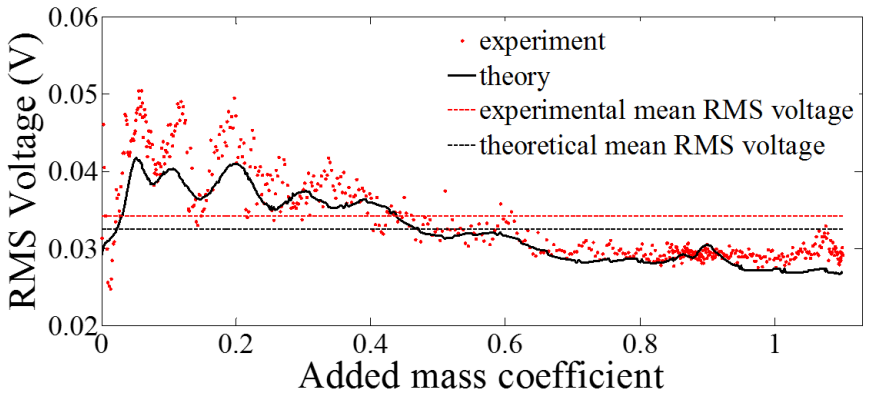


Figure 3.12: RMS voltage against added mass coefficient

3.5 Dynamics of the harvester subjected to multiple droplets impact

In an actual rain, raindrop will impact on different positions on the piezoelectric beam at various rain rates. To investigate these phenomena in a controlled environment, a multiple droplet impact model is developed. The multiple droplet impact model considers the drop period and drop position on the piezoelectric beam. The drop period of the rain and three drop positions are considered and they are maintained as a constant to simplify the validation of the model.

Rain is stochastic in nature, it is generally distinguished by the drop size distribution (DSD) and rain rate of the rain [41]. Rain rate is the quantity of number of raindrops accumulated per unit time on unit area while DSD describes the amount of raindrop counts on different raindrop diameter classes. In this section, the droplet size is set as a constant and three rain types are considered to simulate varying rain rate. The three rain types are: light stratiform rain (LSR), moderate stratiform rain (MSR), and heavy thundershower (HT). The three rain types are categorised according to their rain rate as shown in Table 3.1 [38].

According to Perera et al. [38], the three rain types are categorised using raindrop density (N_T). Drop period (T_d) is introduced to produce a statistically valid measurement of rain rate. Drop period is defined as:

$$T_n = (aN_T)^{-1} \tag{3.35}$$

Table 3.1: Raindrop density and drop period for different rain type.

Rain type	Raindrop density ($\mathbf{s^{-1}m^{-2}}$)	Drop period (s)
Light Stratiform Rain	280	2.0
Moderate Stratiform Rain	495	1.1
Heavy Thundershower	818	0.7

where, a is the device area ($a = 0.001766$ m^2).

The pulse function shown in Equation (3.17) describes the event of single water droplet impact. In the formulation of a multiple droplet excitation model, a continuous periodic signal that consists of drop period (T_n) and impact duration (τ) are used. It is modelled by using Heaviside Function as:

$$\eta_m(t) = \sum_{n=1}^{N_d} \{[\Phi(t-(n-1)T_n)] - [\Phi(t-\tau-(n-1)T_n)]\} \tag{3.36}$$

where, N_d is the total number of water droplets; Φ is the Heaviside function.

In the multiple droplet impact, the water droplet will impact on different positions along the beam. To incorporate the effect of multiple droplet impact, the modal force in Equation (3.16) is rewritten as:

$$F_m(t) = f_{avg}\eta_m(t) \sum_{n=1}^{N_d} [\varphi(x_n)] \tag{3.37}$$

$$x_n = \begin{cases} x1, & \text{when: } n = 1, 4, 7, ... \\ x2, & \text{when: } n = 2, 5, 8, ... \\ x3, & \text{when: } n = 3, 6, 9, ... \end{cases} \tag{3.38}$$

where, n is the droplet number count; $x1$, $x2$, and $x3$ are three fixed position on the piezoelectric beam shown in Figure 3.13.

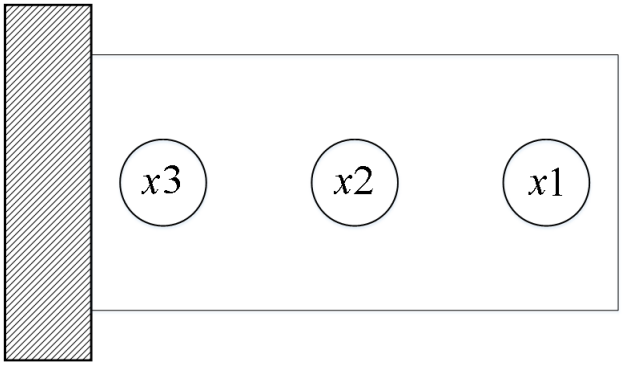


Figure 3.13: Impact position on the piezoelectric beam, where $x1 = 42$ mm, $x2 = 27$ mm, $x3 = 12$ mm, which are measured from the clamp.

3.6 Experiment validation of the multiple droplet impact model

The purpose for this section is to study the response of the piezoelectric beam when being excited by water droplet impacting on three different positions on the piezoelectric beam. The theoretical model describing multiple droplet impact derived in Section 3.5 is validated in this section using experimental studies. Three different rain types, namely light stratiform rain (LSR), moderate stratiform rain (MSR), and heavy thundershower (HT), which produce different rain rates are

studied. The rain types were classified based on the number of raindrops per unit time on unit area provided in Table 3.1 [38].

Single water droplet impact experiments had been conducted many times in the literature [34, 37, 40]. The water droplet in the mentioned studies was produced by using a syringe pump. With a syringe pump, the drop formation time is slow in order to produce an accurate drop size. According to Guigon et al. [34], the drop formation time ranges from 10 s to 60 s. From Table 3.1, the highest drop period in this study is 0.7 s, which formation time is faster than the minimum formation time when using a syringe pump. Although the peristaltic pump in the previous section is able to generate steady stream of water droplet at a fast rate, it is unable to synchronise three syringes. In order to synchronise three syringes, three peristaltic pumps are needed, and this becomes infeasible. Therefore, a new water droplet generator is needed and will be presented in this section.

In this section, the impact coefficient obtained from Section 3.4.2 is utilised to estimate the average impact force of the impinging water droplets. The added mass coefficient due to water droplet accumulation was determined. In addition, a drop position study is conducted to investigate the dynamic response of the harvester. Three different rain types are studied by varying the rain rate. The performance of the energy harvester under the three different rain types are evaluated by using the RMS voltage and energy accumulated over a time period of 12 s.

3.6.1 Experiment methodology

The water droplet is produced by three individual solenoid valves connected to three syringes. The syringes are able to generate droplet diameter of 4.36 mm. The syringes are elevated 1.23 m above the impact plane. The syringes were carefully positioned so that it could impact on the positions illustrated in Figure 3.13. An overview and schematic diagram of the experiment setup are depicted in Figure 3.14.

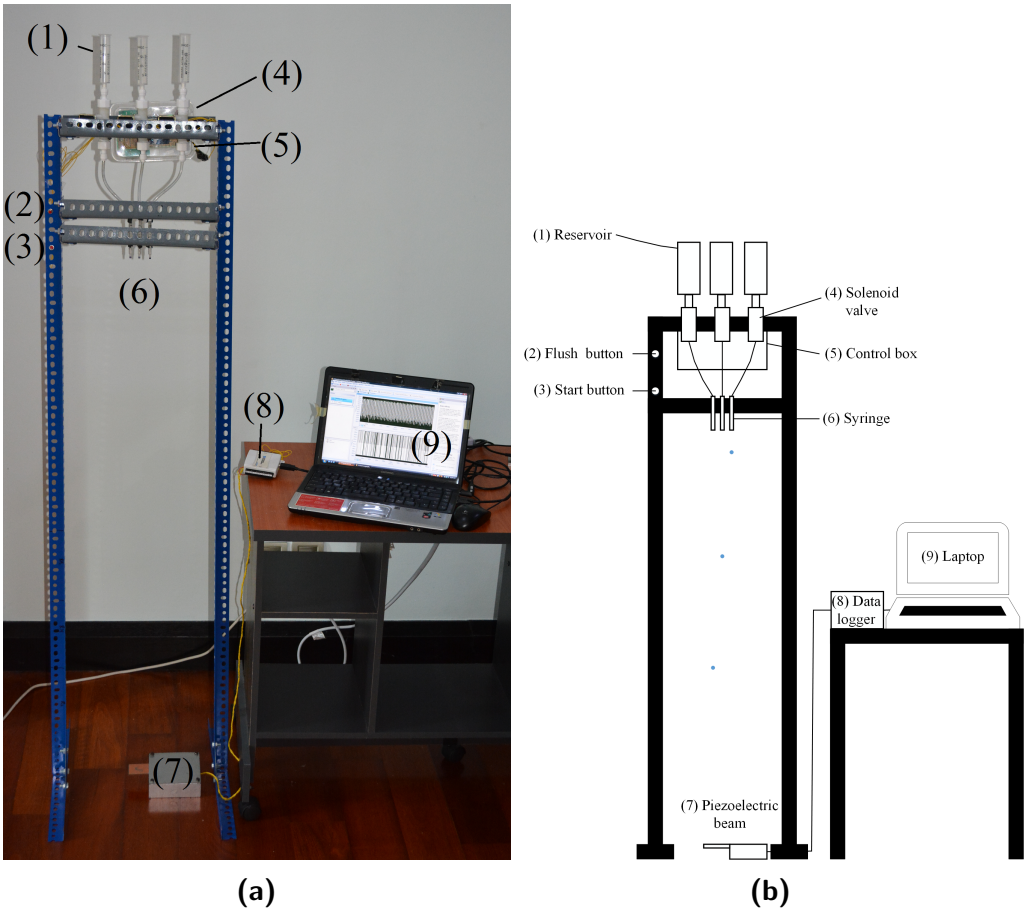


Figure 3.14: (a) Overview and (b) schematics diagram of the experimental setup for multiple droplet excitation.

Three syringes are mounted on top of the solenoid valves that act as water

reservoirs. The drop period of the water droplet is controlled by the on and off of the solenoid valves. The toggling of the solenoid valves is synchronised by a microcontroller (Microchip-PIC18F4550), which is housed inside a control box. A flush and start buttons are connected to the microcontroller. This is to facilitate flushing and initiation of the programmed rain type routine. The flushing function is vital to ensure that air bubble does not trapped within the system. The piezoelectric beam (Mide-v25w) is clamped by using a water resistant casing to ensure that water does not short the output pins. The piezoelectric layers are connected in series with a load resistance of 15 kΩ. The generated voltage is measured by using a data logger (NI-USB6008) and the data is stored in a laptop.

3.6.2 Results and discussion

The multiple droplet impact model developed in Section 3.5 is validated through experimental results in this section. The theoretical results are simulated using MATLAB. In this section, the performance of the raindrop impact energy harvester due to three different impact positions and three different rain rates are studied. The piezoelectric layers are connected in series and the generated voltage is measured across a load resistor with resistance of 15 kΩ.

Added mass coefficient

When water droplet impacts the surface of the piezoelectric beam, the post impact behaviour of the impinging water droplet will affect the average impact force. This phenomenon is highlighted in Section 3.3, by describing the post impact behaviour using the impact coefficient. In the case of multiple droplet impact, the water will spill on the sensing surface of the laser vibrometer, hence tip displacement could not be obtained.

In order to obtain the impact coefficient, the added mass coefficient from the experimental result is estimated using Equation (3.13). Two parameters are needed in order to obtain the added mass coefficient, which are the damped natural frequency and damping ratio. The damped natural frequency was obtained by performing FFT on the voltage time response graph of individual water droplets while the damping ratio is obtained by using logarithmic decrement, Equation (2.31). After obtaining the added mass coefficient, the impact coefficient could be calculated using Equation (3.33). The voltage time response graph and the added mass coefficient graph for LSR, MSR and HT are presented in Figure 3.15.

By inspecting Figure 3.15, there were only two added mass coefficient values, which were 0 and 0.0421. By substituting these values into Equation (3.33), the impact coefficients were found to be 0.496 and 0.361 respectively. The impact coefficient values were substituted to Equation (3.28) in order to obtain the average impact force. The obtained average impact force is then substituted to the theoretical equation of motion for multiple droplet excitation given in Equation (3.37).

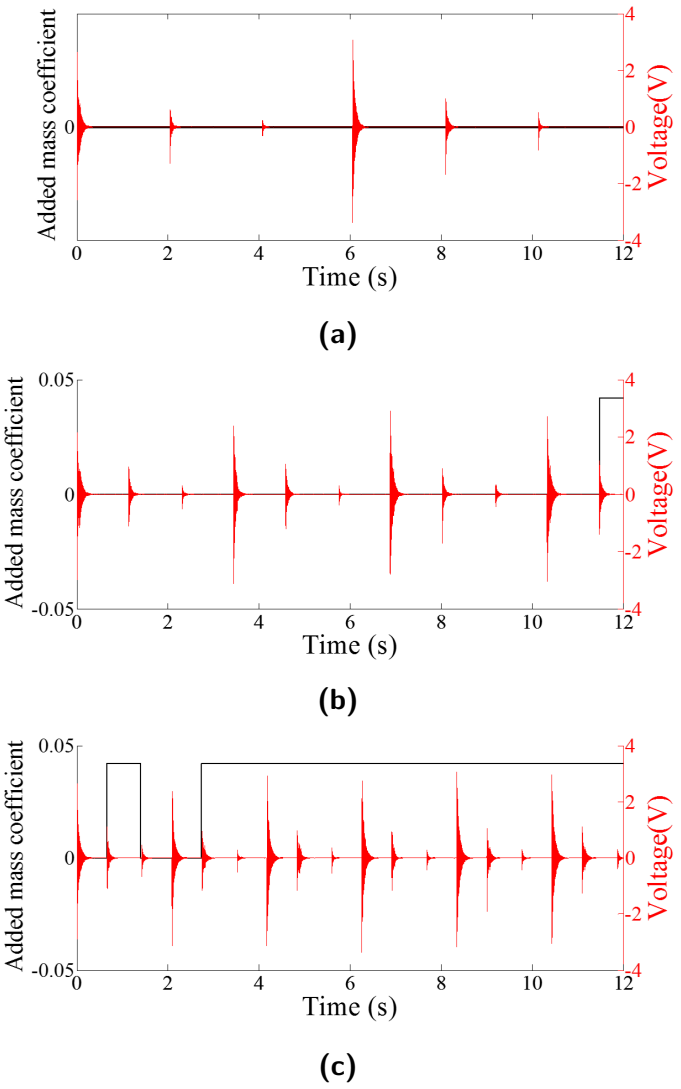


Figure 3.15: Voltage time response (black) and added mass coefficient (red) graphs for: (a) LSR; (b) MSR; and (c) HT.

Drop position study

The response of water droplet impact on three different positions on the piezoelectric beam is validated as well. The impact location is depicted in Figure 3.13. The experimental results presented in this section utilised the first three drops from the simulated rain type, LSR. The rain type LSR was considered here due to the impact coefficient remains constant throughout the experiment.

This is to ensure a fair comparison as the only varying parameter is the drop position. The experimental and theoretical results of the three different impact positions are shown in Figure 3.16. The results shows a good conformance.

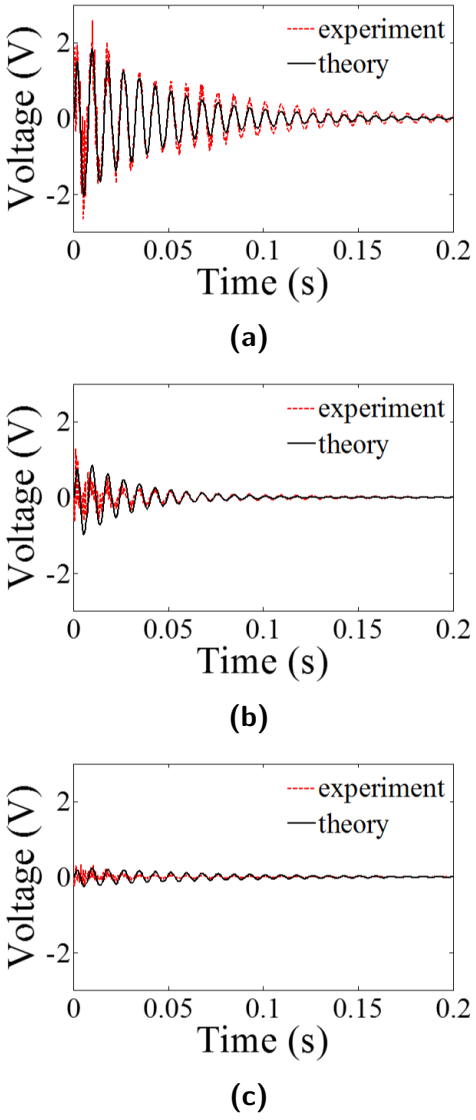


Figure 3.16: Experimental and theoretical voltage time response graphs of water droplet impinging on position: (a) $x1$; (b) $x2$; and (c) $x3$.

The effect of drop position is evaluated by comparing the peak voltage and RMS voltage generated from the three drop positions. The experimental and

theoretical peak voltage and RMS voltage are tabulated in Table 3.2 and Table 3.3 respectively.

Based on the results in Table 3.2 and Table 3.3, the maximum percentage error for the peak voltage and RMS voltage were 36.04 % and 30.89 %. From the peak voltage results (Table 3.2), the theoretical results were found to be consistently underestimating the experimental results by an average percentage error of 28.56 %. The reason for this is that the impact coefficients used here are approximated values obtained from different experimental setup . Nevertheless, the impact coefficients were able to describe the post impact behaviour of the impinging water droplet well. The percentage errors for the RMS voltages for the position $x2$ and $x3$ were higher than position $x1$. This was due to the slight underestimation of the damping ratios as the voltage magnitudes were lower when compared to drop position $x1$. The effect of underestimation of the damping ratios can be observed from Figure 3.16(b) and (c), where the theoretical voltage reaches steady state slower than the experimental voltage.

The experimental and theoretical results in Table 3.2 and Table 3.3 suggest that when the water droplet impacts the harvester further from the clamp, more voltage will be generated. This is because higher moment will be generated when the water droplet impacts further from the clamp end of the piezoelectric beam. Therefore, the piezoelectric layers will experience more strain and more electrical charges will be produced.

Table 3.2: Experimental and theoretical results, and the percentage error for the peak voltage when water droplet impacts at position $x1$, $x2$ and $x3$ of the piezoelectric beam.

Drop position	**Experiment (V)**	**Theory (V)**	**Percentage Error (%)**
$x1$	2.65	2.05	29.12
$x2$	1.29	0.98	30.89
$x3$	0.32	0.25	25.69

Table 3.3: Experimental and theoretical results, and the percentage error for the RMS voltage when water droplet impacts at position $x1$, $x2$ and $x3$ of the piezoelectric beam.

Drop position	**Experiment (V)**	**Theory (V)**	**Percentage Error (%)**
$x1$	0.58	0.52	12.39
$x2$	0.14	0.21	30.60
$x3$	0.05	0.07	36.04

Rain rate study

The effect of the three simulated rain rates (LSR, MSR, and HT) on the energy harvester is investigated too. The results were benchmarked by using RMS voltage and total energy accumulated over a time period of 12 s. The experimental and theoretical voltage time response graphs for the three different simulated rain rates (LSR, MSR, HT) are presented in Figure 3.17. The RMS voltage and the total energy accumulated over time, t, can be obtained by using Equation (3.34) and (3.39) respectively.

$$E(t) = \int_0^t \frac{V^2(t)}{R} dt \tag{3.39}$$

The experimental RMS voltage obtained from LSR, MSR, and HT were 0.12

V, 0.17 V, and 0.22 V respectively whereas the theoretical RMS voltage value estimated were 0.10 V, 0.13 V, and 0.19 V respectively. The percentage errors of the experimental and theoretical results were calculated to be 23.50 %, 24.33 %, and 14.24 % for the rain type LSR, MSR, and HT respectively. Judging from the percentage errors, the experimental and theoretical results correlate well with each other.

The total energy accumulated over a period of 12 s for LSR was found to be 12.18 μJ and 8.00 μJ from the experimental and theoretical results respectively. As for MSR, the experimental and theoretical total energy accumulated were 22.44 μJ and 14.65 μJ respectively. The total energy accumulated from the experimental and theoretical results for rain type HT were 37.79 μJ and 30.47 μJ respectively. By comparing the experimental results to the theoretical results for the total energy accumulation, it was found that the theoretical results were consistently underestimating the total energy accumulated. This is expected as impact coefficients and damping ratios used in the theoretical simulations were approximate values. By inspecting Figure 3.17, one can observe that some peak voltages found in the experimental results were having higher voltage magnitude compared to the theoretical results. Nevertheless, the theoretical results were able to capture the trend of the experimental results.

According to the RMS voltage and total energy accumulated in the experimental and theoretical results, as the rain rate increases, the RMS voltage and total energy accumulated increases as well. This shows that the RMS voltage and total energy accumulated are having a positive trend to the rain rate.

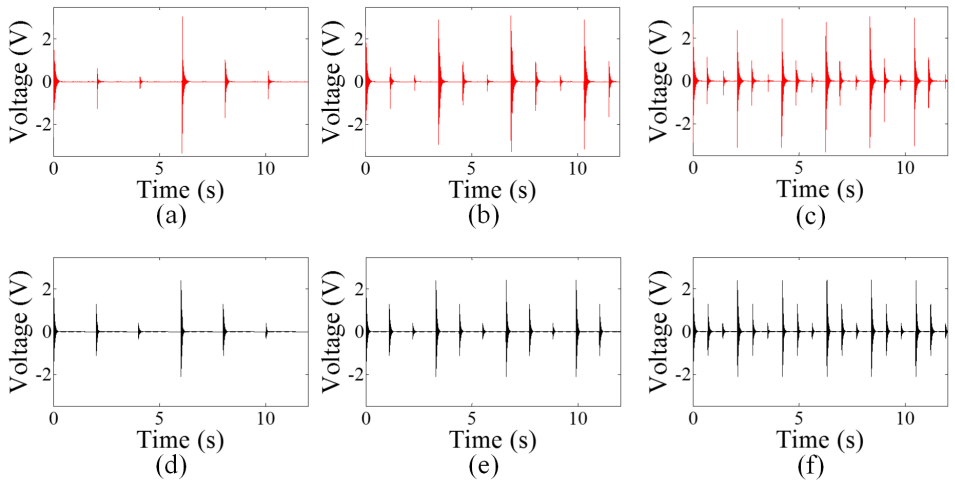


Figure 3.17: Voltage time response graphs (y-axis: voltage,V; x-axis: time, s) for experimental results: (a) LSR; (b) MSR; (c) HT and theoretical results: (d) LSR; (e) MSR; (f) HT.

3.7 Chapter conclusion

In this chapter, the single and multiple droplet impact models have been developed and validated through experiments.The forming of a water layer on the surface of the piezoelectric beam is due to the accumulation of successive water droplet impacts. Added mass coefficient is used to describe the modal mass of the water layer. The loss of momentum of a water droplet impact due to the post impact behaviours is modelled using an impact coefficient. The impact coefficient is determined by using added mass coefficient, and tip displacement from the experiment. This impact coefficient is fitted by using a two-term power series model. The experimental and the predicted theoretical results showed good agreement. Peak and RMS voltage are considered in the attempt to evaluate the performance of the energy harvester over the course of water layer accumulation. Peak voltage analysis revealed that the highest recorded peak voltage from the

experimental and theoretical results were 0.23 V and 0.21 V respectively, which yielded instantaneous power of 3.53 μW and 2.94 μW respectively. The highest recorded RMS voltage from experimental and theoretical results were found to be 0.05 V and 0.04 V respectively. In addition, an optimal operating region is deduced by using the mean RMS voltage from the experimental and theoretical results. This could be correlated to the camera images in Figure 3.8, where the optimal operating region happens before the water layer reaches the width ends of the piezoelectric beam. Therefore, the development of surface treatment for the piezoelectric beam can be a good future prospect of this research.

In Section 3.5, multiple droplet impact model is presented. The model considers different drop periods and drop positions on the piezoelectric beam. Three rain types (LSR, MSR, and HT) that correspond to different drop periods were considered. In order to validate the mathematical model, an experimental setup consists of three individual syringes were developed. In general, the experimental and theoretical results are in good conformance. Added mass coefficient and impact coefficient for each droplet impact are obtained experimentally. Drop position study revealed that when the water droplet impacts further form the clamp, more RMS voltage will be produced, this will give rise to higher energy production. According the rain rate study, higher rain rate will reduce the drop period, which ends up with more droplet impacts. The three rain types were benchmarked by using a fixed experiment period of 12 s. The total energy accumulated over the 12 s period for the experimental and theoretical results were 37.79 μJ and 30.47 μJ respectively. In this study, great potential can be observed

when the water droplet is impinging at the tip of the piezoelectric beam with a low drop period. This could be realised by designing a rain water collecting regime and funnelling the rain water at the tip of the piezoelectric beam.

Chapter 4

Performance of the energy harvester in a simulated rain environment

4.1 Introduction

After establishing the fundamentals on the dynamics of single and multiple droplet impacts, this research is able to progress into simulated rain environment. Based on the literature studies on rain energy harvester, most of the conducted experimental works were based on fixed water droplet diameter dripping at a fixed height [32, 34, 37]. The stochastic nature of actual rain makes it hard to be modelled. Nevertheless, rain can be characterised by rain rate

and drop size distribution (DSD) [41]. Rain rate measures the total amount of precipitation in a fixed time frame, while DSD describes the amount of raindrop count for different raindrop diameter classes. This provides a foundation to study the rain behaviour in a controlled laboratory environment. In this chapter, the performance of the piezoelectric rain energy harvester is investigated through a rain simulator. Artificial raindrops (characterised by the rain rate and DSD) were generated and impacted on a piezoelectric beam. A dynamical model that incorporates the excitation force from the artificial raindrops is proposed.

In Chapter 3, three different drop rates were investigated. The study was carried out by using water droplets with fixed diameter, impinging on three fixed drop positions on the piezoelectric beam surface. The idea of multiple droplet excitation is extended in this chapter, where water droplets of random size will be impinging on random position on the piezoelectric beam. As the water layer accumulates on the surface of the piezoelectric beam, the added mass coefficient and impact coefficient, discussed in Chapter 3, will affect the performance of the piezoelectric energy harvester. Hence, they are included in the model.

The piezoelectric energy harvester was tested under laboratory conditions before being deployed under actual rain (discussed in Chapter 5). A rain simulator was developed using different nozzles to simulate four artificial rains with different rain rates and DSDs. The dynamical model presented in previous chapters is extended to include the excitation force generated by the artificial rain. In this study, the duration of experiments was fixed at 300 s, and the rain rate of each artificial rain was maintained constant throughout the experiment duration.

The stochastic nature of the artificial rain excitation model is described using two random parameters, which are DSD and impact position on the beam. The DSD is described by using a lognormal distribution, while the impact position on the beam is represented using a uniform distribution. A section is dedicated to the numerical simulation of the artificial rain excitation model. The theoretical model is verified through experimental studies. The performance of the piezoelectric energy harvester is evaluated by using the total energy accumulated over a fixed time interval of 300 s.

4.2 Artificial rain excitation model

The mathematical model for a piezoelectric beam is discussed in Chapter 2. The piezoelectric beam is modelled as a distributed parameter system. In Chapter 3, added mass effect is integrated into the piezoelectric beam model to describe the water layer accumulation on the beam. The mechanical and electrical domain of the piezoelectric beam model is presented in Equation (3.12) and Equation (2.35) respectively, recalled as:

$$(1 + C_a)\underline{M}\ddot{r}(t) + \underline{D}_a\dot{r}(t) + \underline{K}r(t) - \theta V(t) = F(t)$$

$$\theta^t r(t) + C_p V(t) = q(t)$$

The piezoelectric beam model is validated through base excitation experiment using an electromagnetic shaker described in Chapter 2. In Section 3.5, the single

droplet impact external model force is extended into multiple droplet impact as presented in Equation (3.37):

$$F_m(t) = f_{avg}\eta_m(t)\sum_{n=1}^{N_d}[\varphi(x_n)]$$

In this section, the piezoelectric beam is placed under an artificial rain. Raindrops with different diameter will impact different positions on the piezoelectric beam. In order to incorporate random drop size and drop position, the multiple droplets impact excitation model has to be extended. For the generalised excitation force due to the artificial raindrop impact, two random variables are introduced, which are the raindrop diameter (D_n) and the impact position on the beam (x_n).

According to the experimental results recorded by the laser precipitation monitor sensor, the diameter of the water droplets produced by the rain simulator was found to be lognormal distributed. To obtain the nth droplet diameter, a random number generator based on two lognormal parameters, μ and σ is implemented as:

$$D_n \sim \mathscr{L}(\mu, \sigma) \tag{4.1}$$

where, $\mathscr{L}$ is a lognormal distributed random number generating function with the two lognormal parameters, μ and σ. Here, μ and σ are the log-mean and log-standard-deviation of the lognormal distribution.

Meanwhile, the drop position is assumed to be uniformly distributed along the length direction of the beam, giving the following expression:

$$x_n \sim \mathscr{U}(0, L) \tag{4.2}$$

where, $\mathscr{U}$ is a uniform distributed random number generating function ranges from 0 to the maximum length span of the piezoelectric beam, L.

The average impact force was given in Equation (3.28), which only considered fixed water droplet size. Parameters such as mass (m_w), impact velocity (v_w), and impact duration (τ) of the impinging water droplet are dependent on the droplet diameter. For the case of artificial rain, the droplet diameter varies. Therefore, Equation (3.28) is re-expressed in the function of the nth random water droplet diameter as:

$$f_{avg}(D_n) = \frac{[1 - C_i(n)]m_w(D_n)v_w(D_n)}{\tau(D_n)} \tag{4.3}$$

$$\tau(D_n) = \frac{D_n}{v_w(D_n)} \tag{4.4}$$

By relating Equation (4.1-4.4) into the generalised excitation force due to multiple droplet, given in Equation (3.37), the generalised excitation force due to artificial rain is written as:

$$F_a(t) = \sum_{n=1}^{a_r N_T} [f_{avg}(D_n)\varphi(x_n)\eta_a(t)]$$

$$\eta_a(t) = \Phi[t - (n-1)T_n] - \Phi[t - \tau(D_n) - (n-1)T_n] \tag{4.5}$$

where, N_T is the total number of water droplets; $f_{avg}(D_n)$ is the average impact force due to n^{th} droplet diameter (D_n); φ is the normalised mode shape function; x_n is the impact position of the nth droplet; Φ is the Heaviside function; $\tau(D_n)$ is the impact duration of the nth droplet; T_n is the drop period; $\eta_a(t)$ is the pulse function for the artificial rain.

Since the rain rate for the whole experiment duration is fixed, the total number of water droplet can be obtained from the laser precipitation monitor sensor (N_T). The total number of water droplets were measured across a measuring area of 4513.4 mm^2. In order to obtain the total number of water droplets that impact the piezoelectric beam, a scaling factor is needed. The scaling factor is obtained by dividing the surface area of the piezoelectric beam (1766 mm^2) by the measuring area of the laser precipitation monitor sensor (4513.4 mm^2). The drop period can be estimated using:

$$T_n = \frac{t_T}{a_r N_T} \tag{4.6}$$

where, t_T is the total duration of the experiment ($t_T = 300$ s); N_T is the total number of water droplets measured by the laser precipitation monitor sensor; a_r is the scaling factor ($a_r = 0.3913$).

4.3 Experiment methodology

A rain simulator is designed to produce artificial rain that mimics actual rain characteristics such as rain rate and DSD. Rain simulator is useful for many research purposes, such as to investigate the effects of rainfall on soil properties, and soil erosion during rainstorms [69]. In general, there are two types of rain simulator, namely drip type and spray type simulator [70]. A drip type rain simulator design includes a water reservoir with a constant water head placed on top of the simulator, allowing the water to form slowly and drip out from an array of capillary tubes [71]. Such design is capable of simulating free falling raindrops accurately but it requires a substantial height for the raindrops to reach terminal velocity. The design of a spray type rain simulator involves pressurised water and a spray nozzle. Such design enables the simulator to produce raindrops near to terminal velocity without compromising the height of the simulator. In this study, a spray type rain simulator is considered due to height constraint of the research facility. The overview of the experimental setup is presented in Figure 4.1.

The rain simulator consists of two nozzles, QPHA-10, and QPHA-6.5. The two nozzles are raised approximately 2.5 m above the impact plane, which is the surface of the piezoelectric beam. The two nozzles can be directly operated using the water pressure from the commercial pipeline, therefore no water pump is installed in this setup. A valve is installed to control the flow of water of the main pipe. The control box comprises two mechanical switches and power supply for the solenoid valves. The mechanical switches in the control box enable

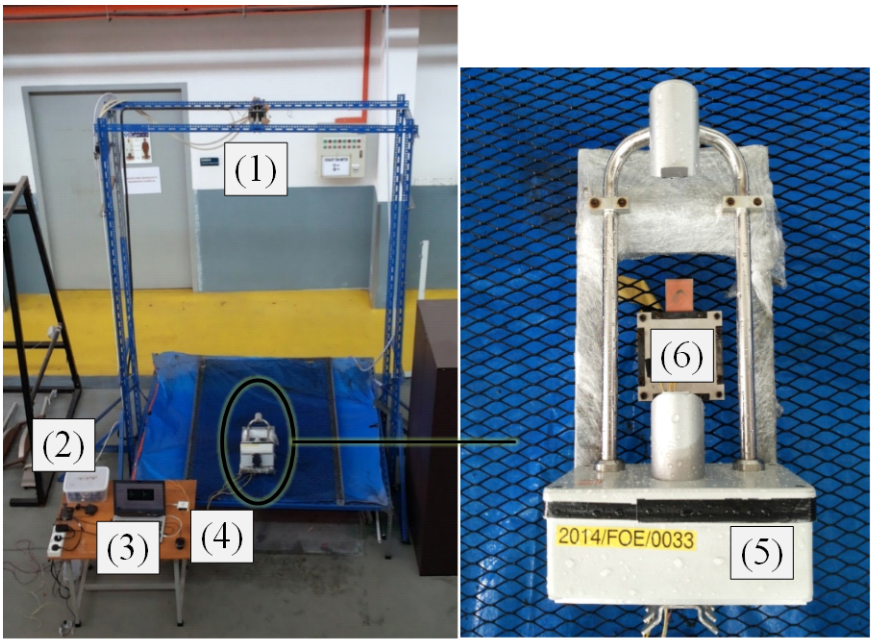


Figure 4.1: Overview of rain simulator: (1) rain nozzles; (2) control box; (3) laptop; (4) data logger; (5) laser precipitation monitor sensor; (6) piezoelectric beam.

the user to toggle the solenoid valves freely, which effectively turn the respective nozzles on or off. When a designated nozzle is selected, water will spray from the selected nozzle.

A laser precipitation monitor sensor (Thies CLIMA-5.4110.10.000) is deployed to measure the rain rate, and DSD of the artificial rain. The laser precipitation monitor sensor measures the rain parameter by estimating the sizes of water droplets that pass through the measuring area utilising optics and laser diodes. The sampling rate for the laser precipitation monitor sensor is 60 s. The recorded data is processed by using a software provided by the manufacturer, LNM View.

The piezoelectric beam utilised in this study is an off-the-shelf piezoelectric

beam (Mide-v25w). The piezoelectric beam was carefully clamped in an enclosed box shown in Figure 4.1. It is positioned right below the laser precipitation monitor sensor. The voltage produced by the piezoelectric beam is measured by connecting the two piezoelectric layers in series and across a 15 kΩ load resistor. With the aid of a laptop, a data logger (NI-USB6008) is used to record the voltage generated by the piezoelectric beam.

The experiment was conducted by setting two different flow rates for the two nozzles, resulting in four different rain rates. Each set of data records the voltage time response over a fixed duration of 300 s. The four artificial rains produced by the rain simulator are given in Table 4.1.

Table 4.1: List of different rain types produced by the rain simulator.

Rain no.	Nozzle	Flow rate (l/min)	Rain rate (mm/hr)
1	QPHA-6.5	1.3	33
2	QPHA-10	1.4	40
3	QPHA-6.5	2.1	62
4	QPHA-10	2.4	99

4.4 Numerical simulation

By using the piezoelectric beam model outlined in Chapter 2 and the artificial rain excitation model detailed in Section 4.2, the performance of the piezoelectric energy harvester under artificial rain can be studied. The numerical simulation of

the piezoelectric energy harvester is conducted by using MATLAB. The sampling rate for the numerical simulation is determined as 30 kHz. In the simulation, the two piezoelectric layers are connected in series and they are configured to be connected to a 15 kΩ load resistor. Piezoelectric beam impact parameters such as the added mass coefficient, and impact coefficient have to be determined before running the simulation.

The added mass coefficient varies over time. This is due to the water layer thickness on the surface of the piezoelectric beam varies as more water droplets are generated by the rain simulator. From the experimental data, frequency response graph is generated based on the voltage time response of one second interval. By using the generated frequency response graphs, the first mode damped natural frequency can be obtained. From there, the added mass coefficient of that particular one second interval can be estimated by using Equation (3.10). A boxplot consists of all the four artificial rains is presented in Figure 4.2.

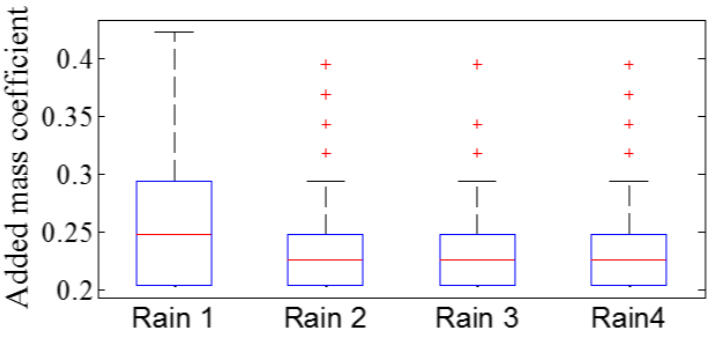


Figure 4.2: Boxplots consist of added mass coefficients for the four artificial rains (each group of added mass coefficient contains 300 samples).

From the four boxplots in Figure 4.2, the maximum added mass coefficient is approximately 0.4, while the minimum is approximately 0.2. Higher added

mass coefficient indicates higher water layer thickness formed on the surface of the piezoelectric beam. Having lower rain rate, the first artificial rain has larger collection of added mass coefficient samples with larger value. This is due to the water layer formed on the piezoelectric beam is having less tendency to be discharged from the surface by the water ripple motion produced by the impinging artificial raindrops.

In the numerical simulation of the artificial rain excitation model, the added mass coefficient for the four artificial rains are assumed to be constant throughout the 300 s duration. Since the median variation of the added mass coefficients for the four artificial rains were small, the added mass coefficient is fixed as a constant for the four artificial rains as 0.235. This is a good assumption as most of the recorded added mass coefficients are concentrated below 0.3. After obtaining the added mass coefficient, the impact coefficient can be estimated by using Equation (3.33) as 0.251.

The numerical simulation of the theoretical model was conducted using the 'lsim' function in MATLAB. The 'lsim' function is able to simulate the time response of continuous linear systems subjected to any given inputs. Whilst the numerical simulation for single droplet described in Chapter 2 is straight forward, the simulation for artificial rain excitation poses some challenges due to the stochastic nature of a rain.

In the artificial rain excitation model presented in Section 4.2, there are two random variables describing the stochastic nature of a rain, which are the droplet diameter and the drop position. The droplet diameter affects the average

force as well as the pulse function, while the drop position affects the magnitude of the mode shape function.

The droplet diameter is governed by the DSD of the particular artificial rain. From the DSDs recorded in the four artificial rains, it was found that each set of the DSDs was slightly different. The DSDs exhibited a lognormal distribution, which the distribution was skewed to the right. This lognormal distribution is governed by two lognormal parameters, μ and σ. The lognormal parameters could be obtained by fitting the DSDs obtained experimentally using the 'lognfit' command in MATLAB. The lognormal parameters for the four rains are illustrated in Table 4.2. Despite having higher rain rate, the total number of droplets for rain 2 is lower than rain 1. This is due to different nozzles utilised to generate the two artificial rains. According to the DSDs obtained using the laser precipitation monitor sensor (Figure 4.4), the number of higher diameter water droplet produced by QPHA-10 was higher than of QPHA-6.5 at a low flow rate. As a result, the rain rate for rain 2 is slightly higher than rain 1.

In the numerical implementation of the artificial rain excitation model, there are two counters: the drop counter and impact duration counter. The drop counter checks the duration of individual drops, while the impact duration counter checks the impact duration for each droplet. The duration of individual drops was monitored by using the drop period, which can be calculated by using Equation (4.6). The total number of droplets over duration of 300 s and their respective drop periods are computed in Table 4.2.

Table 4.2: Rain no., nozzle used, rain rate, lognormal parameters (μ and σ), total number of droplets, and drop period of the four artificial rains.

Rain no.	**Nozzle**	**Rain rate (mm/hr)**	μ	σ	**Total number of droplets**	**Drop period (ms)**
1	QPHA-6.5	33	-0.365	0.450	17120	17.52
2	QPHA-10	40	-0.336	0.493	15505	19.35
3	QPHA-6.5	62	-0.361	0.523	22770	13.18
4	QPHA-10	99	-0.453	0.534	40770	7.36

The flow chart for the artificial rain generalised excitation force implementation in MATLAB is presented in Figure 4.3. Droplet diameter and impact position are calculated using Equation (4.1) and Equation (4.2) respectively. The droplet diameter is set to be more than 0.125 mm as this is the smallest droplet diameter that the laser precipitation monitor sensor is able to measure. The impact duration can be estimated using Equation (4.4). When the impact duration counter is less than the impact duration, the generalised excitation force can be calculated as $F_a(t) = f_{avg}(D_n)\varphi(x_n)$. The generalised excitation force will set as zero as the impact duration counter exceeds the impact duration. Once the drop period counter is larger or equal to the drop period, a new droplet will be introduced. The simulation iterates until time t is greater or equal to the maximum time.

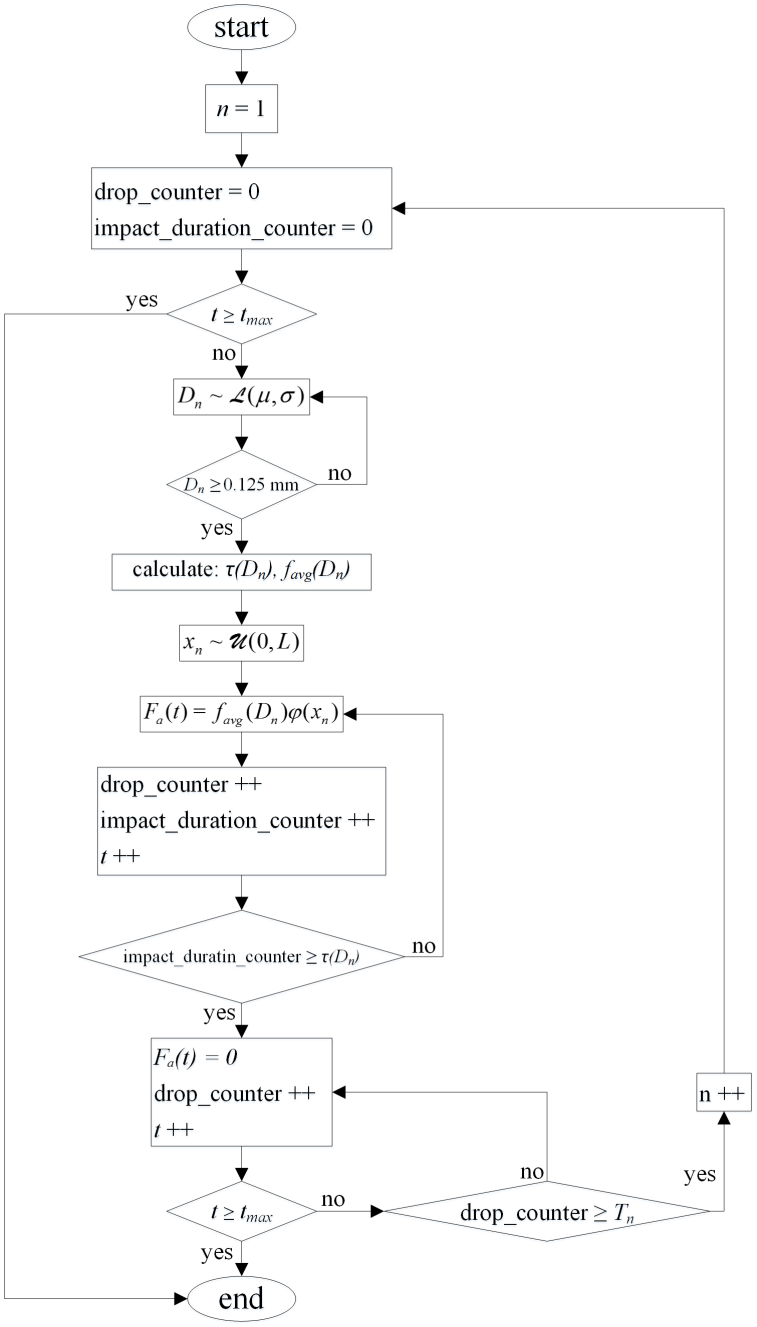


Figure 4.3: Flow chart for computation of artificial rain model.

4.5 Results and discussion

Experiments were performed to verify the artificial rain excitation model. In the experiment, the performance of the piezoelectric energy harvester under four

artificial rains with four different rain rates were tested. The rain number and its rain rate are tabulated in Table 4.2. The duration of each experiment was fixed as 300 s. To demonstrate the effect of the variability due to DSD, a total of 10 theoretical simulations were conducted. In the experimental and theoretical studies, the two piezoelectric layers were connected in series and then connected to a 15 kΩ load resistor.

4.5.1 Drop size distribution

The DSDs for all the artificial rains generated by the rain simulator were measured using a laser precipitation monitor sensor. A conventional DSD provides the number of droplets per unit volume per unit interval of drop diameter, with the unit of $m^{-3}mm^{-1}$ [41]. This is to give a general measurement on how the rain droplets distributed at the location where the measurement is being made. The interest in this study is to examine the performance of a piezoelectric energy harvester excited under artificial rain. To give a more direct measurement, the DSD in this study records the total number of droplets accumulated over 300 s with a measuring area similar to the surface area of the piezoelectric beam used in this study (1766.1 mm^2).

The experimental and mean of 10 theoretical DSDs for the four artificial rains are given in Figure 4.4. The x-axis in the DSD used in this study indicates the bin-centre of each bin. A total of 10 numerical simulations were conducted for the four artificial rains using the lognormal parameters in Table 4.2. The mean

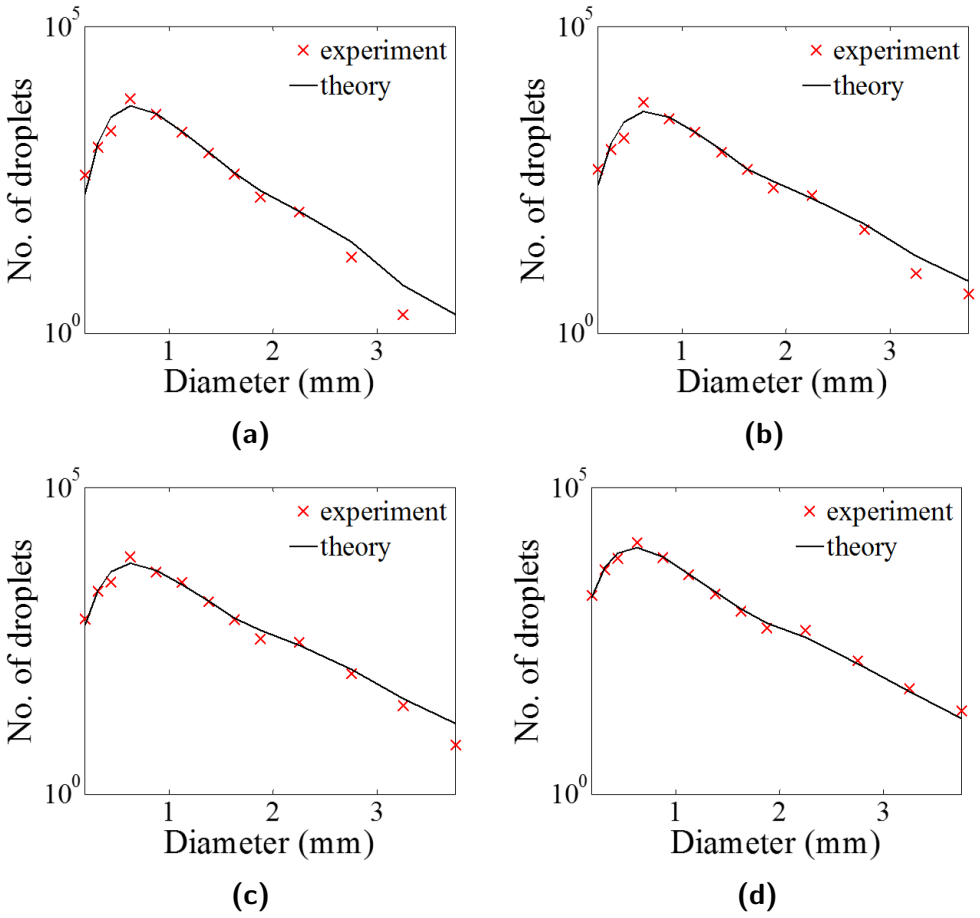


Figure 4.4: Experimental and theoretical (mean of 10 samples) drop size distributions (DSD) for: (a) rain 1; (b) rain 2; (c) rain 3; (d) rain 4.

of 10 DSD simulation results were obtained and plotted against the bin-centre of each diameter bins.

The accuracy of the theoretical DSDs are verified using coefficient of determination (R^2):

$$R^2 = 1 - \frac{\sum_{i=1}^{n}(experiment_i - theory_i)^2}{\sum_{i=1}^{n}(experiment_i - \overline{theory})^2}$$

$$\overline{theory} = \frac{1}{n}\sum_{i=1}^{n} theory_i \tag{4.7}$$

The R^2 value for the four artificial rains were calculated to be 0.9069, 0.8773, 0.9309, and 0.9612 respectively. Overall, the theoretical results matched well with the experimental results. From the DSDs shown in Figure 4.4, as the rain rate increases, the number of water droplet with higher diameter increases. The maximum recorded water droplet was found to be approximately 3.75 mm.

4.5.2 Performance of the rain energy harvester

The performance of the rain energy harvester under artificial rains is discussed in this section. Compared to actual rain, the artificial rain was generated with a fixed rain rate. By fixing the rain rate and using experiment duration of 300 s, the effect of two other random parameters i.e. the raindrop diameter and the drop position on the piezoelectric beam can be investigated. The experimental and theoretical voltage time response graphs for the four rains are presented in Figure 4.5. The first 1.5 s of the experimental and theoretical voltage time response graphs for the four artificial rains are given in Figure 4.6. The two PZT layers were configured to be connected in series and measured across a 15 kΩ load resistor for both experiment and theory cases.

Analyse the two cases qualitatively in Figure 4.5 and Figure 4.6, it is noted that both the experimental and theoretical voltage time response graphs are getting denser while the rain rate increases. This is due to the increase in the total number of artificial rain droplets that were impacting on the surface of the piezoelectric beam. The theoretical results were able to estimate the overall

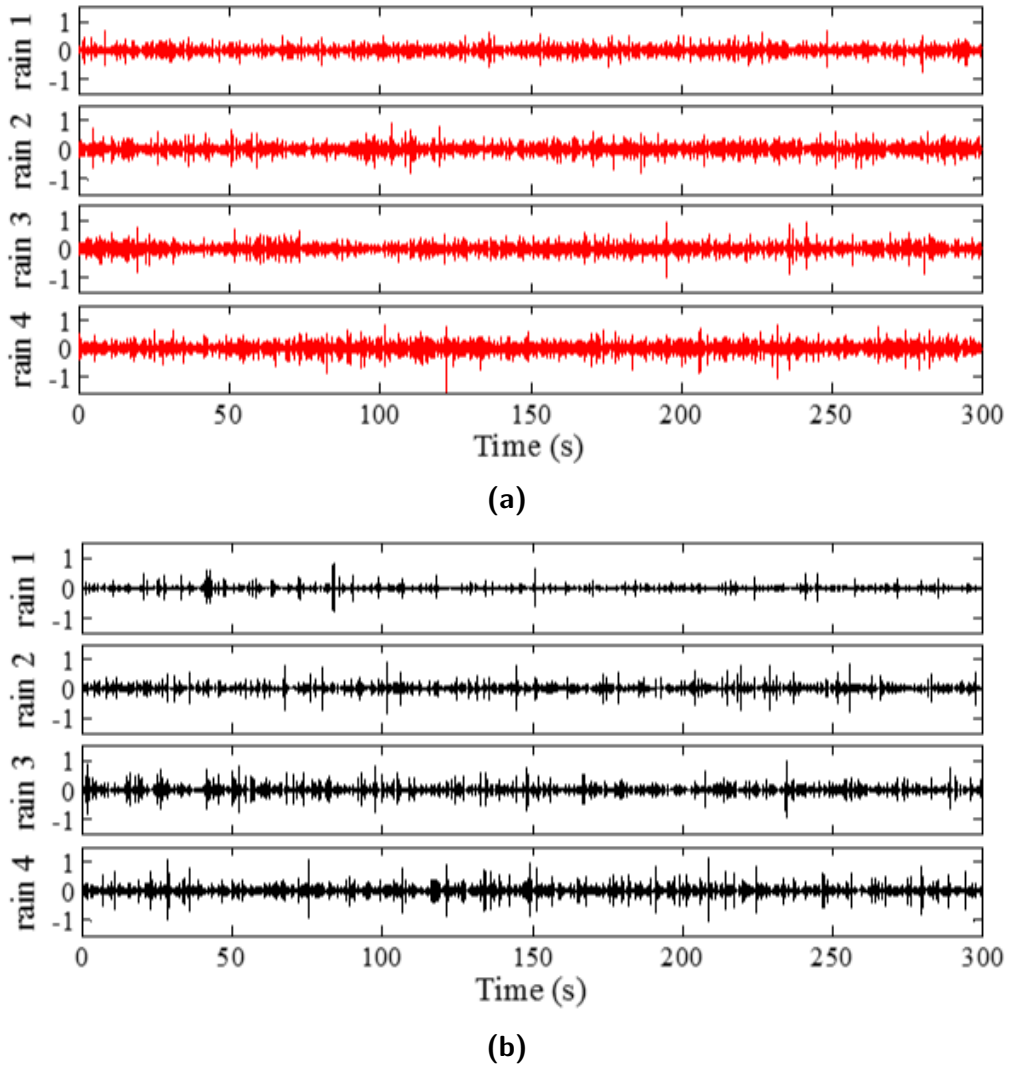


Figure 4.5: The (a) experimental and (b) theoretical results for the four artificial rains, where the x-axis represents time (s); y-axis represents voltage produced by the piezoelectric energy harvester (V).

performance of the piezoelectric energy harvester compared to the experimental results.

To examine the energy accumulated over time, Equation (3.34) is employed. A total of 10 samples of theoretical energy accumulation graphs were simulated for each of the four artificial rains. The experimental and theoretical energy accumulated over time for the four artificial rains are given in Figure 4.7.

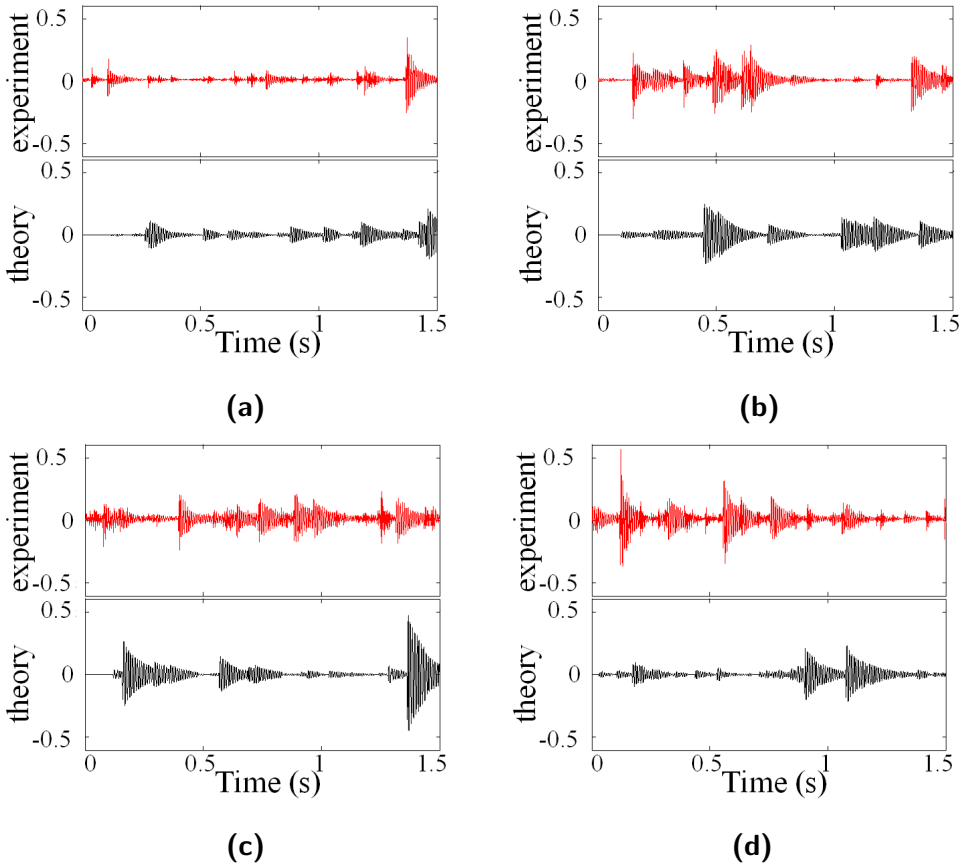


Figure 4.6: The experimental and theoretical voltage time response graphs for the first 1.5 s of: (a) rain 1, (b) rain 2, (c) rain 3, (d) rain 4; where the x-axis represents time (s); y-axis represents voltage produced by the piezoelectric energy harvester (V).

The experimental total energy accumulated over the period of 300 s for the four artificial rains were 22.49 μJ, 47.76 μJ, 49.35 μJ, and 62.53 μJ respectively; while the mean of the 10 theoretical total energy accumulation for the four artificial rains were 18.81 μJ,42.64 μJ, 59.46 μJ, 78.05 μJ respectively. Overall, the experimental and theoretical results were in good agreement with percentage difference of 19.54 %, 12.01 %, 17.00 %, and 19.88 % for the four artificial rains respectively. From Figure 4.7, in the early 30 s of the energy accumulation graphs for the four artificial rains, the experimental energy accumulation graphs were

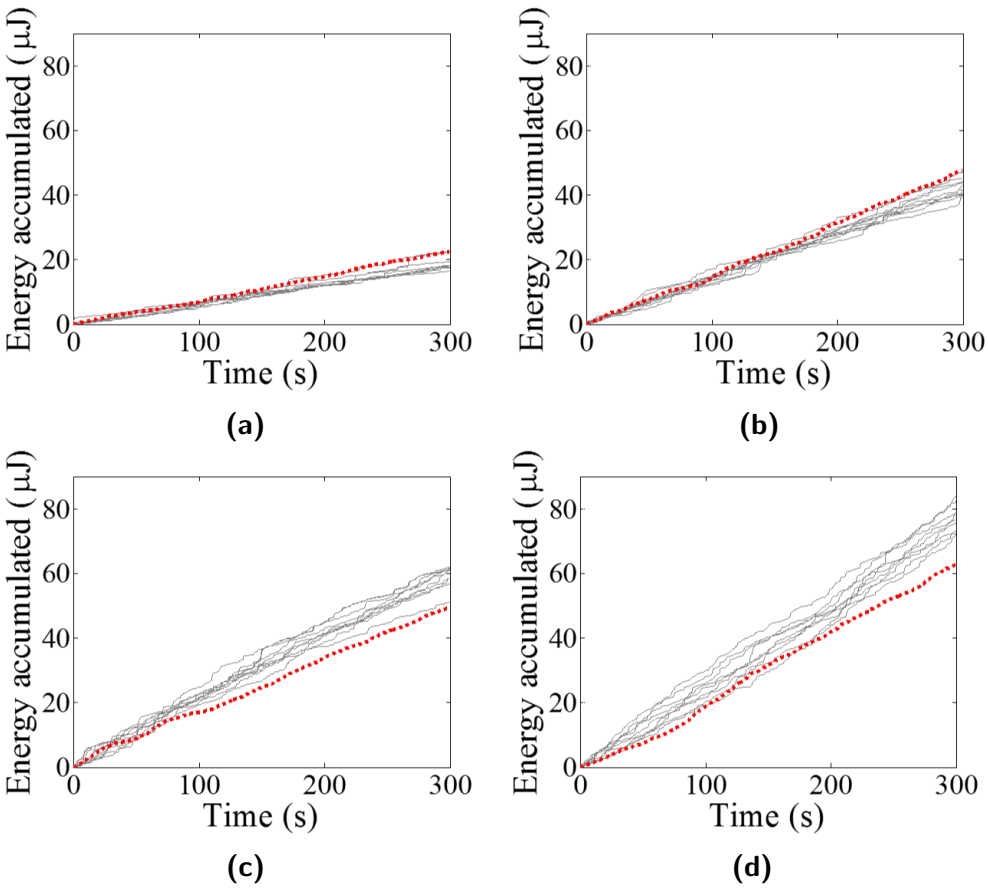


Figure 4.7: Experimental (red dotted line) and theoretical (10 samples in grey lines) energy accumulation graphs for: (a) rain 1; (b) rain 2; (c) rain 3; (d) rain 4.

found to be within the range of the theoretical accumulation curves. This shows that the percentage differences of the experimental and theoretical results are contributed by the accumulation of error over the period of 300 s.

The cause of this accumulation of error is due to the combined effect of the randomness of the DSD and impact position. As the number of droplet impact increases, the effect of these parameters will become more apparent, which is reflected by the increase in the spread of total energy accumulated over time.

Both experimental and theoretical results exhibited a linear trend with positive gradient. The effect of randomness (i.e. such as droplet diameter and impact position) was smoothened in the long run with an experiment duration of 300 s. Therefore, the consistency of the linear behaviour can be ensured. The gradient of the energy accumulation graphs is the power produced by the energy harvester. The gradients are obtained by fitting a linear curve that starts with zero using MATLAB. The experimental and theoretical power generated by the piezoelectric energy harvester from the four artificial rains are tabulated in Table 4.3.

As the rain rate increases, the slope of the gradient increases as well. This implies that the rain rate and the power generated by the energy harvester has a position correlation in a controlled environment. Overall, the theoretical results showed a good agreement with the experimental results.

Table 4.3: Experimental and theoretical power produced by the piezoelectric energy harvester from the four simulated artificial rains.

Rain no.	**Rain rate(mm/hr)**	**Power generated (μW)**		
		Experiment	**Theory (mean)**	**% Diff**
1	33	0.074	0.063	17.46
2	40	0.156	0.143	9.09
3	62	0.167	0.205	18.54
4	99	0.207	0.251	17.53

4.6 Chapter Conclusion

This chapter further extends the multiple droplet excitation model by testing the piezoelectric energy harvester under simulated artificial rain. Experimental results showed that the artificial rain excitation model was able to estimate the energy produced by a piezoelectric energy harvester. This is achieved by introducing two random parameters into the artificial rain excitation model, which were the droplet size and the droplet impact position. From the experimental and theoretical results, when the rain rate of the artificial rain is 99 mm/hr, the piezoelectric energy harvester is able to generate power of 0.207 μW and 0.251 μW respectively.

Four artificial rains with different rain rates (33 mm/hr, 40 mm/hr, 62 mm/hr, and 99 mm/hr) were considered in this study. With increasing rain rate, the total energy accumulated over a fixed period of time (300 s) increased as well. When the rain rate increases, more raindrops are anticipated to impact on the piezoelectric beam. Thus higher energy could be accumulated over time. In a controlled environment, experimental and theoretical results revealed that the rain rate and power generated by the harvester exhibit positive correlation. By extending this study, the theoretical excitation model for an actual rain can be accomplished by varying the rain rate.

Chapter 5

Performance of the energy harvester in actual rain

5.1 Introduction

In Chapter 4, theoretical and experimental study based on the performance of the raindrop impact energy harvester on artificial rain were conducted. In actual rain, the rain rate varies unpredictably, this will alter the rain drop size distribution (DSD). Furthermore, the number of raindrop that impact the piezoelectric beam increases with the rain rate. As a result, the variation of rain rate will affect the energy production of the energy harvester. The purpose of this chapter is to investigate the performance of a raindrop impact energy harvester in actual rain, and to formulate a theoretical model to estimate the energy generation of the raindrop impact energy harvester given the rain rate.

The excitation model for actual rain is developed by integrating the variation of the rain rate that affects the rain DSD and raindrop count into the artificial rain excitation model, which was discussed in Chapter 4. Section 5.2 discusses the actual rain excitation model and also the implementation of the Lognormal DSD Model in the numerical simulation. The performance of the energy harvester in actual rain is evaluated in Section 5.3. The theoretical model is validated in Section 5.4 by comparing with the experimental results. The theoretical model is modified according to the experimental result to demonstrate the practicability of the actual rain excitation model. The implication of the results is presented in Section 5.5. Section 5.6 concludes the chapter.

5.2 Actual rain excitation model

In this section, the external work done due to actual rain is devised. The piezoelectric beam model presented in Chapter 2 describes the dynamical response of a piezoelectric beam and voltage generation due to base excitation. Chapter 3 studies the dynamics of a water droplet impact on the piezoelectric beam. Added mass coefficient and impact coefficient introduced in Chapter 3 are able to describe the water layer accumulation on the piezoelectric beam and the post impact behaviour of a water droplet respectively. The effect of water droplet impact position is also studied in Chapter 3. In Chapter 4, the piezoelectric beam model is extended to incorporate artificial rain excitation, which rain rate is fixed.

The artificial rain excitation model can be expanded into actual rain excitation model by varying the rain rate over time. The implementation of the Lognormal DSD Model in the numerical simulation is presented in this section. The two fitting parameters for Lognormal DSD Model, and average raindrop count are plotted and discussed in this section.

5.2.1 Actual rain excitation model

In Chapter 4, the work done due to artificial rain using fixed rain rate is presented. The mathematical model for a piezoelectric beam that incorporates the effect of water layer accumulation is recalled in Equation (3.12) and Equation (2.35) as:

$$(1 + C_a)\underline{M}\ddot{r}(t) + \underline{D}_a\dot{r}(t) + \underline{K}r(t) - \theta V(t) = F(t)$$

$$\theta^t r(t) + C_p V(t) = q(t)$$

This section expands artificial rain excitation model to describe actual rain scenario. The difference between artificial rain and actual rain is that the rain rate for actual rain varies over time. Recall the artificial rain excitation model, Equation (4.5):

$$F_a(t) = \sum_{n=1}^{N_t} [f_{avg}(D_n)\varphi(x_n)\eta_a(t)]$$

$$\eta_a(t) = \Phi[t - (n-1)T_n] - \Phi[t - \tau(D_n) - (n-1)T_n]$$

where, N_t is the total number of water droplets; n is the rain droplet count; $f_{avg}(D_n)$ is the average impact force due to n^{th} droplet diameter (D_n); φ is the

normalised mode shape function; x_n is the impact position of the nth droplet; Φ is the Heaviside function; $\tau(D_n)$ is the impact duration of the nth droplet; T_n is the drop period; $\eta_a(t)$ is the pulse function for artificial rain.

The equations for the average force and impact duration of an impinging water droplet, illustrated in Equation (4.3) and (4.4) respectively are given as:

$$f_{avg}(D_n) = \frac{[1 - C_i(n)]m_w(D_n)v_w(D_n)}{\tau(D_n)}$$

$$\tau(D_n) = \frac{D_n}{v_w(D_n)}$$

Following the model developed for the artificial rain, the raindrop diameter and impact location can be generated via random generator function using lognormal and uniform distribution respectively, given as:

$$D_n \sim \mathscr{L}(\mu(R), \sigma(R))$$

$$x_n \sim \mathscr{U}(0, L) \tag{5.1}$$

According to literature, the empirical parameters describing DSD changes with rain rate [72]. Therefore the two fitting parameters for the lognormal distribution (σ and μ) in Equation (5.1) are in a function of rain rate.

Rain rate changes in actual rain, this will vary the drop period. Therefore, in the actual rain excitation model, the drop period is expressed with a function of rain rate. The pulse function for the actual rain excitation model is written

as:

$$\eta_r(t) = \Phi[t - (n-1)T_n(R)] - \Phi[t - \tau(D_n) - (n-1)T_n(R)]$$

$$T_n = \frac{60}{a_r \overline{N}_d(R)} \tag{5.2}$$

where, a_r is the scaling factor; $\overline{N}_d$ is the average number of droplet. The average number of droplet is recorded across a measuring area of 4513.4 mm^2. A scaling factor of 0.3913 is applied so that it gives the average number of droplet that impact the surface of the piezoelectric beam.

The laser precipitation monitor sensor is able to measure the total raindrop count for every one minute (the sampling time of the sensor). The average raindrop count can be expressed as a function of rain rate as well. This is achieved by relating the average raindrop count provided by the laser precipitation monitor sensor to the rain rate. The average raindrop count equation will be further discussed in Section 5.2.2. By integrating the average number of droplet over the period of the rain, the total number of raindrops that impact on the surface of the piezoelectric beam can be obtained as:

$$N_r = a_r \int_0^t \overline{N}_d(R) dt \tag{5.3}$$

The final form of the generalised excitation force due to actual rain droplet impact is written as:

$$F_r(t) = \sum_{n=1}^{N_r} [f_{avg}(D_n)\varphi(x_n)\eta_r(t)]$$

$$\eta_r(t) = \Phi[t - (n-1)T_n(R)] - \Phi[t - \tau(D_n) - (n-1)T_n(R)] \tag{5.4}$$

5.2.2 Drop size distribution model

The stochastic nature of rain is characterised by rain rate and DSD [41]. In Chapter 4, artificial rain was replicated in laboratory condition, where the rain rate is fixed. In actual rain, the rain rate is reported to be changing over time and it is found that the DSD varies when the rain rate changes [72]. The study of DSD can be applied in various practical uses such as: microwave network [73], radio communications [74], and cloud modelling [75]. Therefore, rain DSD is a salient parameter in describing a raining event. The nature of rain DSD varies not only to the rain rate but also to climatic zone and geographical area [72, 76]. As a result, it is tough to propose a generic DSD model to describe the rain DSD for every rain type and location.

Over the years, several statistical functions for rain DSD had been developed. The Exponential DSD Model introduced by Marshall and Palmer [77] was reported to be inaccurate when the sampling time is lower than one minute as it tends to exaggerate the smallest and largest raindrop count [78]. The Gamma DSD Model suggested by Ulbrich [79] provides a wide range of distribution shapes. The Lognormal DSD Model proposed by Ajayi and Olsen [80] has a steeper gradient at lower end of the raindrop diameter spectrum. Lognormal DSD Model is suitable in describing the rain DSD for tropical climate [72]. Several implementations of Lognormal DSD Model in tropical climate countries found in literature are: Singapore [81], South Africa [82], and Malaysia [83].

Since this study is conducted in a tropical climate country, the Lognormal DSD Model is selected.

The rain DSD shows the total number of rain droplets per unit size interval per unit volume of space with a unit of $m^{-3}mm^{-1}$. The excitation model presented in Equation (5.4) requires the total number of droplet instead of raindrop density. In order to facilitate the implementation of the rain DSD onto the excitation, the total number of raindrop is utilised instead of raindrop density. Hence, the average raindrop counts for the respective rain rate bins are determined.

In the implementation of the Lognormal DSD Model, two fitting parameters are used, which are σ and μ. Furthermore, by using the data recorded by the laser precipitation monitor sensor, the average rain drop count can be obtained. In the essence of obtaining a stable distribution, a total of 10 rain events of 1616 minutes were recorded. The flow chart for generating the two fitting parameters and the average drop count is presented in Figure 5.1.

The instantaneous DSDs recorded from each rain events are categorised and sorted into designated rain rate bin. The rain rate bin number (i) and its respective rain rate range is provided in Table 5.1. After sorting all the DSDs, the DSDs in the respective bins are merged. For comparison purpose, the total number of raindrop collected over the 10 rains were converted to raindrop density by using the following Formula [41]:

$$N(D_{w,j}) = \frac{N_{d,j}}{A_s T_s [\Delta D_{w,j}][v(D_{w,j})}] \tag{5.5}$$

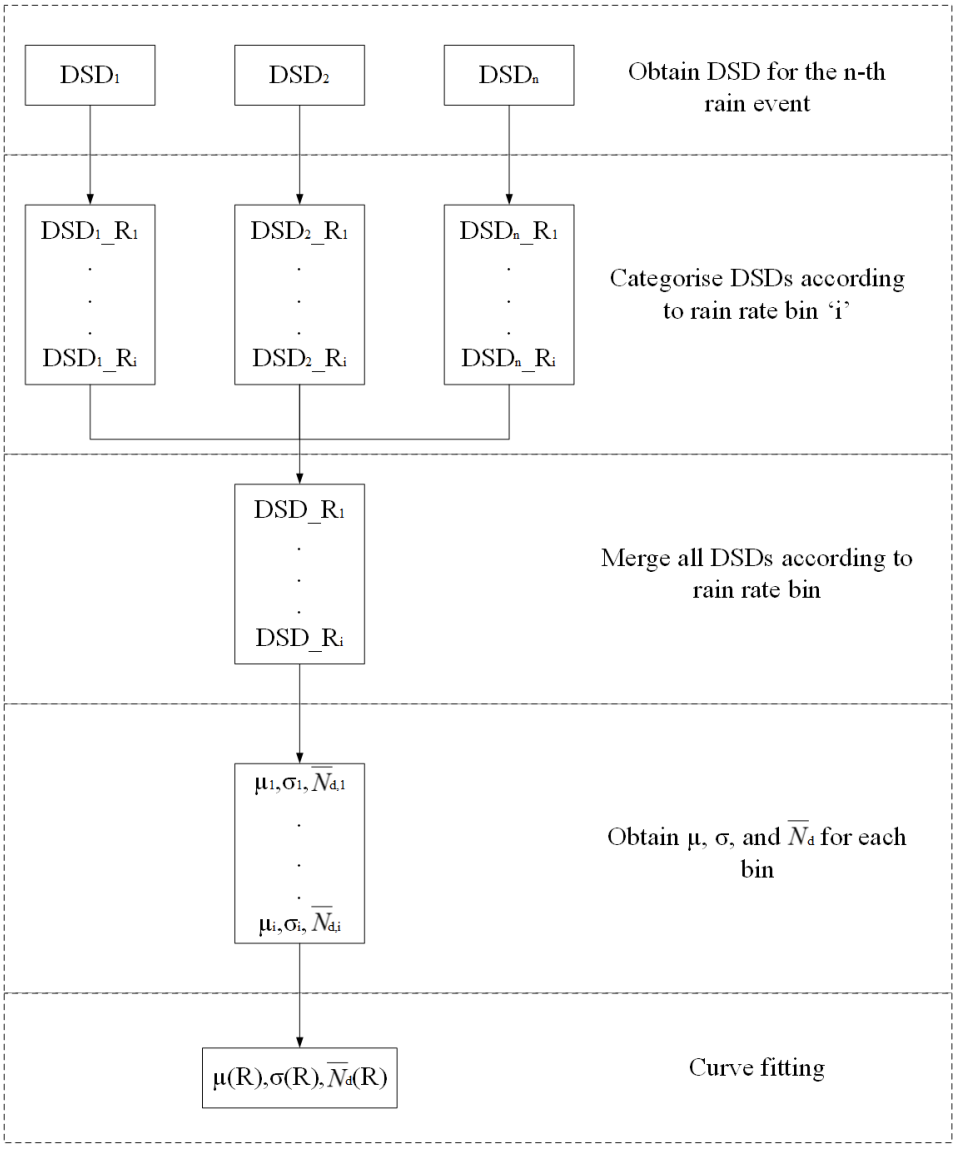


Figure 5.1: Flow chart of obtaining the average number of droplet($\overline{N}_d$), and two fitting parameters for the lognormal distribution model (σ and μ).

where, $N_{d,j}$, is the number of raindrops of the jth diameter bin; $v(D_{w,j})$ is the velocity of the raindrop in the jth diameter bin; $\Delta D_{w,j}$ is the bin width of the jth diameter bin; A_s and T_s is the measuring area and the total integration time of the laser precipitation monitor sensor respectively.

The merged rain DSDs for all the rain rate bins are presented in Figure

Table 5.1: The rain rate range for respective rain rate bin.

Rain rate bin, i	**Rain rate range (mm/hr)**
1	$R < 25$
2	$25 \leq R < 50$
3	$50 \leq R < 100$
4	$100 \leq R < 150$
5	$150 \leq R < 200$
6	$200 \leq R < 250$
7	$250 \leq R < 300$
8	$300 \leq R < 350$
9	$350 \leq R < 450$

5.2. From Figure 5.2, it can be observed that as the rain rate increases, the total density of the raindrop count increases as well. Furthermore, it is noticed that the number of raindrop with larger diameter increases as the rain rate increases.

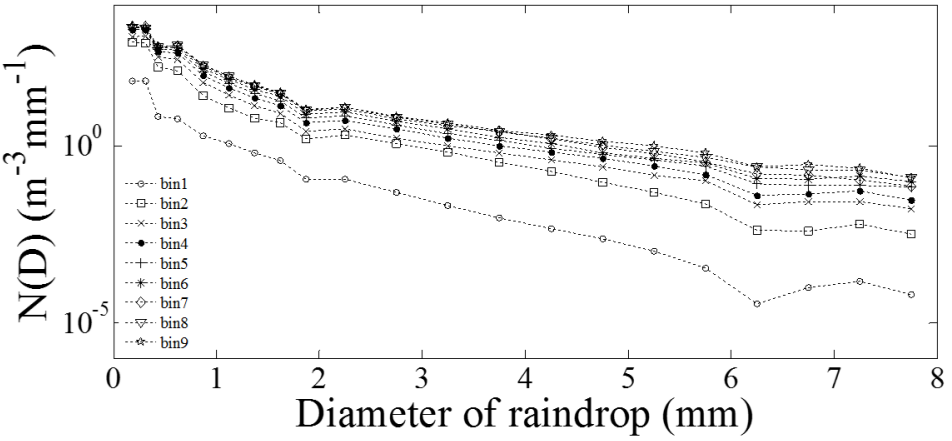


Figure 5.2: Rain DSD of different rain rate bins obtained from experiment 10 rain events.

The two fitting parameters for Lognormal DSD Model for each rain rate bins (σ and μ) are estimated using MATLAB. The average number of droplet

($\overline{N}_d$) for each rain rate bin can be obtained by summing up the total number of droplets in the respective DSD and divided by the total number of DSDs in that particular rain rate bin. After obtaining the two fitting parameters and the average number of droplet, curve fitting was conducted using MATLAB. Each rain rate bin is represented by its bin-centre value. By performing curve fitting, a continuous function of rain rate relating the two fitting parameters, and the average number of droplet, can be realised. The curve fitted equations for the two fitting parameters and the average number of droplet are:

$$\sigma(R) = 0.0003384R + 0.5912 \tag{5.6}$$

$$\mu(R) = -0.1892e^{-0.03581R} - 0.961e^{-0.0006652R} \tag{5.7}$$

$$\overline{N}_d(R) = 0.0002897R^3 - 0.3746R^2 + 155.1R \tag{5.8}$$

where, $\overline{N}_d(0) = 0$, and the maximum rain rate is set as 450 mm/hr.

The experiment data and the three fitted curves are given in Figure 5.3. Overall, the fitted curves of the two fitting parameters and the average number of droplet showed a good agreement to the experiment data, with R^2 values of 0.9951, 0.9792, and 0.9917 respectively. The fitted values of the two fitting parameters will be used to determine the DSD for different rain rate bins; whist the average number of droplet indicates the frequency of raindrop impact in one minute duration in the theoretical model.

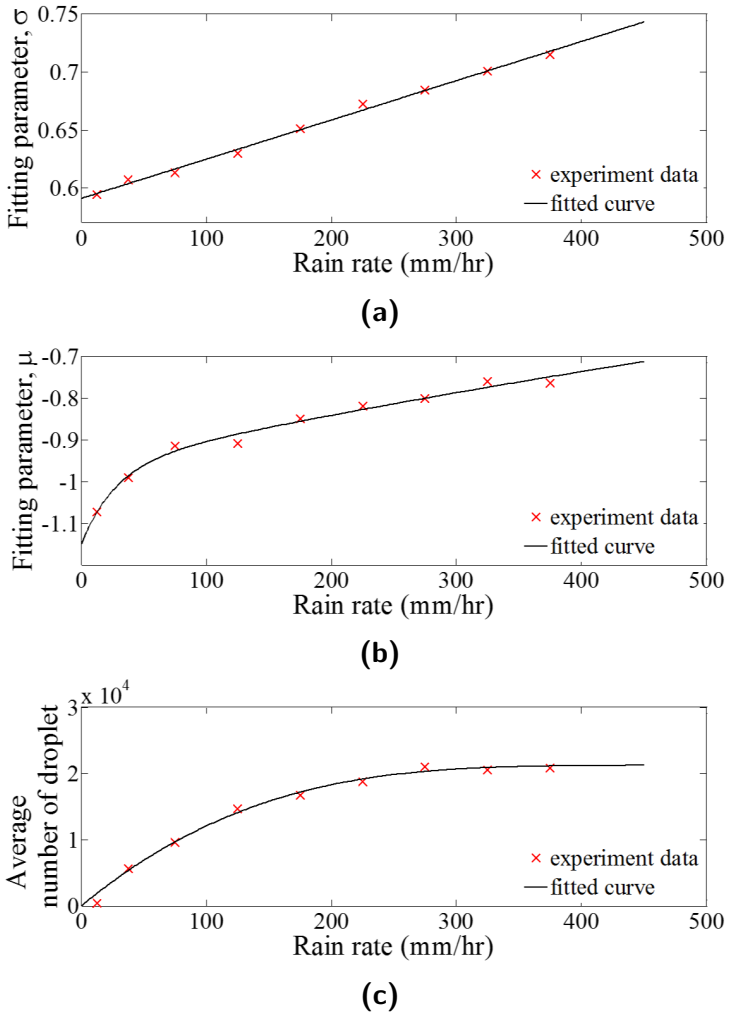


Figure 5.3: Experiment data and fitted curve for: (a) fitting parameter, σ;(b) fitting parameter, μ; (c) average number of droplet, $\overline{N}_d$.

5.3 Performance of the harvester in actual rain

The performance of a raindrop impact energy harvester using a commercial piezoelectric beam is investigated in this section. Actual field test was carried out in order to evaluate the performance of the raindrop impact energy harvester in actual rain. In this study, a total of 10 rains were recorded. The voltage time

response graphs for the 10 rains are provided in Appendix C. The experiments were carried out by using a laser precipitation monitor sensor to measure the rain parameters. A data logger is used to record voltage produced by the piezoelectric beam. The experiment methodology is presented in Section 5.3.1. An evaluation on the performance of the raindrop impact energy harvester in actual rain condition is given in Section 5.3.2. The influence water layer accumulation on the surface of the piezoelectric beam are also discussed in this section.

5.3.1 Experiment methodology

To record the rain parameters, a laser precipitation monitor sensor (Thies CLIMA-5.4110.10.000) is deployed. The laser precipitation monitor sensor is able to measure rain rate and DSD with a sampling time of one minute. The raindrop diameter measurement range of the laser precipitation monitor sensor is 0.125 mm to 8.0 mm. The raindrop diameter classes and their respective diameter range is illustrated in Table 5.2.

The overview of the laser precipitation monitor sensor together with the piezoelectric beam, and the schematics of the experimental setup are depicted in Figure 5.4. The piezoelectric beam (Mide-v25w) used in this study is clamped tightly in a water-proof aluminium casing. The piezoelectric beam setup is positioned right under the laser precipitation monitor sensor to ensure that most of the measured raindrops impact on the surface of the piezoelectric beam. The two PZT layers of the piezoelectric beam are connected in series. The voltage generated by the piezoelectric beam is measured using a data logger (NI-USB

Table 5.2: Rain drop diameter class.

Class	Diameter range (mm)	Class	Diameter range (mm)
1	$0.125 \leq D < 0.250$	**12**	$3.000 \leq D < 3.500$
2	$0.250 \leq D < 0.375$	**13**	$3.500 \leq D < 4.000$
3	$0.375 \leq D < 0.500$	**14**	$4.000 \leq D < 4.500$
4	$0.500 \leq D < 0.750$	**15**	$4.500 \leq D < 5.000$
5	$0.750 \leq D < 1.000$	**16**	$5.000 \leq D < 5.500$
6	$1.000 \leq D < 1.250$	**17**	$5.500 \leq D < 6.000$
7	$1.250 \leq D < 1.500$	**18**	$6.000 \leq D < 6.500$
8	$1.500 \leq D < 1.750$	**19**	$6.500 \leq D < 7.000$
9	$1.750 \leq D < 2.000$	**20**	$7.000 \leq D < 7.500$
10	$2.000 \leq D < 2.500$	**21**	$7.500 \leq D < 8.000$
11	$2.500 \leq D < 3.000$		

6008) across a 15 kΩ load resistor. The voltage measuring sampling rate is 2 kHz.

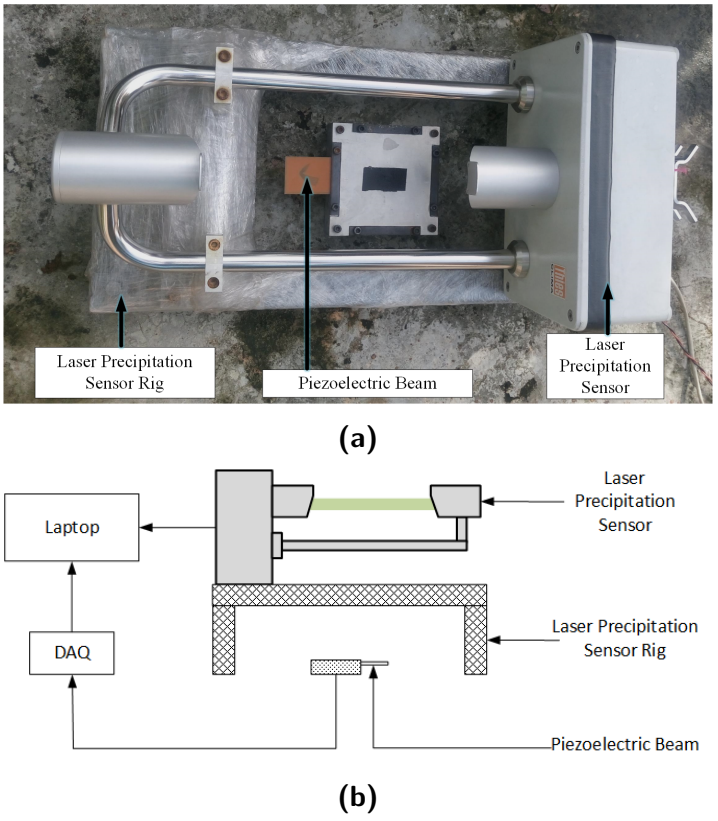


Figure 5.4: (a) Overview and (b) schematics of the actual rain experiment setup.

5.3.2 Experiment results

Performance of the piezoelectric beam was evaluated under actual rain. The rain rate and instantaneous voltage graphs are presented in Figure 5.5. The rain spans for a period of 3540 s, with the highest rain rate of 407.3 mm/hr recorded at $t = 840s$. For analysis purposes, the rain rate and instantaneous voltage results are sliced into four sections: S1($t \leq 360s$); S2($360s \leq t < 1080s$); S3($1080s \leq t < 2460s$); and S4($t \geq 2460s$).

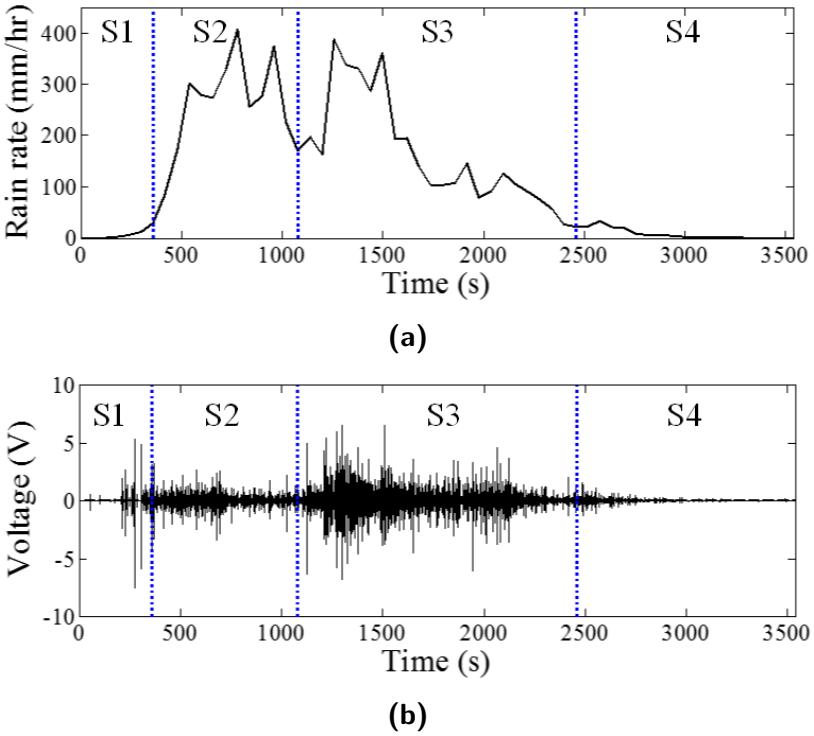


Figure 5.5: Time series graphs of (a) rain rate; (b) voltage. The time series graphs were segmented into four sections: S1($t \leq 360s$; S2($360s \leq t < 1080s$); S3($1080s \leq t < 2460s$); and S4($t \geq 2460s$).

In the beginning of the rain (S1), the rain rate was less than 25 mm/hr. Despite lower rain rate, the maximum absolute peak voltage throughout the whole rain was measured to be 7.60 V. According to the DSD model presented

in Section 5.2.2, the tendency of higher droplet size impinging the piezoelectric beam is higher as the rain rate increases. From Equation (4.3), the increase in raindrop diameter will increase the average impact force. Hence, higher peak voltage will be generated by the piezoelectric beam. Therefore, the spikes in the peak voltage observed in S1 can be explained by the sudden impingement of large raindrop diameter.

Heavy rains weres potted in S2 and S3. The first heavy rain occurred in S2 has the highest local maxima rain rate of 407.3 mm/hr; whereas the second heavy rain happened at S3 has the highest local maxima rain rate of 387.4 mm/hr. Even though the rain rates of both heavy rain periods were similar, the absolute peak voltages in S2 were relatively lower in comparison with S3. One of the explanations for this occurrence is the raindrops that impacted on the piezoelectric beam in S2 were having lower raindrop diameter. In S4, the rain started to dwindle. As the rain rate reduces, the tendency of larger raindrop diameter that impacts the piezoelectric beam reduces as well. Therefore, the absolute peak voltage produced by the piezoelectric beam in S4 was lower than S2 and S3 in overall.

During the actual rain experiment, water layer accumulation was observed, as shown in Figure 5.6. Theoretical and experimental investigations on the effect of water accumulation on the piezoelectric beam had been carried out and discussed in Chapter 3 and 4. Having irregular geometry, the volume and size of the water layer during its formation is usually hard to be deduced. The modal

mass of the water layer can be estimated by using the added mass coefficient highlighted in Section 3.2.



Figure 5.6: Water layer formed on the piezoelectric beam.

In order to obtain the time coarse history of the formation of the water layer, the added mass coefficient of every one minute interval was recorded. The added mass coefficient is attainable by using Equation (3.13), using the first mode natural frequency. The first mode natural frequency for the nth minute can be acquired by sliding a one minute window at that interval and performing Fast Fourier Transform (FFT) on the voltage time response graph using MATLAB.

According Equation (3.10), the added mass coefficient is actually defining the ratio between the modal mass of the piezoelectric beam to the modal mass of the formed water layer on its surface. There will be no water layer on the piezoelectric beam when the $C_a = 0$, while the modal mass of the water layer has the same modal mass of the piezoelectric beam without any water layer when the when $C_a = 1$. The added mass coefficient graph is plotted in Figure 5.7.

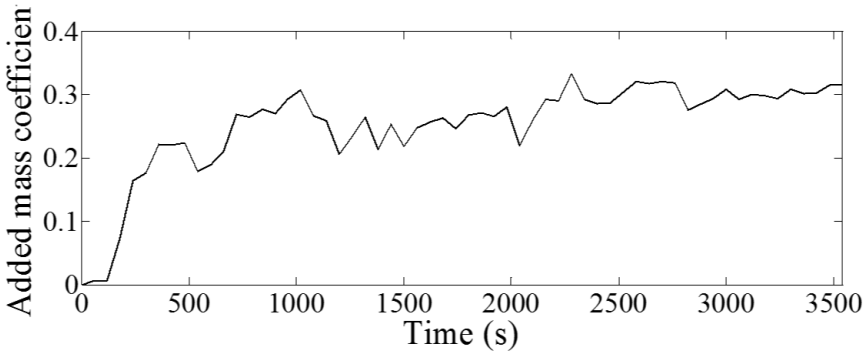


Figure 5.7: Time series graph of added mass coefficient.

The added mass coefficient was reported to be close to zero at the beginning of the rain ($t < 180s$). This is due to low rain rate and there was no water layer formed on the piezoelectric beam surface. As the rain progresses, more raindrops were being introduced to the surface of the piezoelectric beam and the added mass coefficient begun to increase accordingly.

According to the result, the added mass coefficient fluctuated within the range of 0.17 and 0.33. The cause of the fluctuations can be explained by the variation of the water layer thickness on the surface of the piezoelectric beam. The water layer formed on the surface will flow out from the surface once it reaches certain thickness or geometry, this will reduce the added mass coefficient. After spilling out, subsequent raindrop introduced onto the surface will fill the water layer up again which will then increase the added mass coefficient. Besides this, wind gust and water ripple played a role in preventing the formation of water layer on the surface.

In the numerical simulation, the median value of the added mass coefficients is used. The median added mass coefficient value is found to be 0.2685. The impact coefficient, which describes the post impact behaviour of a raindrop impact,

can be estimated by using Equation (3.33) as 0.2465. The added mass coefficient and impact coefficient are assumed to be constant in the raindrop impact energy harvesting simulation.

5.4 Verification of the theoretical model

The theoretical DSDs were generated using the two lognormal fitting parameters and the same number or raindrop as recorded in the experiment as presented in Section 5.2.2. The comparison between the experimental and theoretical DSDs are presented in Figure 5.8. Qualitative analysis on the DSD comparison graphs revealed that the accuracy of the theoretical DSD decreases when the raindrop diameter increases. Moreover, the theoretical results in bin1, bin2, and bin3 could not generate any raindrop beyond 5.75 mm. This is due to the low probability of obtaining raindrop diameter of more than 5.75 mm in low rain rate. Even so, the theoretical results were able to describe the DSDs obtained from actual rain experiments reasonably well.

Referring to the DSD graphs presented in Figure 5.8, the frequency of raindrop impact with higher diameter is higher as the rain rate increases. Furthermore, the average number of droplet increases as well when the rain rate increases. Therefore, higher absolute peak voltage and energy generation are expected as rain rate increases. According to the time series voltage graph obtained from the actual rain experiment, the voltage produced by the piezoelectric beam was not following the rain rate trend. To demonstrate the practicability of the

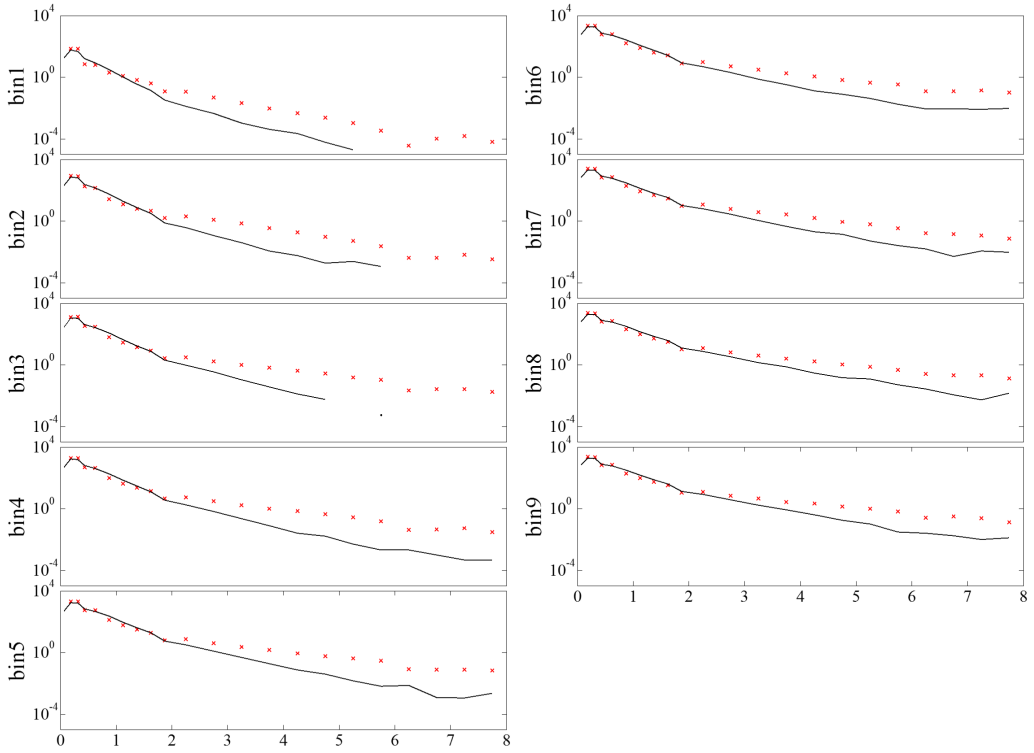


Figure 5.8: The theoretical and experimental DSD comparison graphs for different rain rate bins (y-axis: raindrop density ($\mathrm{m}^{-3}\mathrm{mm}^{-1}$; x-axis: raindrop diameter (mm).

theoretical model, the random generator function in Equation (5.1) is modified explicitly for the rain event discussed. The modified random generator function is presented as:

$$\overline{D}_n \sim \begin{cases} \mathscr{L}(\mu(R), \sigma(R)), & S1 : t < 360s \\ \mathscr{L}(\mu(R), \sigma(R)) | \overline{D}_n < 4.0mm, & S2 : 360s \leq t < 1080s \\ \mathscr{L}(\mu(R), \sigma(R)), & S3, S4 : t \geq 1080s \end{cases} \tag{5.9}$$

According to Figure 5.3(c), the average number of droplet is low during low rain rate. Therefore, the possibility of a raindrop with large diameter impacting the piezoelectric beam is extremely low. This phenomenon could not be replicated

by the theoretical DSD Lognormal Model, shown in Figure 5.8. As a result, it is impractical to modify the Lognormal DSD Model for S1.

The overall absolute peak voltage generated in S2 was relatively lower than of S3. This is explained by the raindrops that impacted the piezoelectric beam had lower diameter. As a result, the maximum raindrop diameter is limited as 4.0 mm in S2, shown in Equation 5.9. By doing so, the absolute peak voltage will be relatively lower despite having high rain rate. Whereas for S1, S3 and S4, the random generator function retains as Equation (5.1).

The experimental, theoretical, and modified theoretical voltage time response graphs are depicted in Figure 5.9. The theoretical voltage time response graph is obtained by performing numerical simulation using MATLAB, whilst the modified theoretical voltage time response graph is simulated using the modified random generator function presented in Equation 5.9. By comparing the experimental result to the theoretical result, the spikes of high absolute peak voltages were absent in the theoretical results in S1. Moreover, the overall absolute peak voltages in S2 were higher for the theoretical results, when compared to the experimental result. Hence, it is conjectured that the behaviour of the experimental voltage time response graph at S1 and S2 are irregular, where it does not follow the trend of rain rate as illustrated by the theoretical result.

In order to demonstrate the cause of irregularity in S2, the random generator function is modified as shown in Equation 5.9. It is demonstrated in Figure 5.9 that the overall absolute peak voltages for the modified theoretical result in S2 were lower than the theoretical result, which is in agreement with the

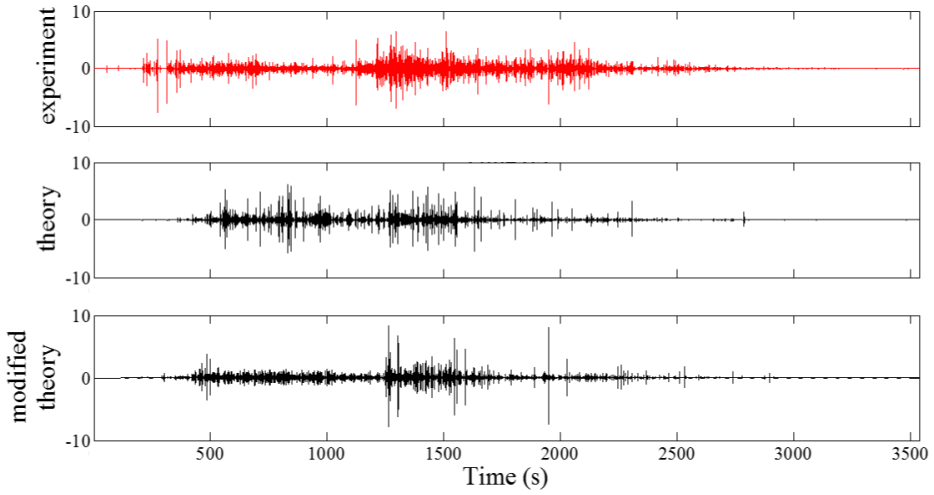


Figure 5.9: The experimental, theoretical, and modified theoretical voltage time response graphs, where the y-axes represent Voltage (V).

experimental result. On another note, both theoretical and modified theoretical voltage time response graphs did not exhibit high absolute peak voltage at S1. This is due to the impracticability of the Lognormal DSD Model to generate high raindrop diameter at low rain rate.

Energy accumulation graphs can be obtained by using Equation (3.39). The experimental, theoretical, and modified theoretical energy accumulation comparison graph are given in Figure 5.10. The total energy accumulated over a rain duration of 3540 s for the experiment result was 1564 μJ. A total of 10 theoretical and 10 modified theoretical energy accumulation graphs were generated to illustrate the variability of the model. The mean of the 10 energy accumulation graphs for the theoretical and modified theoretical results were calculated to be 2556 μJ and 1784 μJ respectively. The theoretical energy accumulation graphs had overpredicted the experimental energy accumulation with a percentage difference of 38.81 %. This is due to the lower absolute peak voltages in S2 in the

experimental result. By limiting the maximum raindrop diameter in the modified theoretical results in S2, it showed a good agreement with the experimental result, with a percentage difference of 12.33 %.

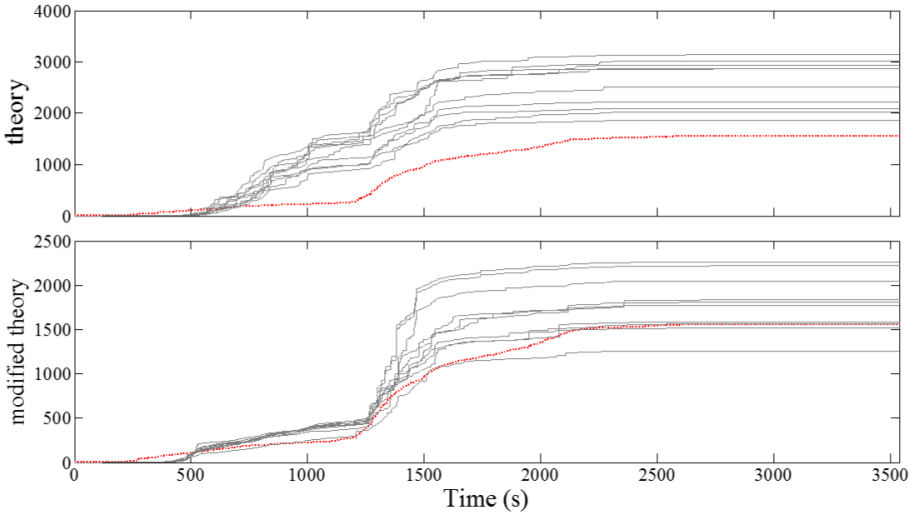


Figure 5.10: The experimental (in red dotted line), theoretical (10 samples in grey lines), and modified theoretical (10 samples in grey lines) energy accumulation comparison graphs, where the y-axis is the energy accumulation (μJ).

5.5 Implication of results

According to the theoretical model, higher energy production is to be expected during higher rain rate. However this is not always the case as shown by the experimental result as the voltage generated by the piezoelectric beam was not following the rain rate trend. This showed the unpredictability of an actual rain.

During rain, there will be period where the rain rate is low, especially during the beginning and towards the end of a rain. During this period, voltage generation will be very low and this will lead to low power generation. As a

result, the piezoelectric energy harvester could not power up devices directly. To solve this inconsistent power generation issue, an effective energy storage system has to be integrated into the energy harvesting system [84, 85].

There are several downsides for raindrop impact energy harvesting that need to be addressed [31]. When being compared to fossil fuels at their current cost, the energy generated by a raindrop impact energy harvester is less cost efficient. Furthermore, the power produced is very low and in some cases it could not be used directly. Moreover, the payback period is lengthy as the harvesting system only operational during rainy days.

On the bright side, the efficiency of the piezoelectric material will be improved as technology advances. As a result, the total recoverable energy from a raindrop impact energy harvester will be improved. Besides this, an array of raindrop impact energy harvester can be implemented [32] to increase the energy production of the whole system. A multifunctional hybrid energy harvesting system was introduced by Gambier et al. [86] that is able to harvest solar, thermal and vibration energy. Raindrop impact energy harvester can be integrated into such multifunctional hybrid energy harvesting system so that it could produce energy even during non-raining period.

5.6 Chapter conclusion

The artificial rain excitation model is modified into an actual rain excitation model in this chapter. The stochastic natures of an actual rain such as the variation of the rain rate and its effect on the rain DSD and average number of droplet are adapted into the theoretical model. The performance of a raindrop impact energy harvester was tested under actual rain condition. From the experimental results, a total energy of 1564 μJ was harvested for a rain duration of 3539 s.

The theoretical model is evaluated using experimental result obtained from actual rain. In the experiment result, even with high rain rate, the energy generated in S2 is lower in comparison to the energy generated in S3. As a result, the theoretical model could not correctly predict the energy harvested in S2. A modified theoretical model is introduced, which limits the maximum raindrop diameter in S2. The modified theoretical model shows an improvement in accuracy in estimating the total energy accumulation, with a percentage difference of 12.33 % when compared to the experimental result.

Chapter 6

Optimisation of the raindrop impact energy harvester

6.1 Introduction

Electrical energy generated by a piezoelectric beam must be converted into usable form (e.g. battery storage). A harvester circuit is integrated into the system for this purpose. To date, many harvesting circuits have been proposed and most of them considered harmonic excitation sources only [87–90]. In raindrop impact energy harvesting, a stochastic and impulsive excitation are expected. Therefore, the harvester circuit has to operate in such conditions. In this chapter, optimisation of a rectifier circuit is discussed. The forward voltage drop due to diodes in a conventional full bridge rectifier lowers the efficiency of a harvester circuit, especially in low voltage operations. To tackle this issue, a hybrid bridge

rectifier circuit is proposed. It is designed to exploit the switching between half bridge and full bridge modes via a microcontroller. By switching between these modes, the hybrid bridge rectifier circuit is able to perform better in both low and high voltage operations.

Literature surveys on mechanical and electrical optimisation for a piezoelectric energy harvester are conducted in Section 6.2. A harvester circuit which operates in random damped oscillation sources is rarely found in literature. The working fundamentals of the hybrid bridge rectifier is presented in Section 6.3. A RMS threshold voltage is introduced in Section 6.4 to determine the switching point for the hybrid bridge rectifier. The hybrid bridge rectifier was tested under actual rain and the results are discussed in Section 6.5.

6.2 Related work

The optimisation of a raindrop impact energy harvester using piezoelectric beam is discussed in this section. The performance of a piezoelectric beam energy harvester can be enhanced through mechanical means. The electrical energy generated by a piezoelectric beam is directly proportional to the strain induced on the transducer. A conventional piezoelectric beam, which is rectangular in shape, has higher strain at the clamp end of the beam and decreases linearly along the length of the structure when excited [91]. It was reported by Roundy [92] that a triangular beam can generate up to twice the power density of a conventional rectangular beam. A tapered piezoelectric beam design was found to

have a more uniformly distributed strain along the length of the beam compared to a conventional rectangular piezoelectric beam [89]. Numerical simulations successfully showed an improvement in performance by 69 %. The triangular or tapered beam structure is further optimised, demonstrated via FEA simulations [93]. The power output of the optimised shape increased approximately 25 % when compared with that of the conventional beam design. This has showed that the geometry of a conventional piezoelectric beam can be optimised to enhance energy generation.

Unfortunately, these studies considered base excitation only, which is not the case for a raindrop impact energy harvester. Furthermore, by decreasing the surface area of the piezoelectric beam, the likelihood for the raindrop to impact the beam decreases. Therefore, geometry optimisation requires further practical considerations in raindrop energy harvesting.

A combination of diaphragm and cantilever beams design was proposed by Chin-Hong et al. [39]. The piezoelectric beams were mounted around the diaphragm and will vibrate as raindrop impacts on the diaphragm. This has increased the raindrop impact likelihood as the diaphragm has a larger surface area. However, the efficiency of energy transfer from the diaphragm to the piezoelectric beams was not investigated and the design was not tested experimentally.

It was shown in Section 3.6.2 that when the water droplet impacts the harvester further from the clamp, more voltage will be generated. Moreover, the performance of the piezoelectric energy harvester is affected by the raindrop size. To tackle this issue, the raindrop energy harvester design can be modified into

a potential energy collection based generator. This is achieved by employing a water reservoir to collect water from rainfall and concentrates the impact position at the tip beam. A design that incorporates a water shelter that collects rain water, and a syringe to produce fixed water droplet size is proposed by Ong et al. [94]. With a drop distance of 0.2 m, which was measured from the tip of the syringe to the impact surface on the beam, the enhanced configuration gave an improvement of 6.84 % in an actual rain test. The performance of such design can be further improved by increasing the drop height of the fixed-size water droplet, however this would increase the size of the harvester.

In another design, the rain water is directed to a fluidic flow mechanism to drive a kinetic-to-electric transducer, such as a watermill or turbines [95]. Higher kinetic energy may be produced by providing a higher potential build-up. Although the energy generated by a potential energy collection based generator can be much higher than a direct impact based generator, the design of such harvester is bulky and it is challenging to be scaled down. In addition, the high kinetic energy of a raindrop due to its terminal velocity is lost when collected in a reservoir. To overcome this issue, higher drop height is required.

The performance of a piezoelectric energy harvester can also be enhanced electronically via harvester circuit. Harvester circuit is utilised in order to convert and store the electrical energy generated by the piezoelectric energy harvester. A typical harvester circuit topology comprises an AC-DC rectifier, a DC-DC converter and an energy storage buffer. An AC-DC rectifier is able to convert alternative current (AC) voltage from the piezoelectric energy harvester into

direct current (DC) voltage. The DC voltage output from the AC-DC rectifier is regulated before storing into an energy storage buffer (storage capacitor or battery).

According to the maximum power transfer theorem [96], in order for the maximum amount of power to be transferred from source to load, the impedances of the load and source have to be matched. Impedance is the combined effect of resistance, capacitive reactance, and inductive reactance. Piezoelectric element is known to have a large clamped capacitance [97]. In order to match the large clamped capacitance, inductor is normally used. The inductive reactance is dependent on the frequency. As the frequency of operation becomes too low, larger inductor is required, which becomes unfavourable for micro device designs [98]. Moreover, an inductor is unable to autonomously adapt to the changes in the operation environment. To tackle this issue, switching circuits were introduced. The performance of the switching circuits is optimised by using synchronous switches that correspond to the vibration of the piezoelectric element.

According to Liu and Vasic [98], switching circuit can be grouped into two categories. The first type locates the switches between the piezoelectric harvester and the rectifier. Examples are parallel-SSHI (Synchronised Switching Harvesting on an Inductor), and series-SSHI [87]. The techniques implemented for the switching circuit involve modifying the output voltage waveform of harvester when the mechanical displacement of the harvester reaches its maximum or minimum peaks. The second type of switching circuit positions the switches between the rectifier and storage buffer. Synchronised switching and discharging

to a storage capacitor through an inductor (SSDCI) [88] is an example for the second group of switching circuit. This method is able to increase the charging rate of the system by introducing an inductor and synchronised switches.

Conventional rectifiers are normally made of passive diodes such as p-n junction diodes or Schottky diodes. Diode's forward voltage drop is the amount of voltage dropped across a conducting diode. This is unfavourable when operating at low voltage as it could not overcome the diode's forward voltage drop. Besides this, the efficiency of a passive diode is low, and passive rectifier produces nonlinear load, which poses a challenge when designing a suitable converter [99].

To address this issue, active diodes had been introduced. Active diodes function by utilising transistor switches , which are controlled using comparators to sense the input AC voltage [100]. According to Liu et al. [101], an active diode rectifier is able to harvest maximum power up to five times when compared to passive diode rectifier.

However, such technique requires additional components, such as external comparators or bias networks, which increases the complexity and power loss of the circuitry [99]. To overcome this, a bridgeless boost rectifier is proposed [99]. The bridgeless boost rectifier consists of two types of DC-DC converter (boost converter and buck-boost converter). The two converters were designed to work together so that the boost converter is able to condition the positive half cycle of the AC voltage, while the buck-boost converter is able to condition the negative half cycle. Such design is able to convert 10 VAC to 30 VDC.

A low-power standalone adaptive harvesting circuit was introduced by Tabesh and Fréchette [90]. The harvesting circuit consists of a voltage doubler rectifier, a step down switching converter, and an analogue controller. It uses the piezoelectric voltage directly as a control signal compared to conventional circuits which rely on external sensors to provide feedback to the DC-DC converter. This has simplified the harvesting circuit as it does not require external sensors and digital controller to adjust the duty cycle of the switching converter. The proposed adaptive harvesting circuit has an efficiency of about 60 % for output power levels above 0.5 mW.

A two-stage energy conversion circuit designed for wind energy harvesting was proposed by Porcarelli et al. [102]. This design includes a hybrid voltage rectifier and a DC-DC buck boost converter. The hybrid voltage rectifier is able to switch between active and passive rectifier topologies. The harvesting circuit is managed by a microcontroller, which uses a 3.3 V supply. The authors proposed two strategies for the power management strategies: adaptive strategy, and smart strategy. The adaptive strategy allows the system to track the power generated by the microturbine and dynamically switches between the two rectifier topologies according to a threshold value. The implementation of this strategy has shown an increase in efficiency of 10 % and 30 % when compared to the conventional passive and active rectifier topologies respectively. As for the smart strategy, the system is able to predict power intake using regression analysis, so that an appropriate rectifier topology is selected. Results illustrated that by employing the power prediction algorithm, the system is able to yield 22% more

energy with respect to the previous method.

Full bridge and double voltage rectifier circuits were tested and optimised by varying the forward voltage of the diodes and the capacitance of the capacitor [103]. Experimental results revealed that the full bridge rectifier had higher efficiency compared to the double voltage rectifier when it was operating at lower voltage range.

Drawbacks of the abovementioned synchronised switch techniques include the relatively larger design size due to large inductor, and the power consumption of the synchronised switches and the control circuits. Moreover, most of the studies conducted were based on harmonic excitation, which make synchronisation possible. The control circuit design becomes complicated when the nature of the excitation is in damped oscillation, impulsive, and stochastic, which are the cases for raindrop impact energy harvesting. This has created a technology gap for harvester circuits in the case energy harvesting through damped oscillating and stochastic sources. This chapter focuses on the design and evaluation of a hybrid bridge rectifier that is suitable for raindrop impact energy harvesting. A brief experiment was carried out to demonstrate the viability of a hybrid bridge rectifier under actual rain.

6.3 Proposed optimisation method

Piezoelectric material is able to convert ambient mechanical vibration energy into usable electrical energy through direct piezoelectric effect. The electrical energy

generated by the piezoelectric material is usually in AC form and it could not be stored in a storage buffer such as rechargeable battery or storage capacitor, which require electrical energy in DC form. Hence, a rectifier, which is a AC-DC converter, is needed. However, the DC voltage obtained from the rectifier is normally low and sometimes can be discontinuous depending on the excitation source. In order to overcome this issue, a charging circuit (DC -DC converter) is implemented in a standard harvester circuit for piezoelectric energy harvesting. The charging circuit is often integrated with a control system, which will handle the discontinuity of DC voltage and also the impedance matching issue. The electrical energy is stored in a storage buffer (storage capacitor or battery), and it can be used for sensor or actuator depending on application. A block diagram of a standard harvester circuit topology is given in Figure 6.1.

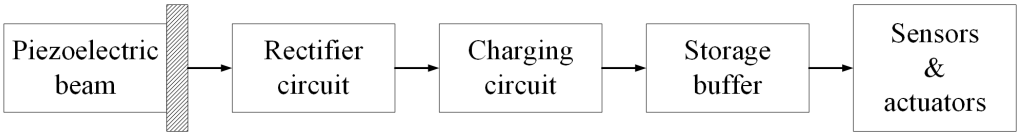


Figure 6.1: Block diagram of a standard harvester circuit topology.

This chapter focuses on the optimisation of the rectifier stage. The rectifier usually consists of active or passive diodes, which are discussed in the previous section. Passive diodes are selected for the study as active diodes require addition components [99], which will complicate the design. The passive diodes in a conventional rectifier circuit are arranged in either half bridge, full bridge, or double voltage configuration. According to [103], full bridge rectifier outperforms the double voltage rectifier in terms of efficiency in low voltage operating

range. Since the maximum peak voltage generated by the piezoelectric beam in this research is approximately less than 10 V, double voltage rectifier is not considered.

In this study, a bimorph piezoelectric beam, which has two layers of PZT material, is utilised. The two layers of the beam can be connected in either series or parallel. When it is connected in parallel, the current rating generated by the two PZT layers are added up, maintaining the same voltage rating; while connected in series, the voltage of the two PZT layers are added, keeping the same amperage rating. It is advantageous to have more electrical current to charge a capacitor or battery [21]. On the other hand, the voltage produced by the harvester might not be enough to overcome the diodes present in the rectifier circuit. Therefore, it is recommended to use series configuration when the excitation force is lower and parallel configuration when the excitation force is higher.

As mentioned previously, one of the disadvantages of using a passive diode is its forward voltage drop. The forward voltage drop of a diode (V_D) can be related to the current that passes through it (I_D) by using the diode equation, which is described by the diode current-voltage ($I - V$) characteristics curve [104], written as:

$$I_D = I_o\left(e^{\frac{V_D}{\eta V_T}-1}\right) \tag{6.1}$$

where, I_o is the reverse saturation current of the diode; V_T is the thermal voltage; and η is the ideality factor, which varies between 1 and 2. By taking $\eta = 1$, the

forward voltage drop of a diode can be written as a function of current using Equation (6.1) as:

$$V_D(I_D) = V_T ln\left(\frac{I_D + I_o}{I_o}\right) \tag{6.2}$$

From Equation (6.2), it is noted that the forward voltage drop increases as the current that passes through the diode increases. As a result, the current generated by the PZT layers will affect the performance of the rectifier circuit. The operation of the half bridge and full bridge rectifiers are presented in Figure 6.2.

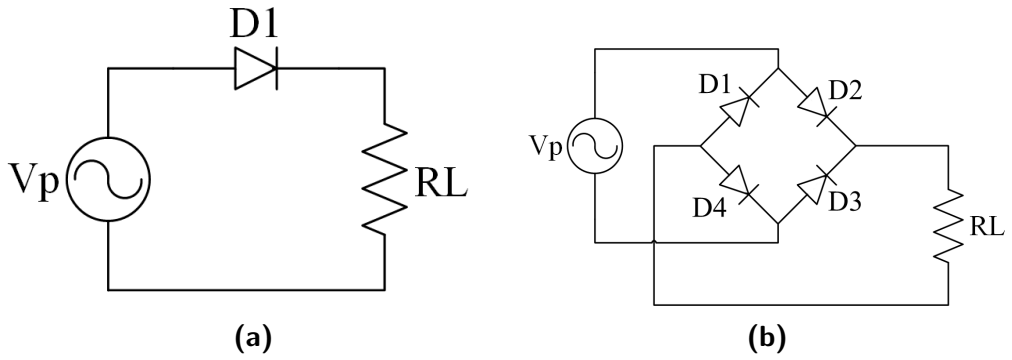


Figure 6.2: Schematic diagram of: (a) half bridge rectifier; (b) full bridge rectifier.

By applying Kirchoff's Voltage Law to the half bridge and full bridge rectifier circuits in Figure 6.2, the following expressions can be obtained:

Half bridge rectifier:

$$V_p > 0 \rightarrow V_{RL} = V_p - V_D(I_D)$$

$$V_p \leq 0 \rightarrow V_{RL} = 0 \tag{6.3}$$

Full bridge rectifier:

$$V_p > 0 \rightarrow V_{RL} = V_p - 2V_D(I_D)$$
$$V_p \leq 0 \rightarrow V_{RL} = -V_p - 2V_D(I_D) \tag{6.4}$$

where, V_p is the voltage generated by the piezoelectric beam; V_{RL} is the voltage measured across a load resistor, RL.

The output voltage graphs from the half bridge and full bridge rectifiers due to a sine wave input voltage are presented in Figure 6.3. Consider the half bridge rectifier, the negative cycle of the generated voltage is blocked by the diode. Hence at least 50 % of its efficiency is lost. Nonetheless, the half bridge rectifier only consists of a single forward voltage drop (V_D), hence it is preferred for low voltage operation, shown in Figure 6.3a. In the full bridge rectifier, the generated voltage from the harvester suffers from two forward voltage drop ($2V_D$) due to the operating diodes, shown in Figure 6.3a. As a result, the voltage generated by the piezoelectric layers has to be high enough in order to overcome the forward voltage drops due to the operating diodes.

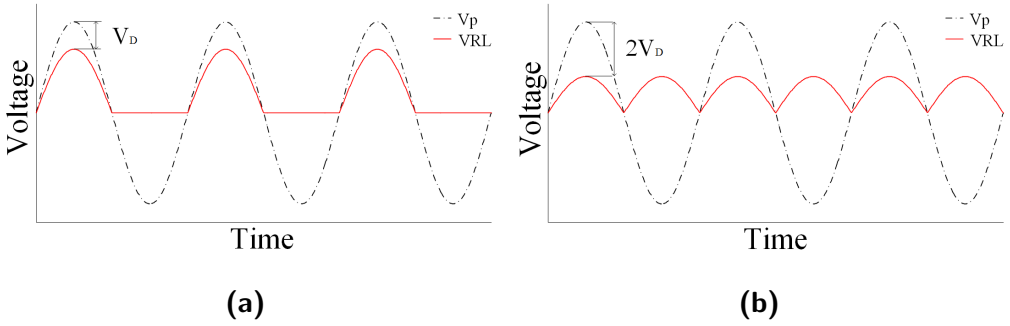


Figure 6.3: Input voltage from the piezoelectric harvester (V_p) and output voltage of the (a) half bridge rectifier, and (b) full bridge rectifier, measured across the load resistor (V_{RL}).

In this study, a hybrid bridge rectifier is proposed. The hybrid bridge rectifier operates by switching between full bridge and half bridge mode, depending on operating voltage conditions. The voltage measured across the load resistor is monitored by a microcontroller. RMS voltage is calculated for a fixed period of time by the microcontroller and the modes are switched accordingly. The control diagram of the hybrid bridge rectifier is illustrated in Figure 6.4.

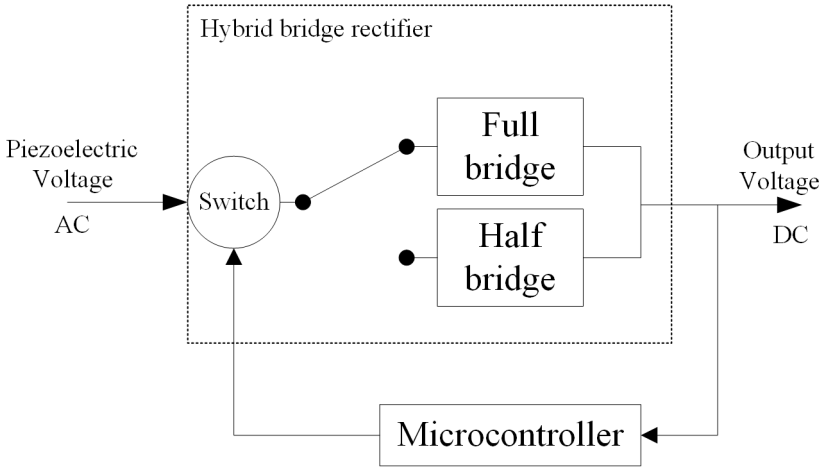


Figure 6.4: Control diagram of the hybrid bridge rectifier.

6.4 Design of the hybrid bridge rectifier

The design of a hybrid bridge rectifier is simple for fixed harmonic oscillation voltage output, such as a sine wave. The switch can be controlled by monitoring the voltage peak using comparators. However, for the case of random damped oscillation voltage output, which is the case for raindrop impact rain energy harvester, a better control regime has to be designed. For a damped oscillation, the

voltage will decay over time. Moreover, when the excitation source is stochastic in nature, it is hard to determine the successive optimal operation mode judging from the voltage peaks. In the proposed hybrid bridge rectifier, the bridge mode is switched by monitoring the RMS voltage for a fixed time frame using a microcontroller. By using RMS voltage as a switching indicator, the hybrid bridge rectifier is able to estimate the consecutive optimal operation mode.

In this section, the design of the proposed hybrid bridge rectifier is presented. Experiments were conducted to study the performance of the harvester circuit in four different configurations. The four configurations tested in this study are, full bridge rectifier with piezoelectric layers connected in series (SFB) and parallel (PFB), and half bridge rectifier with piezoelectric layers connected in series (SHB) and parallel (PHB). A threshold RMS voltage is established based on the experimental results, which determines the mode of operation for the hybrid bridge rectifier. The schematics design of the hybrid bridge rectifier is presented in Figure 6.5.

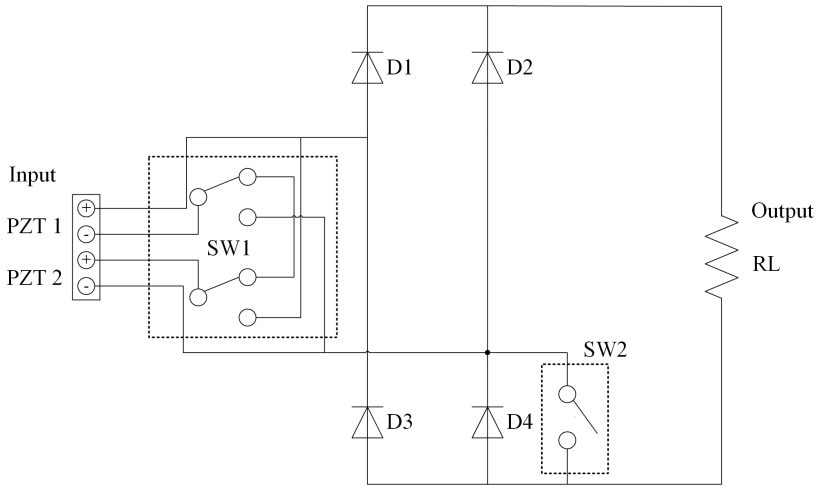


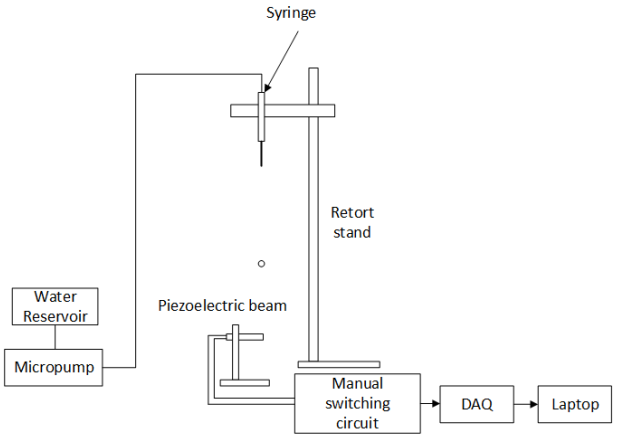
Figure 6.5: Schematics diagram of the manual switching circuit.

In order to produce the damped oscillation voltage output, the configuration in Chapter 3 is replicated. A peristaltic pump (Cole Palmer-Masterflex L/S series) is used to generate water droplet with consistent size. The water from a water reservoir is pumped to the silicon tube with a syringe needle. The syringe needle is positioned such that the water droplet could impact the tip of the piezoelectric beam. The voltage produced by the piezoelectric beam is conveyed to a manual switching circuit. The rectified voltage is then measured across a 15 kΩ load resistor using a data logger (NI-USB6008). The measured data is stored in a laptop for further analysis.

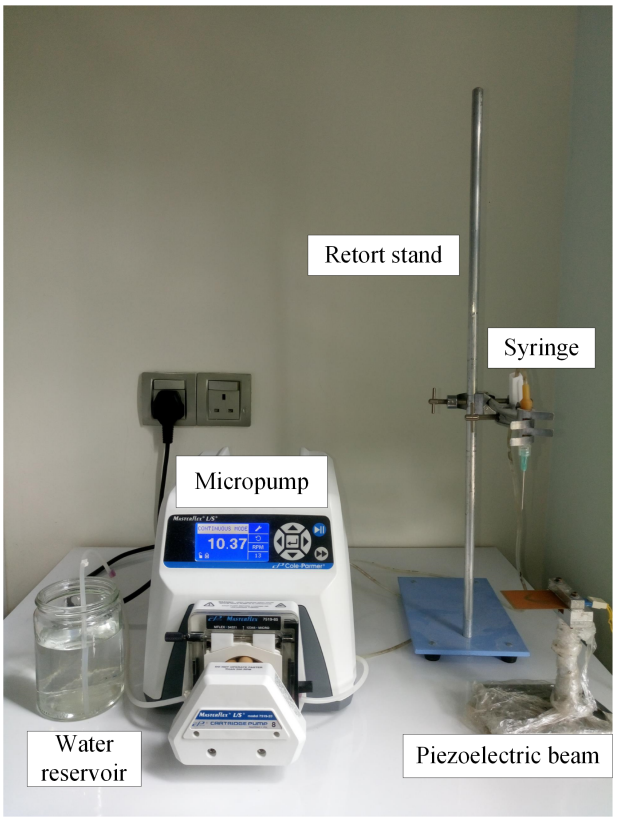
The syringe was positioned at the tip of the piezoelectric beam throughout the experiment. Combinations of different drop height and droplet diameter were used to generate various damped oscillation voltage outputs. The averages of 10 RMS voltage results are tabulated in Table 6.1 for each configuration mode. The average forces presented in Table 6.1 are calculated using Equation (3.27).

From Table 6.1, it was observed that the series connection of the piezoelectric layers performed better than the parallel connection. This was due to higher current generated by the piezoelectric layers when they were connected in parallel. According to the forward voltage drop of a diode, presented in Equation (6.2), the forward voltage drop of the diode will be higher when a higher current passes through it. As a result, higher voltage drop is expected.

By analysing the rectifier configurations when the piezoelectric layers are connected in series, the half bridge rectifier performs better in lower voltage



(a)



(b)

Figure 6.6: (a) Overview and (b) schematics diagram of the experimental setup.

region, compared to the full bridge rectifier. As shown in Table 6.1, by compromising the negative cycle of the input voltage and reducing the amount of diode forward voltage drop, it was found that the half bridge rectifier performs better

in low voltage operation. On the other hand, as the input voltage increases, the loss in RMS voltage by compromising the negative cycle was higher than the loss due to diode forward voltage drop. Hence, the full bridge configuration performs better at higher voltage operation.

Table 6.1: The root mean square voltage (average of 10 samples) of respective configurations when excited by single droplet impact of various average impact forces.

Droplet diameter (mm)	Drop height (m)	Average force (mN)	Root mean square voltage (mV)			
			PHB	PFB	SHB	SFB
2.96	0.020	1.8	2.290	0.577	**2.786**	1.445
2.96	0.030	2.7	3.881	1.385	**4.336**	3.325
2.96	0.040	3.6	7.324	3.165	**8.728**	6.474
2.96	0.055	4.9	10.506	4.751	**10.984**	9.497
2.96	0.078	6.9	18.632	9.622	**20.186**	18.179
2.96	0.100	8.8	21.568	13.189	24.666	**35.014**
2.96	0.250	20.4	50.480	35.090	48.452	**79.625**
4.36	0.110	21.1	107.550	92.110	109.840	**128.420**
4.36	0.130	24.9	184.970	139.270	172.960	**189.270**
4.36	0.180	34.1	189.010	160.770	198.210	**209.860**
4.36	0.900	152.1	582.070	511.843	512.410	**608.850**
4.36	1.770	261.8	687.170	631.670	603.720	**691.660**

The results of RMS voltage for SHB and SFB are presented in Figure 6.7. A zoom-in plot for lower voltage region is given in Figure 6.8. From Figure 6.8, the RMS voltage threshold can be estimated as 21 mV. The RMS voltage threshold will be used in the design of the hybrid rectifier control circuit.

For the final design of the hybrid rectifier circuit, the piezoelectric layers are connected in series, according to the results obtained from Table 6.1. The schematics of the hybrid rectifier circuit is presented in Figure 6.9. A full bridge rectifier is implemented by using four passive diodes (1N5817). The voltage are

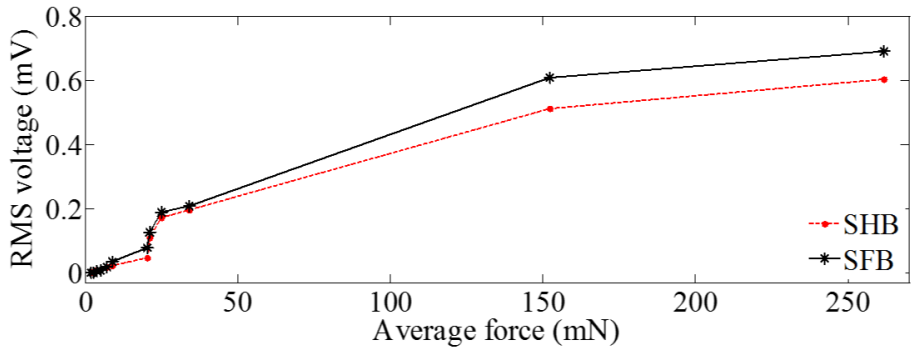


Figure 6.7: Scatter plots of RMS voltages for SHB and SFB.

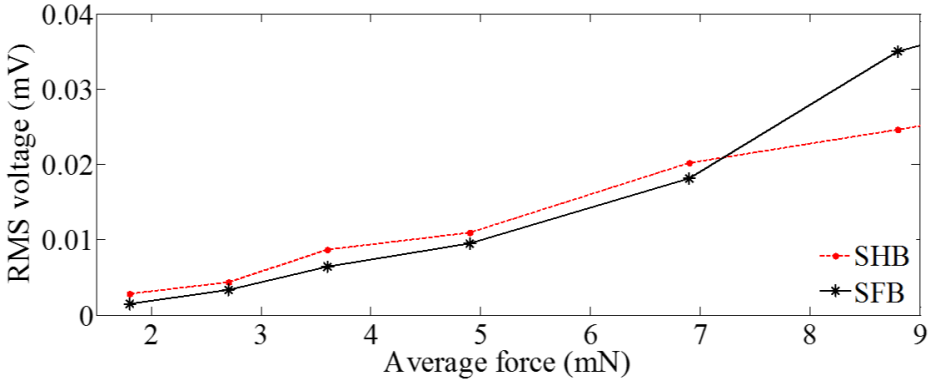


Figure 6.8: Zoom-in view of the RMS voltages for SHB and SFB.

measured across a load resistor (15 kΩ) by a microcontroller (Arduino UNO) via the 'in' pin illustrated in Figure 6.9. Meanwhile, the microcontroller monitors the RMS voltage generated by the piezoelectric harvester and switches according to the threshold voltage via the 'out' pin displayed in Figure 6.9. The circuit can be switched into half bridge mode by integrating a transistor switch (2N2222) that shorts diodes D2, D4. The transistor switch is controlled by the microcontroller via the 'out' pin shown in Figure 6.9.

In the implementation of the control circuit for the hybrid rectifier circuit, a microcontroller (Arduino UNO) is deployed. A flow chart of the developed control circuit is presented in Figure 6.10. At the start of the program, the

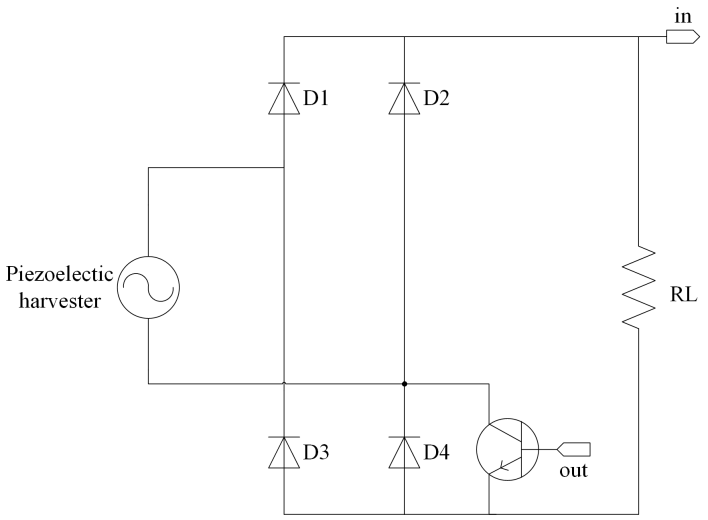


Figure 6.9: Schematics diagram of the hybrid bridge rectifier circuit.

switch is turned on by default. By doing so, it will configure the rectifier into half bridge configuration. This is because rain always starts with low intensity and results in very low RMS voltage output. The system monitors the RMS voltage every five seconds. As the RMS voltage exceeds the threshold voltage, the switch will be turned off, configuring the rectifier to full bridge mode.

6.5 Performance of the hybrid rectifier in actual rain

6.5.1 Methodology

The overview and schematics of the actual rain experiment are presented in Figure 6.11. A laser precipitation monitor sensor (Thies CLIMA-5.4110.10.000) is deployed to measure the rain rate. In the experimental setup, two commercial

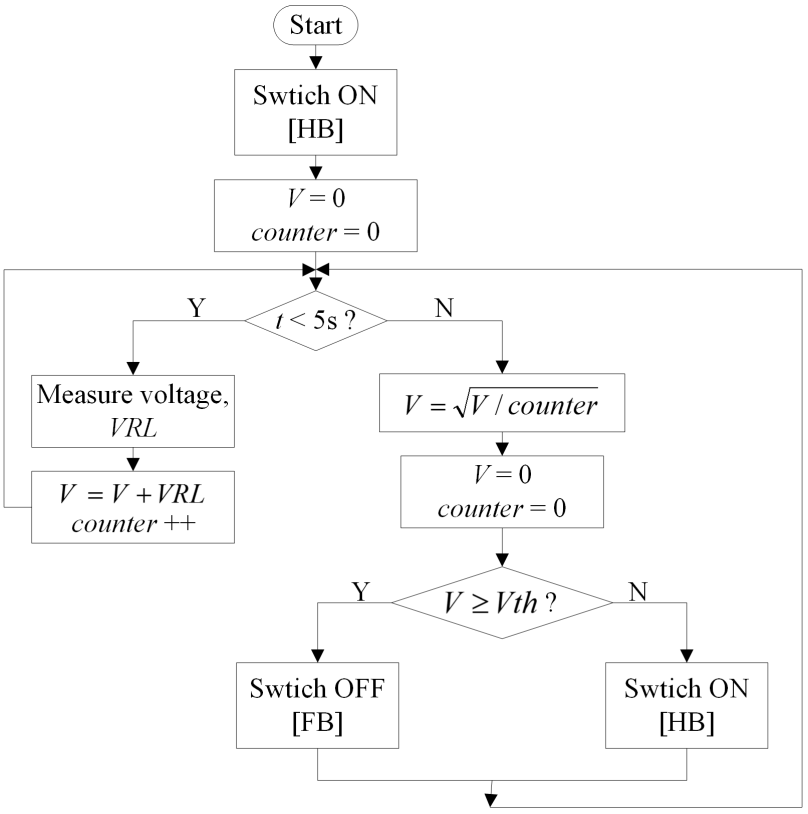


Figure 6.10: Flowchart of the control circuit for the hybrid bridge rectifier circuit.

bimorph piezoelectric beams (Mide-v25w) are used. The piezoelectric beams are clamped properly in a water-proof aluminium casing. The two piezoelectric beams are placed near to the laser precipitation monitor to minimise the discrepancy in raindrop distribution. The two piezoelectric beams were labelled as PZT-A and PZT-B, where they are being connected with a full bridge rectifier and a hybrid bridge rectifier circuit respectively. The voltage output from the two rectifier circuits are measured by a data logger (NI-USB6008), and it is connected to a laptop for data storage. The full bridge rectifier, hybrid bridge rectifier, and the data logger (NI - USB6008) are enclosed in a water-proof box.

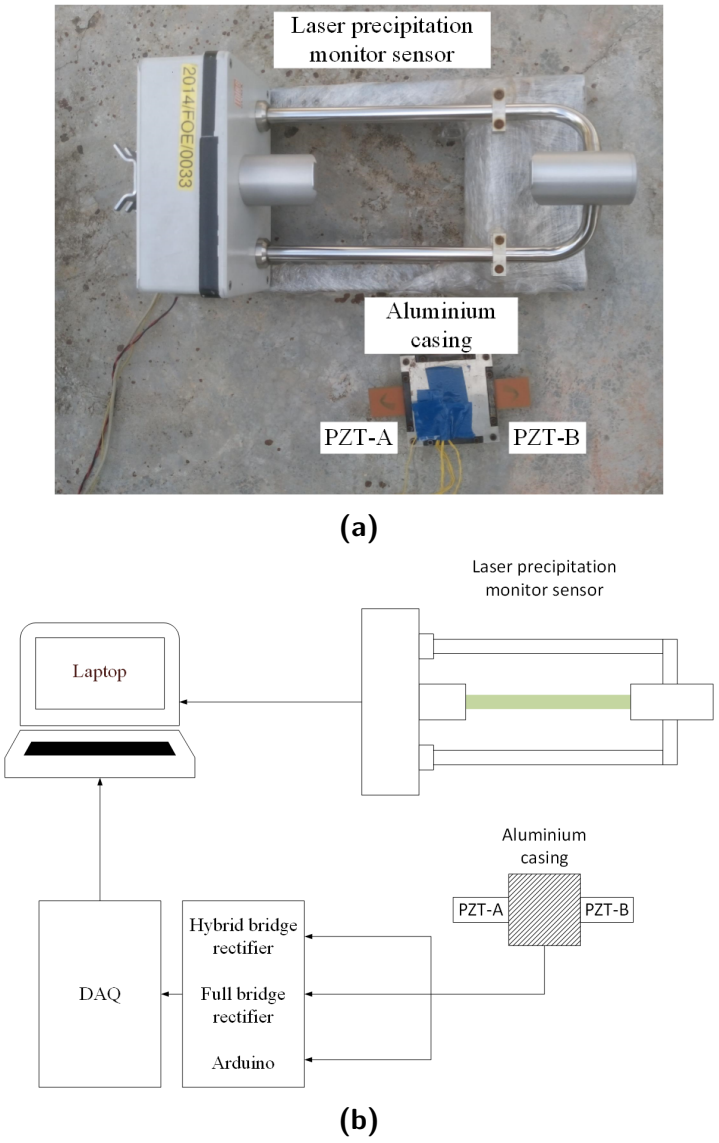


Figure 6.11: (a) Overview and (b) schematics of the actual rain experiment setup

6.5.2 Results and discussion

The total rain duration was 700 s. The rain rate graph is provided in Figure 6.12. The rain started off with low rain rate and increased gradually until it reached a maximum rain rate of 78.93 mm/hr at $t = 240$ s. After that, the rain rate decreased and started to dwindle.

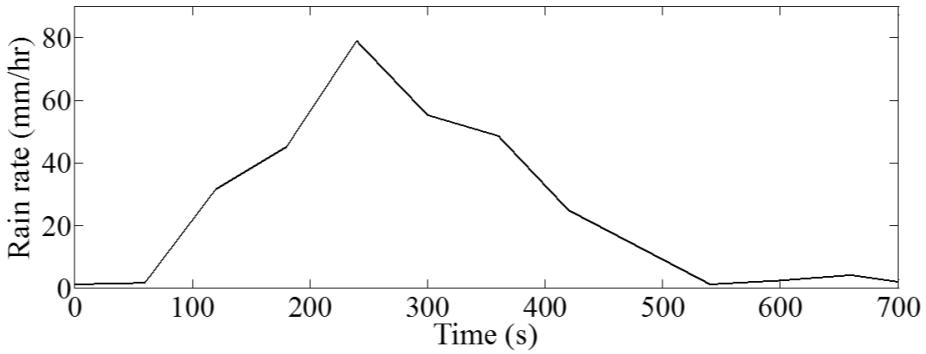


Figure 6.12: Rain rate graph with duration of 700 s.

The graphs of instantaneous voltage generated by the full bridge (PZT-A) and hybrid bridge (PZT-B) configurations are presented in Figure 6.13. The control switching of the hybrid rectifier is illustrated in Figure 6.13(b). The microcontroller switches every five seconds according to the RMS voltage measured. As the five-second RMS voltage dropped below the threshold voltage (21mV), the microcontroller will switch on the transistor, configuring the hybrid bridge rectifier into half bridge mode. The microcontroller will switch off the transistor if the five-second RMS voltage is higher than the threshold voltage, where in this case the hybrid bridge rectifier is in full bridge mode.

From Figure 6.13(b), it was noted that the hybrid bridge rectifier was operating at full bridge mode when the peak voltages were dense and having higher magnitude. This is in consensus to the design of the hybrid bridge rectifier, as it operates at full bridge mode when higher RMS voltage is detected, and operates at half bridge mode when lower RMS voltage is detected. The zoom-in view of the output voltage for the hybrid bridge rectifier in both half bridge and full bridge mode are presented in Figure 6.14. In half bridge mode, half cycle of the

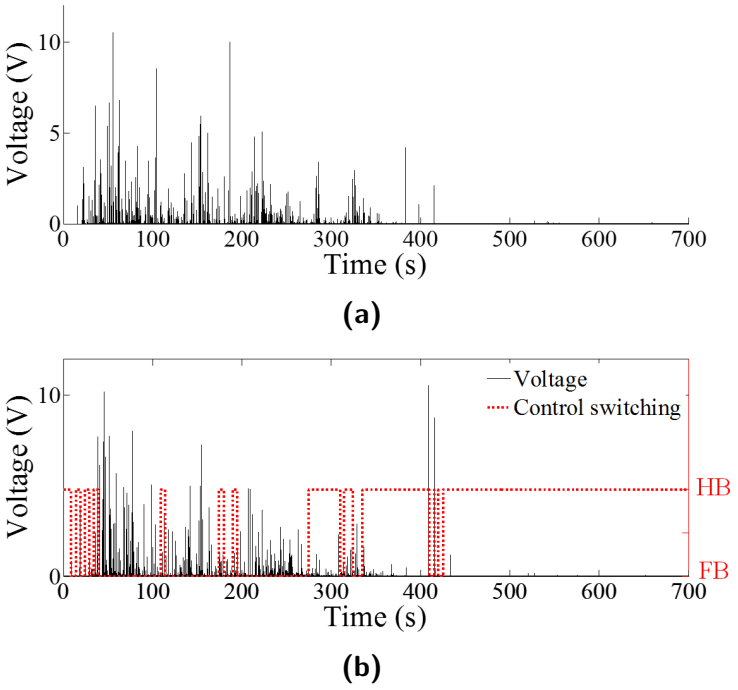


Figure 6.13: The voltage time response graphs for the: (a) full bridge rectifier (PZT-A); (b) hybrid bridge rectifier (PZT-B).

generated voltage is filtered by the diode; whereas in the full bridge mode, full cycle is present.

The energy generated by the full bridge and hybrid bridge rectifiers can be estimated by using Equation (3.39). The accumulation of energy produced by the two configurations are presented in Figure 6.15. The total energy accumulation of the hybrid bridge rectifier was found to be 56.97 μJ higher than the full bridge rectifier.

In order to further investigate the performance of the hybrid bridge rectifier, the energy accumulation graph for the two configurations are divided into S1 and S2, as shown in Figure 6.16. In S1, the hybrid bridge rectifier switched between full bridge and half bridge modes, according to the measured five-second RMS

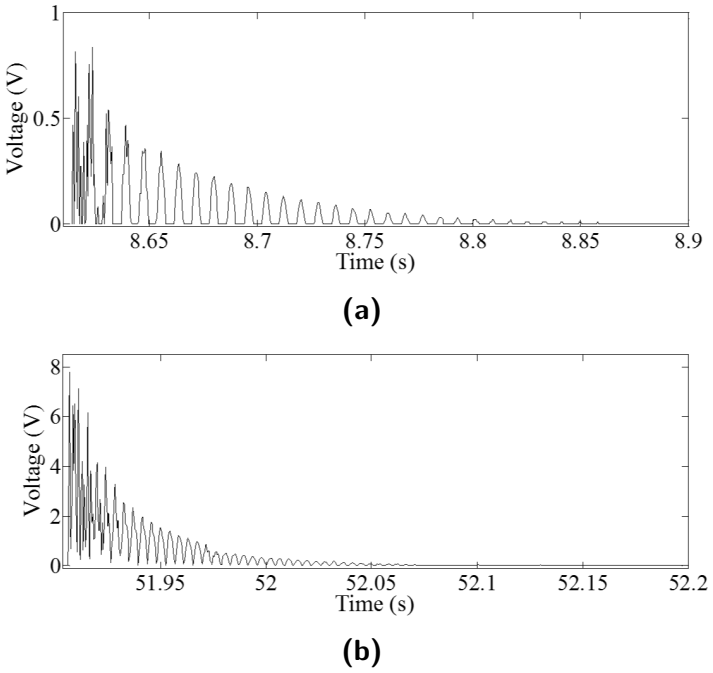


Figure 6.14: Zoom-in view on the voltage time response when the hybrid bridge rectifier is operating in: (a) half bridge mode; (b) full bridge mode.

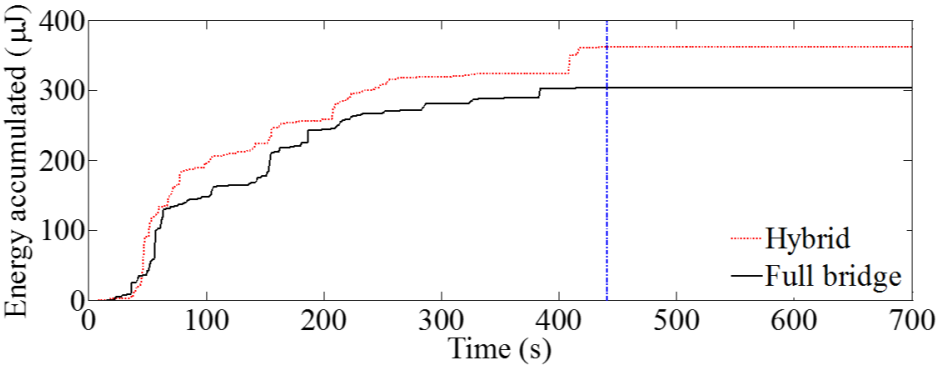


Figure 6.15: Energy accumulation graphs for the full bridge rectifier (PZT-A) and hybrid bridge rectifier (PZT-B). The graph is partitioned into S1 ($t < 440s$) and S2 ($440 \leq t \leq 700s$).

voltage, as illustrated in Figure 6.13(b). Whereas in S2, the measured five-second RMS voltage was low, resulting the hybrid bridge rectifier to be operating in half bridge mode.

In S1, the operating mode of the hybrid bridge rectifier switches frequently

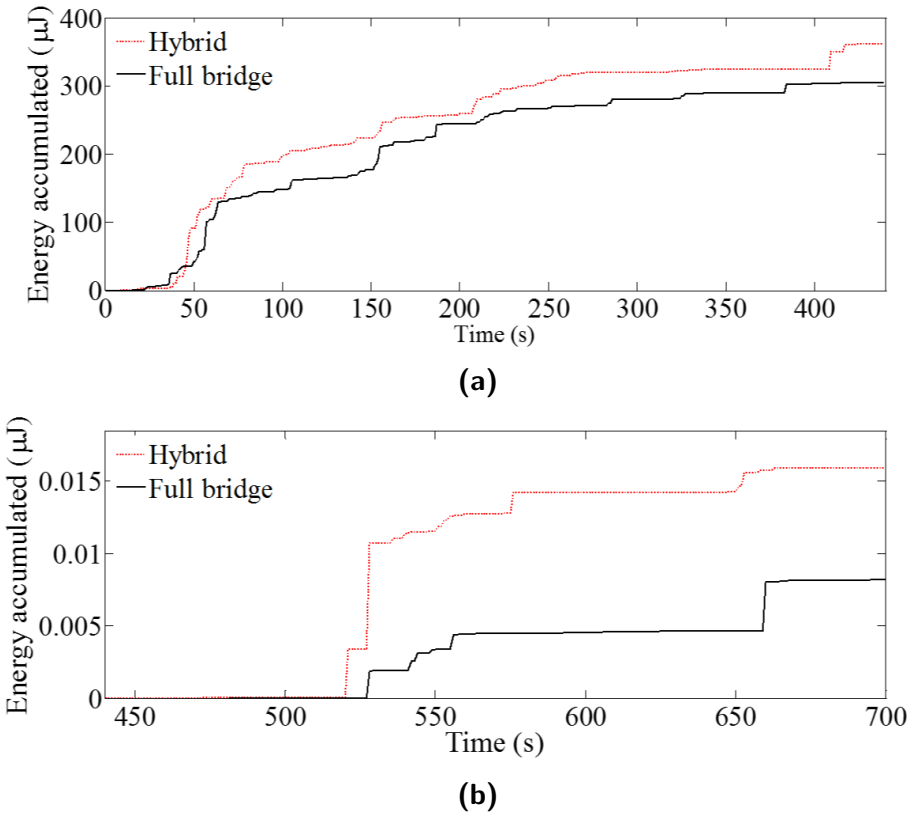


Figure 6.16: Energy accumulation graphs of the full bridge (PZT-A) andhybrid bridge (PZT-B) rectifiers of: (a)S1 ($t < 440$ s); (b) S2(440 s $\leq t \leq$ 700 s).

due to the rapid changes of the rain rate, which would affect the peak voltage generated by the piezoelectric beam. In S1, the hybrid bridge rectifier had harvested 18.71 % energy more when compared to the full bridge rectifier. Most of the energy harvested in this section was contributed when the hybrid bridge rectifier was operating in full bridge mode. Since most of the time the two harvester circuits were operating at the same mode, the discrepancy in the results demonstrated the energy generation variation due to the difference in location of the piezoelectric beam.

Towards the end of the rain, S2, the hybrid bridge rectifier was operating

in half bridge mode. At this region, the rain rate is low and the peak voltages generated by the piezoelectric beam for the two configurations were significantly lower compared to the peak voltages at S1. During low rain rate, the raindrop diameter is expected to be smaller compared to that in the high rain rate. As a result, the generated peak voltage is lower.

In low voltage region, the hybrid bridge rectifier outperformed the full bridge rectifier by 95.12 %. This can be explained by the lower forward voltage drop of the diodes in half bridge mode, which is discussed in Section 6.3. In the full bridge rectifier configuration, the low voltage produced by the piezoelectric beam could not overcome the diode forward voltage drop. Hence the efficiency of the full bridge rectifier dropped when it was operating at this region.

6.5.3 Implication of result

The hybrid bridge rectifier has demonstrated good potential in enhancing the performance of the harvester circuit in lower voltage region. The total energy accumulation of the full bridge rectifier in S1 and the hybrid bridge rectifier (which operated in half bridge mode) in S2 were 304.5 μJ and 0.01747 μJ respectively. Comparing the absolute value of the total energy accumulated in the two time sections, the introduction of the hybrid bridge rectifier may not seem justifiable. According to the control switching in Figure 6.13(b), the hybrid bridge rectifier operates at 62.79 % of the time throughout the experiment. This shows that for most of the time in rain, half bridge rectifier is a more suitable configuration. Since the energy requirement for a MEMS to operate is low, every

little energy harvested counts. This is especially true in raindrop impact energy harvesting application where rain does not occur all the time.

One of the drawbacks of the current hybrid bridge rectifier design is that it requires external voltage supply to power the microcontroller. To solve this issue, a microcontroller with low energy consumption or a comparator to compare RMS voltages can be utilised together with a low power standalone regime [90].

Furthermore, the control circuit requires to collect enough voltage reading before able to switch to the appropriate mode. This will cause a delay in the control circuit to determine the optimised mode and this will reduce the effectiveness of the overall system. The system can be further optimised by introducing a rain prediction algorithm to predict the successive operating mode instantly. During low rain rate, due to lower raindrop diameter, the RMS voltage produced in this time interval will be lower. At this instance, half bridge mode is preferred. Being able to predict the rain rate, the hybrid bridge rectifier could switch instantaneously instead of relying on the five second delay to determine the successive mode. One method to achieve this is by relating the RMS voltage to the intensity of rain. The RMS voltages recorded are monitored and the future RMS voltage could be estimated using regression analysis [102] so that the appropriate mode can be pre-determined.

Other than raindrop impact energy harvesting, the hybrid bridge rectifier concept can be integrated into other form of energy harvester which harvests energy from random impulsive vibrations in low voltage region.

6.6 Chapter conclusion

A hybrid bridge rectifier that is able to operate in low and high voltage region is proposed in this chapter. The hybrid bridge rectifier consists of a microcontroller that switches between half bridge and full bridge mode by comparing the five-second RMS voltage value to the RMS voltage threshold. The RMS voltage threshold was determined experimentally by considering various droplet impact magnitudes. In actual rain, the hybrid bridge rectifier performed 18.71 % better than the conventional full bridge rectifier. Further analysis on the actual rain experiment revealed that the half bridge mode produced 95.12 % more energy than in a full bridge rectifier during low rain rate. Despite having lower energy magnitude harvested during low rain rate as compared to the higher energy magnitude harvested in high rain rate, the increase in the energy production will be greater in the long run. The hybrid bridge rectifier can also be implemented in other types of energy harvester that operate at random impulsive vibration at low voltage region.Future works for this study include introducing a rain prediction algorithm so that the hybrid bridge rectifier could switch instantaneously, and converting the current circuit into a low power standalone circuit so that external power supply is not needed.

Chapter 7

Conclusions and future work

7.1 Conclusions and summary of findings

In this section, an overview of achievements and contributions of the work is presented. Throughout this research, theoretical models describing response of the raindrop impact energy harvester under different droplet excitation cases. This enables the analysis of the harvester in different given scenarios and provides accurate predictions without the need for expensive experimental setup. The theoretical models were validated via experimental results. Findings from previous chapters are summarised in this section.

Chapter 1:

A background study of piezoelectric energy harvesting is introduced in this chapter. The general motivation, aim and objectives are also provided in Chapter 1. Annual rainfall of a tropical climate country is high. As such, raindrop impact energy harvester is a feasible form of alternative energy source. Most of the studies conducted from the literature only considered single droplet impact, which could not fully describe the dynamics of a raindrop impact energy harvester using piezoelectric beam. Hence, this has became the main drive for the research.

Chapter 2:

The derivation of a piezoelectric beam model is presented in this chapter. The mode shape of a cantilever beam is derived by conducting modal analysis on the beam. Mass normalisation of the mode shape is performed by satisfying the orthogonality condition of the mode shape. The piezoelectric beam is described as a distributed parameter system. The piezoelectric beam model is realised by applying the constitutive equation of a linear piezoelectric material, Rayleigh-Ritz Theorem, and Lagranges equations for electromechanical systems. The theoretical piezoelectric beam model is able to estimate the voltage output response of the piezoelectric layers due to external force. The theoretical model is verified through experimental tests by using base excitation of four different G-forces. Good agreement was found between the experimental and theoretical results with a percentage difference range of 9.30 % to 25.45 %.

Chapter 3:

This chapter investigates the dynamics of single and multiple droplet impact on the piezoelectric beam. Water layer was found forming on the surface of the piezoelectric beam after successive water droplet. Such phenomenon was not found in the literature. The modal mass of the water layer formed is modelled by using an added mass coefficient. Loss of momentum of a water droplet impact was reported in literature, however further investigations were not carried out. In this Chapter, the loss of momentum of a water droplet impact is described by using an impact coefficient. The impact coefficient can be estimated by using the added mass coefficient, and the tip displacement measured using a laser vibrometer. The theoretical model is verified utilising experimental results, and good agreement is reported. An optimal operating region was found in the added mass coefficient intervals of $0.03423 < C_a < 0.4396$ and $0.03223 < C_a < 0.4698$ from the experimental and theoretical results respectively. Besides this, the single droplet impact model is extended into multiple droplet excitation model in this Chapter. The multiple droplet excitation model considers different drop periods and drop positions on the piezoelectric beam. In order to validate the theoretical model, three rain types (LSR, MSR, and HT) that correspond to different drop periods were considered. From the drop position study, it was found that when the water droplet impacts further form the clamp, more RMS voltage will be produced, this will increase the energy production. Rain rate study revealed that higher rain rate will reduce the drop period. This will give more droplet impacts, thus increasing the energy yield of the harvester.

Chapter 4:

This chapter further extends the multiple droplet excitation model to artificial rain excitation model. It is accomplished by introducing two random parameters into the excitation model, which are the water droplet size and droplet impact position. The water droplet size is modelled to be a random number based on two lognormal parameters. On the other hand, the droplet impact position is modelled as a uniformly distributed random number, which ranges from 0 to the maximum length span of the piezoelectric beam. The theoretical model was validated by testing the piezoelectric beam in laboratory condition using four artificial rains with fixed rain rate. Results revealed that when the rain rate increases, higher energy was accumulated over time. In the case of artificial rain, results had shown that the rain rate and power generated by the harvester exhibit positive correlation. When the rain rate of the artificial rain is 99 mm/hr, power of 0.207 μW and 0.251 μW were reported in the experimental and theoretical results respectively.

Chapter 5:

In this chapter, the artificial rain excitation model is modified into actual rain excitation model. Unlike artificial rain, the rain rate in actual rain varies over time. This will affect the rain DSD and average number of raindrop impact. As such, the Lognormal DSD model and average number of raindrop impact are modelled as a function of rain rate. The performance of a raindrop impact energy harvester was evaluated under actual rain condition. Experimental results demonstrated that a total energy of 1564 μJ was obtained for a rain duration

of 3539 s. From the actual rain experiment, a maximum instantaneous power of 3.75 mW was measured. This is higher than the maximum instantaneous power reported in literatures, which was 23 μW. The theoretical model is verified using experimental results. From the artificial rain study in Chapter 4 and the theoretical results given in this chapter, the rain rate was observed to be in positive correlation with the energy generation of the harvester. However this was not found in the experimental result. In order to demonstrate practicability of the developed model, the theoretical model is modified. This is achieved by limiting the maximum raindrop diameter at the period of time where the rain rate was not having positive correlation with the energy generation. The modified theoretical model successfully demonstrated improvement in accuracy, with a percentage difference of 12.33 % when compared to the experimental result.

Chapter 6:

A literature study on the optimisation of a piezoelectric beam energy harvester is presented in this Chapter. Most of the studies in literature considered base or harmonic excitation, which are not the case for a raindrop impact energy harvester. In a raindrop impact energy harvester, the excitation force is described as damped oscillation, impulsive, and stochastic. The main contribution of the Chapter is by proposing a harvester circuit that can be applied in raindrop impact energy harvester, known as a hybrid bridge rectifier. The hybrid bridge rectifier consists of a microcontroller that switches between half bridge and full bridge mode by comparing the five-second RMS voltage value to the RMS voltage threshold. As a result it is able to operate in low and high voltage region.

During low rain rate, experimental result revealed that the half bridge mode is able to yield 95.12 % more energy than in a conventional full bridge rectifier.

7.2 Future work

Based on the accomplishments in this project, recommendations on future work are outlined in this section. At this stage, raindrop impact energy harvester is not a propitious form of alternative energy harvester. This is due to its lower power production when compared to other form of energy harvesters. Moreover, raindrop impact energy harvester can only operates during rainy days. As a result, extensive research and development have to be conducted in order to improve its performance and cost effectiveness. Directions such as introducing array of raindrop impact energy harvester [32] and a multifunctional hybrid energy harvesting system, which is able to harvest solar, thermal, and vibration energy [86] demonstrate good future prospect in raindrop impact energy harvesting.

In the time coarse study on the accumulation of water droplet on the piezoelectric beam highlighted in Chapter 3, an optimal operating region was observed. By correlating the camera images given in Figure 3.8, the optimal operating region happens before the water layer reaches the width ends of the piezoelectric beam. Therefore, it is advantageous for the piezoelectric beam to be operating at that region regardless on the water accumulation progress. To accomplish this, surface treatment for the piezoelectric beam can be considered.

Besides this, the drop position study conducted in Chapter 3 revealed that higher RMS voltage was observed when the water droplet impact further from the clamp of the piezoelectric beam. By designing a rain water collecting regime, the rain water can be funnelled and impact on the tip of the piezoelectric beam. Initial phase of this work had been carried out by [94]. In order to produce higher energy, the drop height of the funnelled water droplet has to be higher. Moreover, the inlet of the reservoir should be bigger, and the size of the reservoir can be increase so that more rain water is collected to insure continuous supply of water droplet impact. However, such design compromises the size of the energy harvester, making it impractical in certain applications where space is a concern. As a result, the trade off between the harvester size and energy generation of the harvester has to be investigated. The hybrid bridge rectifier proposed in Chapter 6 is applicable in other types of energy harvester that function at random impulsive vibration in low voltage region. To increase the practicality of the hybrid bridge rectifier, extensive works have to be done so that it could be enhanced into a low-power standalone circuit so that external power supply is not needed. In the application of raindrop impact energy harvesting, rain prediction algorithm can be developed so that the rectifier could switch instantaneously without the need of collecting RMS voltages.

Bibliography

[1] J. Ouellette. Mems: Mega promise for micro devices. *The Industrial Physicist*, 2:9–12, 1996.

[2] M. Staples, K. Daniel, M.J. Cima, and R. Langer. Application of micro-and nano-electromechanical devices to drug delivery. *Pharmaceutical research*, 23(5):847–863, 2006.

[3] N.E. Dutoit, B.L. Wardle, and S.G. Kim. Design considerations for mems-scale piezoelectric mechanical vibration energy harvesters. *Integrated Ferroelectrics*, 71(1):121–160, 2005.

[4] K.A. Cook-Chennault, N. Thambi, and A.M. Sastry. Powering mems portable devicesa review of non-regenerative and regenerative power supply systems with special emphasis on piezoelectric energy harvesting systems. *Smart Materials and Structures*, 17(4):043001, 2008.

[5] J. Curie and P. Curie. Development by pressure of polar electricity in hemihedral crystals with inclined faces. *Bull. soc. min. de France*, 3:90, 1880.

[6] S. Meninger, J.O Mur-Miranda, R. Amirtharajah, A. Chandrakasan, and J.H. Lang. Vibration-to-electric energy conversion. *IEEE Transactions on Very Large Scale Integration (VLSI) Systems*, 9(1):64–76, 2001.

[7] S.P. Beeby, R.N. Torah, M.J. Tudor, P. Glynne-Jones, T. O'Donnell, C.R. Saha, and S. Roy. A micro electromagnetic generator for vibration energy harvesting. *Journal of Micromechanics and microengineering*, 17(7):1257, 2007.

[8] K.A. Cook-Chennault, N. Thambi, M.A. Bitetto, and E.B. Hameyie. Piezoelectric energy harvesting a green and clean alternative for sustained power production. *Bulletin of Science, Technology & Society*, 28(6):496–509, 2008.

[9] S. Boisseau, G. Despesse, and B.A. Seddik. Electrostatic conversion for vibration energy harvesting. *arXiv preprint arXiv:1210.5191*, 2012.

[10] D. Zhu. *Vibration energy harvesting: machinery vibration, human movement and flow induced vibration*. InTech, 2011.

[11] H.G. Lippman. Sur le principe de la conservation de lelectricite ou second principe de la theories des phenomenes electriques. *Comptes Rendus de lAcadamie des Sciences Paris*, 29:1049, 1881.

[12] N. Araki, H. Ohsato, K. Kakimoto, T. Kuribayashi, Y. Kudoh, and H. Morikoshi. Origin of piezoelectricity for langasite a 3 ga 5 sio 14 (a= la and nd) under high pressure. *Journal of the European Ceramic Society*, 27(13):4099–4102, 2007.

[13] L.P. Inc. Mono crystalline quartz - the piezoelectric effect. Report, Laptech Precision Inc, 2011.

[14] K.S. Ramadan, D. Sameoto, and S. Evoy. A review of piezoelectric polymers as functional materials for electromechanical transducers. *Smart Materials and Structures*, 23(3):033001, 2014.

[15] I. Patel, E. Siores, and T. Shah. Utilisation of smart polymers and ceramic based piezoelectric materials for scavenging wasted energy. *Sensors and Actuators A: Physical*, 159(2):213–218, 2010.

[16] Ltd APC International. *Piezoelectric ceramics: principles and applications*. APC International, 2002.

[17] A. Meitzler, H.F. Tiersten, A.W. Warner, D. Berlincourt, G.A. Couqin, and F.S. Welsh III. IEEE standard on piezoelectricity, 1988.

[18] X.D. Xie and Q. Wang. Energy harvesting from a vehicle suspension system. *Energy*, 86:385–392, 2015.

[19] H. Xiong and L. Wang. Piezoelectric energy harvester for public roadway: On-site installation and evaluation. *Applied Energy*, 174:101–107, 2016.

[20] M. Guan and W.H. Liao. Design and analysis of a piezoelectric energy harvester for rotational motion system. *Energy Conversion and Management*, 111:239–244, 2016.

[21] S.R. Anton and D.J. Inman. Vibration energy harvesting for unmanned aerial vehicles. In *The 15th International Symposium on: Smart Structures*

and Materials & Nondestructive Evaluation and Health Monitoring, page 692824. International Society for Optics and Photonics, 2008.

[22] X.D. Xie, Q. Wang, and S.J. Wang. Energy harvesting from high-rise buildings by a piezoelectric harvester device. *Energy*, 93:1345–1352, 2015.

[23] J. Feenstra, J. Granstrom, and H. Sodano. Energy harvesting through a backpack employing a mechanically amplified piezoelectric stack. *Mechanical Systems and Signal Processing*, 22(3):721–734, 2008.

[24] A. Delnavaz and J. Voix. Energy harvesting for in-ear devices using ear canal dynamic motion. *IEEE Transactions on Industrial Electronics*, 61 (1):583–590, 2014.

[25] S. Ju and C.H. Ji. Indirect impact based piezoelectric energy harvester for low frequency vibration. In *2015 Transducers-2015 18th International Conference on Solid-State Sensors, Actuators and Microsystems (TRANSDUCERS)*, pages 1913–1916. IEEE, 2015.

[26] J. Sirohi and R. Mahadik. Piezoelectric wind energy harvester for low-power sensors. *Journal of Intelligent Material Systems and Structures*, 22 (18):2215–2228, 2011.

[27] H.J. Jung, Y. Song, S.K. Hong, C.H. Yang, S.J. Hwang, S.Y. Jeong, and T.H. Sung. Design and optimization of piezoelectric impact-based micro wind energy harvester for wireless sensor network. *Sensors and Actuators A: Physical*, 222:314–321, 2015.

[28] X.D. Xie, Q. Wang, and N. Wu. Energy harvesting from transverse ocean waves by a piezoelectric plate. *International Journal of Engineering Science*, 81:41–48, 2014.

[29] N. Wu, Q. Wang, and X.D. Xie. Ocean wave energy harvesting with a piezoelectric coupled buoy structure. *Applied Ocean Research*, 50:110–118, 2015.

[30] B.K. Biswas and B.H. Mandal. Construction and evaluation of rainwater harvesting system for domestic use in a remote and rural area of khulna, bangladesh. *International Scholarly Research Notices*, 2014, 2014.

[31] A. Tinaikar. Harvesting energy from rainfall. *International Journal of Renewable and Sustainable Energy*, 2(3):130–132, 2013.

[32] M.A. Ilyas and J. Swingler. Piezoelectric energy harvesting from raindrop impacts. *Energy*, 90:796–806, 2015.

[33] R. Guigon, J.J. Chaillout, T. Jager, and G. Despesse. Harvesting raindrop energy: theory. *Smart Materials and Structures*, 17(1):015038, 2008.

[34] R. Guigon, J.J. Chaillout, T. Jager, and G. Despesse. Harvesting raindrop energy: experimental study. *Smart Materials and Structures*, 17(1):015039, 2008.

[35] D. Vatansever, R.L. Hadimani, T. Shah, and E. Siores. An investigation of energy harvesting from renewable sources with pvdf and pzt. *Smart Materials and Structures*, 20(5):055019, 2011.

[36] F. Viola, P. Romano, R. Miceli, G. Acciari, and C. Spataro. Piezoelectric model of rainfall energy harvester. In *Ecological Vehicles and Renewable Energies (EVER), 2014 Ninth International Conference on*, pages 1–7. IEEE, 2014.

[37] M. Al Ahmad. Piezoelectric water drop energy harvesting. *Journal of electronic materials*, 43(2):452–458, 2014.

[38] K.C.R. Perera, B.G. Sampath, V.P.C. Dassanayake, and B.M. Hapuwatte. Harvesting of kinetic energy of the raindrops. *World Academy of Science, Engineering and Technology, International Journal of Mathematical, Computational, Physical, Electrical and Computer Engineering*, 8(2):325–330, 2014.

[39] W. Chin-Hong, Z. Dahari, A.A. Manaf, O. Sidek, M.A. Miskam, and J.J. Mohamed. Simulation of piezoelectric raindrop energy harvester. In *TENCON Spring Conference, 2013 IEEE*, pages 465–469. IEEE, 2013.

[40] C.H. Wong, Z. Dahari, A.A. Manaf, and M.A. Miskam. Harvesting raindrop energy with piezoelectrics: a review. *Journal of Electronic Materials*, 44(1):13–21, 2015.

[41] H.Y. Lam, L. Luini, J. Din, C. Capsoni, and A.D. Panagopoulos. Investigation of rain attenuation in equatorial kuala lumpur. *IEEE Antennas and Wireless Propagation Letters*, 11:1002–1005, 2012.

[42] T. Mao, D.C.S. Kuhn, and H. Tran. Spread and rebound of liquid droplets upon impact on flat surfaces. *AIChE Journal*, 43(9):2169–2179, 1997.

[43] K. Range and F. Feuillebois. Influence of surface roughness on liquid drop impact. *Journal of Colloid and Interface Science*, 203(1):16–30, 1998.

[44] S. Mangili, C. Antonini, M. Marengo, and A. Amirfazli. Understanding the drop impact phenomenon on soft pdms substrates. *Soft Matter*, 8(39): 10045–10054, 2012.

[45] A. Erturk and D.J. Inman. *Piezoelectric energy harvesting*. John Wiley & Sons, 2011.

[46] L. Meirovitch. *Fundamentals of vibrations*. Waveland Press, 2010.

[47] A. Preumont. *Twelve lectures on structural dynamics*, volume 198. Springer, 2013.

[48] M. López Aenlle, R. Brincker, and Alfonso C. Fernández C. Some methods to determine scaled mode shapes in natural input modal analysis. 2005.

[49] A. Erturk and D.J. Inman. On mechanical modeling of cantilevered piezoelectric vibration energy harvesters. *Journal of Intelligent Material Systems and Structures*, 19(11):1311–1325, 2008.

[50] S. Roundy, P.K. Wright, and J. Rabaey. A study of low level vibrations as a power source for wireless sensor nodes. *Computer communications*, 26 (11):1131–1144, 2003.

[51] A. Erturk and D.J. Inman. Issues in mathematical modeling of piezoelectric energy harvesters. *Smart Materials and Structures*, 17(6):065016, 2008.

[52] N.W. Hagood, W.H. Chung, and A. Von Flotow. Modelling of piezoelectric actuator dynamics for active structural control. *Journal of Intelligent Material Systems and Structures*, 1(3):327–354, 1990.

[53] S.H. Crandall. *Dynamics of mechanical and electromechanical systems*. McGraw-Hill, 1968.

[54] H.A. Sodano, G. Park, and D.J. Inman. Estimation of electric charge output for piezoelectric energy harvesting. *Strain*, 40(2):49–58, 2004.

[55] N.E. DuToit and B.L. Wardle. Experimental verification of models for microfabricated piezoelectric vibration energy harvesters. *AIAA journal*, 45(5):1126–1137, 2007.

[56] D.J. Leo. *Engineering analysis of smart material systems*. John Wiley & Sons, 2007.

[57] C.H. Lamarque, S. Pernot, and A. Cuer. Damping identification in multi-degree-of-freedom systems via a wavelet-logarithmic decrementpart 1: theory. *Journal of Sound and Vibration*, 235(3):361–374, 2000.

[58] F. Goldschmidtboeing and P. Woias. Characterization of different beam shapes for piezoelectric energy harvesting. *Journal of micromechanics and microengineering*, 18(10):104013, 2008.

[59] A. Erturk and D.J. Inman. Broadband piezoelectric power generation on high-energy orbits of the bistable duffing oscillator with electromechanical coupling. *Journal of Sound and Vibration*, 330(10):2339–2353, 2011.

[60] S.E. Jo, M.S. Kim, and Y.J. Kim. Passive-self-tunable vibrational energy harvester. In *2011 16th International Solid-State Sensors, Actuators and Microsystems Conference*, pages 691–694. IEEE, 2011.

[61] S. Asadi and H. Panahi. A numerical study of a droplet impinging on a liquid surface. *World Academy of Science, Engineering and Technology*, 5 (7):613–617, 2011.

[62] J. Liu, H. Vu, S.S. Yoon, R.A. Jepsen, and G. Aguilar. Splashing phenomena during liquid droplet impact. *Atomization and Sprays*, 20(4):297–310, 2010.

[63] A.S. Grinspan and R. Gnanamoorthy. Impact force of low velocity liquid droplets measured using piezoelectric pvdf film. *Colloids and Surfaces A: Physicochemical and Engineering Aspects*, 356(1):162–168, 2010.

[64] J. Kongthon, B. McKay, D. Iamratanakul, K. Oh, J.H. Chung, J. Riley, and S. Devasia. Added-mass effect in modeling of cilia-based devices for microfluidic systems. *Journal of Vibration and Acoustics*, 132(2):024501, 2010.

[65] D. Sedlar, Ž. Lozina, and D. Vučina. Experimental investigation of the added mass of the cantilever beam partially submerged in water. *Tehnički vjesnik*, 18(4):589–594, 2011.

[66] A.C. Imeson, R. Vis, and E. De Water. The measurement of water-drop impact forces with a piezo-electric transducer. *Catena*, 8(1):83–96, 1981.

[67] C Mundo, C. Tropea, and M. Sommerfeld. Numerical and experimental investigation of spray characteristics in the vicinity of a rigid wall. *Experimental thermal and fluid science*, 15(3):228–237, 1997.

[68] V.K. Wong, J.H. Ho, and E.H. Yap. Dynamics of a piezoelectric beam subjected to water droplet impact with water layer formed on the surface. *Journal of Intelligent Material Systems and Structures*, 26(16):2170–2180, 2015.

[69] A. Covert and P. Jordan. A portable rainfall simulator: techniques for understanding the effects of rainfall on soil erodibility. *Watershed Management Bulletin*, 13(1), 2009.

[70] J. Blanquies, M. Scharff, and B. Hallock. The design and construction of a rainfall simulator. 2003.

[71] P.R. Commandeur, E.F. Wass, et al. Rainfall simulation, soil infiltration, and surface erosion on skidroad surfaces-Nelson Forest Region. *B.C. Min. Forests, Research Branch, Canada - BC FRDA Report*, 1994.

[72] S. Das, A. Maitra, and A.K. Shukla. Rain attenuation modeling in the 10-100 ghz frequency using drop size distributions for different climatic zones in tropical india. *Progress In Electromagnetics Research B*, 25:211–224, 2010.

[73] J. Ostrometzky, R. Raich, A. Eshel, and H. Messer. Calibration of the attenuation-rain rate power-law parameters using measurements from commercial microwave networks. In *2016 IEEE International Conference*

on Acoustics, Speech and Signal Processing (ICASSP), pages 3736–3740. IEEE, 2016.

[74] P. Panchal and R. Joshi. Performance analysis and simulation of rain attenuation models at 12–40 ghz band for an earth space path over indian cities. *Procedia Computer Science*, 79:801–808, 2016.

[75] S. Patade, S. Shete, N. Malap, G. Kulkarni, and T.V. Prabha. Observational and simulated cloud microphysical features of rain formation in the mixed phase clouds observed during caipeex. *Atmospheric Research*, 169: 32–45, 2016.

[76] A. Vidyarthi, B.S. Jassal, R. Gowri, and A.K. Shukla. Comparison between empirical lognormal and gamma rain drop-size distribution models for indian region. In *Asia-Pacific Microwave Conference 2011*, pages 1686–1689. IEEE, 2011.

[77] J.S. Marshall and W.Mc K. Palmer. The distribution of raindrops with size. *Journal of meteorology*, 5(4):165–166, 1948.

[78] J. Joss and E.G. Gori. Shapes of raindrop size distributions. *Journal of Applied Meteorology*, 17(7):1054–1061, 1978.

[79] C.W. Ulbrich. Natural variations in the analytical form of the raindrop size distribution. *Journal of Climate and Applied Meteorology*, 22(10): 1764–1775, 1983.

[80] G.O. Ajayi and R.L. Olsen. Modeling of a tropical raindrop size distribution for microwave and millimeter wave applications. *Radio Science*, 20 (2):193–202, 1985.

[81] K.I. Timothy, J.T. Ong, and E.B.L. Choo. Raindrop size distribution using method of moments for terrestrial and satellite communication applications in singapore. *IEEE Transactions on Antennas and Propagation*, 50(10): 1420–1424, 2002.

[82] O. Adetan and T.J. Afullo. Comparison of two methods to evaluate the log-normal raindrop size distribution model in durban. In *The Southern Africa Telecommunication Networks and Applications Conference (SATNAC)*, pages 2–5, 2012.

[83] A.R. Zainal, I.A. Glover, and P.A. Watson. Rain rate and drop size distribution measurements in Malaysia. In *Geoscience and Remote Sensing Symposium, 1993. IGARSS'93. Better Understanding of Earth Environment., International*, pages 309–311. IEEE, 1993.

[84] D. Motter, J.V. Lavarda, F.A. Dias, and S. Silva. Vibration energy harvesting using piezoelectric transducer and non-controlled rectifiers circuits. *Journal of the Brazilian Society of Mechanical Sciences and Engineering*, 34(SPE):378–385, 2012.

[85] V.J. Ovejas and A. Cuadras. Multimodal piezoelectric wind energy harvesters. *Smart Materials and Structures*, 20(8):085030, 2011.

[86] P. Gambier, S.R. Anton, N. Kong, A. Erturk, and D.J. Inman. Piezoelectric, solar and thermal energy harvesting for hybrid low-power generator systems with thin-film batteries. *Measurement Science and Technology*, 23 (1):015101, 2011.

[87] E. Lefeuvre, A. Badel, C. Richard, L. Petit, and D. Guyomar. A comparison between several vibration-powered piezoelectric generators for standalone systems. *Sensors and Actuators A: Physical*, 126(2):405–416, 2006.

[88] W.J. Wu, A.M. Wickenheiser, T. Reissman, and E. Garcia. Modeling and experimental verification of synchronized discharging techniques for boosting power harvesting from piezoelectric transducers. *Smart Materials and Structures*, 18(5):055012, 2009.

[89] S. Paquin and Y. St-Amant. Improving the performance of a piezoelectric energy harvester using a variable thickness beam. *Smart Materials and Structures*, 19(10):105020, 2010.

[90] A. Tabesh and L.G. Fréchette. A low-power stand-alone adaptive circuit for harvesting energy from a piezoelectric micropower generator. *IEEE Transactions on Industrial Electronics*, 57(3):840–849, 2010.

[91] S. Roundy, E.S. Leland, J. Baker, E. Carleton, E. Reilly, E. Lai, B. Otis, J.M. Rabaey, P.K. Wright, and V. Sundararajan. Improving power output for vibration-based energy scavengers. *IEEE Pervasive computing*, 4(1): 28–36, 2005.

[92] S. Roundy. On the effectiveness of vibration-based energy harvesting. *Journal of intelligent material systems and structures*, 16(10):809–823, 2005.

[93] C.K. Thein, B.L. Ooi, J.S. Liu, and J.M. Gilbert. Modelling and optimisation of a bimorph piezoelectric cantilever beam in an energy harvesting application. *J. Eng. Sci. Technol*, 11(2):212–227, 2016.

[94] Z.Z. Ong, V.K. Wong, and J.H. Ho. Performance enhancement of a piezoelectric rain energy harvester. *Sensors and Actuators A: Physical*, 252: 154–164, 2016.

[95] Y. Miao and Y. Jia. Hybrid decentralised energy for remote communities: Case studies and the analysis of the potential integration of rain energy. *Journal of Sustainable Development of Energy, Water and Environment Systems*, 2(3):243–258, 2014.

[96] R.G. Meadows. *Electric network analysis*. Burns & Oates, 1972.

[97] S. Zhu, B. Jiang, and W. Cao. Characterization of piezoelectric materials using ultrasonic and resonant techniques. In *Medical Imaging'98*, pages 154–162. International Society for Optics and Photonics, 1998.

[98] Y.P. Liu and D. Vasic. *Self-powered electronics for piezoelectric energy harvesting devices*. INTECH Open Access Publisher, 2012.

[99] M.J. Hasan, M.H. Islam, and Q. Tareq. High efficiency boost rectifier (bridgeless) for energy harvesting. *International Journal of Advanced Research in Electrical, Electronics and Instrumentation Engineering*, 3(10): 12288–12295, 2014.

[100] A. Emadi, A. Khaligh, Z. Nie, and Y.J. Lee. *Integrated power electronic converters and digital control*. CRC Press, 2009.

[101] Y. Liu, G. Tian, Y. Wang, J. Lin, Q. Zhang, and H.F. Hofmann. Active piezoelectric energy harvesting: general principle and experimental demonstration. *Journal of Intelligent Material Systems and Structures*, 20 (5):575–585, 2009.

[102] D. Porcarelli, D. Spenza, D. Brunelli, A. Cammarano, C. Petrioli, and L. Benini. Adaptive rectifier driven by power intake predictors for wind energy harvesting sensor networks. *IEEE Journal of Emerging and Selected Topics in Power Electronics*, 3(2):471–482, 2015.

[103] T. Kashiwao, I. Izadgoshasb, Y.Y. Lim, and M. Deguchi. Optimization of rectifier circuits for a vibration energy harvesting system using a macro-fiber composite piezoelectric element. *Microelectronics Journal*, 54:109–115, 2016.

[104] T.C. Banwell and A. Jayakumar. Exact analytical solution for current flow through diode with series resistance. *Electronics letters*, 36(4):291–292, 2000.

Appendix A

Device Specifications

A.1 Data logger (NI-USB6008)

General

Product Family: Multifunction DAQ

Measurement Type: Voltage

Form Factor: USB

Operating System / Target: Linux, Mac OS, Pocket PC, Windows

RoHS Compliant: Yes

Isolation Type: None

Analog Input

Single-Ended Channels: 8

Differential Channels: 4

Analog Input Resolution: 12 bits

Maximum Voltage Range: -10 V - 10 V

Accuracy: 7.73 mV

Minimum Voltage Range: -1 V - 1 V

Accuracy: 37.5 mV

Number of Ranges: 8

Simultaneous Sampling : No

On-Board Memory: 512 B

Analog Output

Number of Channels: 2

Resolution: 12 bits

Voltage Range: 0 V - 5 V

Accuracy: 7 mV

Update Rate: 150 S/s

Current Drive Single: 5 mA

Current Drive All: 10 mA

Digital I / O

Bidirectional Channels: 12

Input-Only Channels: 0

Output-Only Channels: 0

Timing: Software

Logic Levels: TTL

Programmable Input Filters: No

Supports Programmable Power-Up States: No

Digital Input

Input Type: Sinking Sourcing

Maximum Voltage Range: 0 V - 5 V

Digital Output

Output Type : Sinking Sourcing

Current Drive Single: 8.5 mA

Current Drive All: 102 mA

Maximum Voltage Range: 0 V - 5 V

Counters/ Timers

Watchdog Timer : No

Counters: 1

Buffered Operations: No

Debouncing /Glitch Removal: No

Max Source Frequency: 5 MHz

Pulse Generation: No

Size: 32 bits

Timebase Stability: 50 ppm

Logic Levels: TTL

Timing / Triggering / Synchronisation

Triggering: Digital

Synchronisation Bus(RTSI): No

Physical Specifications

Length: 8.51 cm

Width: 8.18 cm

Height: 2.31 cm

I/O Connector: Screw terminals

USB Power: Bus-Powered

A.2 Peristaltic pump (Cole Palmer-Masterex L/S series)

Output:

Speed: 600 rpm

Torque, Maximum: 180 oz-in (13 kg cm), 540 oz-in Starting

Input:

Operating Voltage/Frequency:

90-260 Vrms, 50/60 Hz, 2.2 A @ 115 Vrms, 1.1 A @ 230 Vrms

External Inputs:

START/STOP, CW/CCW, Contact closure

Remote/Local Speed Control Voltage input: 010V DC @ 10 kΩ

Accuracy: ±0.5 % Full Scale

Current input: 420 mA @ 250 Ω,

Accuracy: ±0.5 % Full Scale

Environment:

Operating Temperature: 32 to 104 °F (0 to 40 °C)

Storage Temperature: -13 to 149 °F (-25 to 65 °C)

Humidity: 10 % to 90 % non-condensing

Altitude: Less than 6562 ft (2000 m)

Pollution Degree: Pollution degree 2 (indoor uselab, office)

Construction:

Dimensions (L W H): 10.5 in 8 in 8 in (267 203 203 mm)

Weight: 6.9 kgs (15.2lbs)

Color: Light Grey (5 % Black)

Material: Aluminum, ABS plastic and vinyl

Enclosure Rating: IP33 per IEC-60529

A.3 Laser vibrometer(MicroEpsilon-ILD1700-10)

Measuring range: 10 mm

Start of measuring range: 30 mm

Midrange: 35 mm

End of measuring range: 40 mm

Linearity: 8 μm

FSO: 0.1 %

Resolution (at 2.5kHz without averaging): 0.5 μm

Measuring rate: 2.5 kHz / 1.25k Hz / 625 Hz / 312.5 Hz (adjustable)

Light source semiconductor laser: <1 mW, 670 nm (red)

Permissable ambient light (at 2.5 kHz): 10,000lx

Laser safety class: class 2 acc. DIN EN 60825-1 : 2008-05

Spot diameter:

-SMR:110 μm

-MMR:50 μm

-EMR: 110 μm

Temperature stability: 0.01 % FSO /°C

Operation temperature: 0 ...+50 °C

Storage temperature: -20 ... +70 °C

Measurements selectable: 4 ... 20 mA / 0 ... 10V / RS 422 / USB (optional with cable PC1700-3/USB)

Switching outputs: 1 x error or 2 x limit (each programmable)

Switch Input laser ON-OFF/zero

Operation: via touch screen on sensor or via PC with ILD 1700 tool

Power supply: 24 VDC (11 ... 30 VDC), max. 150 mA

Electromagnetic compatibility (EMC): EN 61000-6-3 EN 61000-6-2

Sensor cable length (with connector): 0.25 m

Synchronisation: possible for simultaneous or alternating measurements

Protection class: IP 65

Vibration: 2 g / 20 ... 500 Hz

Shock: 15 g / 6 ms

Weight (with 0.25 m cable): 550 g

A.4 Laser precipitation monitor sensor (Thies CLIMA-5.4110.10.000)

Meas. principle: laser beam

Particle size: 0.16 ... 8 mm

Particle speed: 0.2 ... 20 m/s

Intensity: < 0.005 ... > 250 mm/h

Accuracy with quantity meas.: < 15 % @ rain 0.5 ... 20 mm/h < 30 % @ snow

Precipitation types:

drizzle (also freezing), rain (also freezing), hail, snow, snow grains / ice needles, soft hail / ice grains

Accuracy, comparing with synoptic observation:

-drizzle > 97 %

-rain > 99 %

-hail > 95 %

-snow > 99 %

-snow grains > 60 %

Laser diode: 786 nm, max. 0.5 mW

Laser class: 1M (EN60825-1:1994 A2:2001)

Data output digital Interface: RS485 / 422, potential isolation and 2 impulse outputs, potential isolation

Baudrate: 1200 ... 115200 Baud

Output type: ASCII, Synop, Metar @ RS485 / 422, frequency @ impulse outputs

Resolution intensity: 0.001 mm/h @ RS485 / 422

Resolution quantity: 0,001 mm @ RS485 / 422, 0.1 mm, 0,01 mm, 0,005 mm @ impulse outputs

Ambient temp.: -40 ... +70 °C

Protection: IP 65

Dimension: ⌀ 270 x 170 x 540 mm

Weight: 4.8 kg

Appendix B

MATLAB code

```
%%%%%%%%%%%%%%%%%%%%%%%%%%%%%%%%%%%%%%%%%%%%%%%%%%%%%%%%%%%%%%%%%%%%%%%%%%%
% Program simulates the dynamical response of a piezoelectric cantilever  %
% beam due to single water droplet impinged in the tip of the beam     %
%%%%%%%%%%%%%%%%%%%%%%%%%%%%%%%%%%%%%%%%%%%%%%%%%%%%%%%%%%%%%%%%%%%%%%%%%%%

clear all
clc
ln = @(x)(log(x));

%%%%%%%%%%%%%%%%%%%%%%%%%%%
% --- Input Parameters
%%%%%%%%%%%%%%%%%%%%%%%%%%%
```

```
R = 15000;  %Load resistance

droplet_diameter = 2.96e-3; %Droplet diameter

droplet_mass = (4/3)*pi*1000*(droplet_diameter/2)^3;   %Water droplet mass

drop_height = 0.25; %drop height

constant = (3*0.796*1.2041)/(8*1000*droplet_diameter/2);

droplet_v = sqrt((9.81/constant)*(1-exp(-2*constant*drop_height))); %Impact vel

ca = 0; %Added mass coefficient

ee = 0.1923*exp(-21.94*ca) + 0.2773*exp(-0.4458*ca); %Impact coefficient


%%%%%%%%%%%%%%%%%%%%%%%%%%%%%%%%

% --- Time Constant Selection

%%%%%%%%%%%%%%%%%%%%%%%%%%%%%%%%


%Common Parameter

L2 = 46.355e-3;          %Lenght of cantilever beam

w = 38.1e-3;             %Width of cantilever beam

area = L2 * w;           %Surface area of cantilever beam


%Define FR4 Properties

hfr4=0.0762e-3;          %Thickness of FR4

density_fr4 = 1920;      %Density of FR4

cfr4 = 23.4e9;           %Young Modulus of FR4
```

```
%Define ESPANEX Properties

hesp = 0.0762e-3;       %Thickness of ESPANEX

hc = 0.0254e-3;         %Thickness of Copper

hsp = 0.0254e-3;        %Thickness of Polyimide

density_sc = 8960;      %Density of Copper

density_sp = 1430;      %Density of Polyimide

cesp = 4.5e9;           %Young Modulus of Copper

csp = 3.2e9;            %Young Modulus of polyimide


massofesp = (2*density_sc*hc*w) + (density_sp*hsp*w) ;

density_esp = massofesp/(w*hesp);


%Define Copper Properties

cc = 117e9;             %Young Modulus of Copper


%Define Peizoelectric Properties

hp = 0.127e-3;          %Thickness of the piezo

wp = 33.274e-3;         %Width of the piezo

Lp = 45.974e-3;         %Length of the piezo

a0 = 8.854*10^-12;      %epsilon, Electric constant

es33 = 830*a0;          %Dielectric constant

density_p = 7800;       %Density of piezo

y11e = 67e9;            %Young Modlus of piezo

d31 = -190e-12;         %Strain coefficient of piezo
```

```
%Define Eproxy Properties

Eproxy_layers = 4;

he = 0.7e-5;            %Thickness of Epoxy

density_e = 1250;       %Density of Epoxy

ce = 3.5e9;             %Young Modulus of Eproxy


%%%%%%%%%%%%%%%%%%%%%%%%%%%

% --- Constants

%%%%%%%%%%%%%%%%%%%%%%%%%%%


syms x real y z a b mm


%%%%%%%%%%%%%%%%%%%%%%%%%%%

% --- Mode Shape

%%%%%%%%%%%%%%%%%%%%%%%%%%%


%Eigenvalue of the first four modes

beta=[1.87510407 4.69409113 7.85475744 10.99554073]'./L2;


%Mode shape constant

sigma = [0.7340955 1.018467 0.999224497 1.0];


%Define Mode Shape
```

```
MODE_SHAPE = (sin(beta*x)-sinh(beta*x)).*(sin(beta*L2)-sinh(beta*L2))+ ...

(cos(beta*x)-cosh(beta*x)).*(cos(beta*L2)+cosh(beta*L2));


intmode = double(int(MODE_SHAPE.^2,x,0,L2));


%Discretise the mode shape

dl = 1/10000;


xnum = 0:dl:L2;

xnump = 0:dl:Lp;


%Mass per unit length of the nonpiezo and piezo layers

massperlength_np = (2*density_sc*hc*w) + (density_esp*hesp*w) +...

                   (2*density_fr4*hfr4*w) +(Eproxy_layers*he*density_e*w);

massperlength_p = (2*density_p*wp*hp);

massperlength_t = massperlength_p + massperlength_np ;

mode_n = 1; %% Mode number considered



disp('Computing Modal Parameters')


no(mode_n) = sqrt(1./(massperlength_t*intmode(mode_n)));

omode(mode_n) = no(mode_n).*MODE_SHAPE(mode_n);

PhiT(mode_n) = omode(mode_n).';
```

```
omodesdd(mode_n) = diff(diff(omode(mode_n),x),x);

PhiddT(mode_n) = omodesdd(mode_n).';


%%%%%%%%%%%%%%%%%%%%%%%%%%

% --- Mass Matrices

%%%%%%%%%%%%%%%%%%%%%%%%%%


buffer = PhiT(mode_n);


%--- Mass of EXPANEX


%Mass of ESPANEX_Polyimide


MSP = eval(int(w*density_sp* buffer.'*buffer ,y, (-hsp/2) , (hsp/2) ));

Msw = subs(MSP,xnum)';

MASS_ESPP(mode_n) = trapz(xnum,Msw);


%Mass of ESPANEX_Copper


uu = density_sc*hc*w;

buffer = subs(PhiT(mode_n),mm,uu);

h1 = (-hsp/2)-hc;

h2 = (-hsp/2);

h3 = (hsp/2);
```

```
h4 = (hsp/2)+hc;

MSC1 = eval(int(w*density_sc* buffer.'*buffer ,y, h1 , h2 ));

MSC2 = eval(int(w*density_sc* buffer.'*buffer ,y, h3 , h4 ));

MESP =  MSC1 + MSC2;

Msw = subs(MESP,xnum)';

MASS_ESPC(mode_n) = trapz(xnum,Msw);


%--- Mass of epoxy 1


h1 = (-hsp/2)-hc-he;

h2 = (-hsp/2)-hc;

h3 = (hsp/2)+hc;

h4 = (hsp/2)+hc+he;

ME1 = eval(int(w*density_e* buffer.'*buffer ,y, h1 , h2 ));

ME2 = eval(int(w*density_e* buffer.'*buffer ,y, h3 , h4 ));

ME = ME1 + ME2;

Msw=subs(ME,xnum)';

MASS_E1(mode_n)=trapz(xnum,Msw);


%--- Mass of Piezoelectric


h1 = (-hsp/2)-hc-he-hp;

h2 = (-hsp/2)-hc-he;

h3 = (hsp/2)+hc+he;
```

```
h4 = (hsp/2)+hc+he+hp;

MP1 = eval(int(wp*density_p* buffer.'*buffer ,y, h1 , h2 ));

MP2 = eval(int(wp*density_p* buffer.'*buffer ,y, h3 , h4 ));

MP = MP1 + MP2;

Msw = subs(MP,xnump)';

MASS_P(mode_n) = trapz(xnump,Msw);


%--- Mass of epoxy 2


h1 = (-hsp/2)-hc-he-hp-he;

h2 = (-hsp/2)-hc-he-hp;

h3 = (hsp/2)+hc+he+hp;

h4 = (hsp/2)+hc+he+hp+he;

ME1 = eval(int(w*density_e* buffer.'*buffer ,y, h1 , h2 ));

ME2 = eval(int(w*density_e* buffer.'*buffer ,y, h3 , h4 ));

ME = ME1 + ME2;

Msw=subs(ME,xnum)';

MASS_E2(mode_n)=trapz(xnum,Msw);

MASS_E(mode_n) = MASS_E1(mode_n) + MASS_E2(mode_n);


%--- Mass of Copper


h1 = (-hsp/2)-hc-he-hp-he-hc;

h2 = (-hsp/2)-hc-he-hp-he;
```

```
h3 = (hsp/2)+hc+he+hp+he;

h4 = (hsp/2)+hc+he+hp+he+hc;

MC1 = eval(int(w*density_sc* buffer.'*buffer ,y, h1 , h2 ));

MC2 = eval(int(w*density_sc* buffer.'*buffer ,y, h3 , h4 ));

MC = MC1 + MC2;

Msw = subs(MC,xnum)';

MASS_C(mode_n) = trapz(xnum,Msw);


%--- Mass of FR4


h1 = (-hsp/2)-hc-he-hp-he-hc-hfr4;

h2 = (-hsp/2)-hc-he-hp-he-hc;

h3 = (hsp/2)+hc+he+hp+he+hc;

h4 = (hsp/2)+hc+he+hp+he+hc+hfr4;

MFR41 = eval(int(w*density_fr4* buffer.'*buffer ,y, h1 , h2 ));

MFR42 = eval(int(w*density_fr4* buffer.'*buffer ,y, h3 , h4 ));

MFR4 = MFR41 + MFR42;

Msw = subs(MFR4,xnum)';

MASS_FR4(mode_n) = trapz(xnum,Msw);


%%%%%%%%%%%%%%%%%%%%%%%%%%

% --- Stiffness Matrices

%%%%%%%%%%%%%%%%%%%%%%%%%%
```

```
buffer = PhiddT(mode_n);


%--- Mass of ESPANEX


%Stiffness of ESPANEX_Polyimide


KSP = vpa(int(w*csp*y^2* buffer.'*buffer ,y, (-hsp/2), (hsp/2) ));

Ksw = subs(KSP,xnum)';

STIFFNESS_ESPP(mode_n) = trapz(xnum,Ksw);


%Stiffness of ESPANEX_Copper


h1 = (-hsp/2)-hc;

h2 = (-hsp/2);

h3 = (hsp/2);

h4 = (hsp/2)+hc;

KSC1 = eval(int(w*cc*y^2* buffer.'*buffer ,y, h1 , h2 ));

KSC2 = eval(int(w*cc*y^2* buffer.'*buffer ,y, h3 , h4 ));

KESP = KSC1 + KSC2;

Ksw = subs(KESP,xnum)';

STIFFNESS_ESPC(mode_n) = trapz(xnum,Ksw);


%---Stiffness of Epoxy 1
```

```
h1 = (-hsp/2)-hc-he;

h2 = (-hsp/2)-hc;

h3 = (hsp/2)+hc;

h4 = (hsp/2)+hc+he;

KP1 = vpa(int(w*ce*(y^2)* buffer.'*buffer ,y, h1, h2 ));

KP2 = vpa(int(w*ce*(y^2)* buffer.'*buffer ,y, h3, h4 ));

KP = KP1 + KP2;

Ksw=subs(KP,xnum)';

STIFFNESS_E1(mode_n)=trapz(xnum,Ksw);


%--- Stiffness of Piezo


h1 = (-hsp/2)-hc-he-hp;

h2 = (-hsp/2)-hc-he;

h3 = (hsp/2)+hc+he;

h4 = (hsp/2)+hc+he+hp;

KP1 = vpa(int(wp*y11e*(y^2)* buffer.'*buffer ,y, h1, h2 ));

KP2 = vpa(int(wp*y11e*(y^2)* buffer.'*buffer ,y, h3, h4 ));

KP = KP1 + KP2;

Ksw = subs(KP,xnump)';

STIFFNESS_P(mode_n) = trapz(xnump,Ksw);
```

```
%--- Stiffness of Epoxy 2


h1 = (-hsp/2)-hc-he-hp-he;

h2 = (-hsp/2)-hc-he-hp;

h3 = (hsp/2)+hc+he+hp;

h4 = (hsp/2)+hc+he+hp+he;

KP1 = vpa(int(w*ce*(y^2)* buffer.'*buffer ,y, h1, h2 ));

KP2 = vpa(int(w*ce*(y^2)* buffer.'*buffer ,y, h3, h4 ));

KP = KP1 + KP2;

Ksw=subs(KP,xnump)';

STIFFNESS_E2(mode_n)=trapz(xnump,Ksw);

STIFFNESS_E(mode_n) = STIFFNESS_E1(mode_n) + ...

                      STIFFNESS_E2(mode_n) ;


%--- Stiffness of Copper


h1 = (-hsp/2)-hc-he-hp-he-hc;

h2 = (-hsp/2)-hc-he-hp-he;

h3 = (hsp/2)+hc+he+hp+he;

h4 = (hsp/2)+hc+he+hp+he+hc;

KC1 = vpa(int(w*cc*(y^2)* buffer.'*buffer ,y, h1, h2 ));

KC2 = vpa(int(w*cc*(y^2)* buffer.'*buffer ,y, h3, h4 ));

KC = KC1 + KC2;

Ksw = subs(KC,xnum)';
```

```
STIFFNESS_C(mode_n) = trapz(xnum,Ksw);


%--- Stiffness of FR4


h1 = (-hsp/2)-hc-he-hp-he-hc-hfr4;

h2 = (-hsp/2)-hc-he-hp-he-hc;

h3 = (hsp/2)+hc+he+hp+he+hc;

h4 = (hsp/2)+hc+he+hp+he+hc+hfr4;

KFR41 = vpa(int(w*cfr4*(y^2)* buffer.'*buffer ,y, h1, h2 ));

KFR42 = vpa(int(w*cfr4*(y^2)* buffer.'*buffer ,y, h3, h4 ));

KFR4 = KFR41 + KFR42;

Ksw = subs(KFR4,xnum)';

STIFFNESS_FR4(mode_n) = trapz(xnum,Ksw);


%%%%%%%%%%%%%%%%%%%%%%%%%%

% Modal parameters summary

%%%%%%%%%%%%%%%%%%%%%%%%%%


%Modal mass

MASS(mode_n) = MASS_ESPP(mode_n) + MASS_ESPC(mode_n) + ...

    MASS_FR4(mode_n) + MASS_C(mode_n) + MASS_P(mode_n) + ...

    MASS_E(mode_n)


%Inclusive of water layer
```

```
MASS = (1+ca)*MASS


%Modal stiffness

STIFFNESS(mode_n) = STIFFNESS_ESPP(mode_n) + ...

    STIFFNESS_ESPC(mode_n) + STIFFNESS_FR4(mode_n) + ...

    STIFFNESS_C(mode_n) + STIFFNESS_P(mode_n) + ...

    STIFFNESS_E(mode_n)


%%%%%%%%%%%%%%%%%%%%%%%%%%

% --- Coupling Matrix

%%%%%%%%%%%%%%%%%%%%%%%%%%


buffer = PhiddT(mode_n);


%Two layers of piezo

C1 = vpa(int(-y *wp*y11e*d31*(1/hp) *buffer.',y, (-hesp/2)-he-hp ,(-hesp/2)-he

C2 = C1;

C = C1 + C2;

T=subs(C,xnump);

COUPLING(mode_n)=trapz(xnump,T);


%Separate to two single layer

COUPLING(mode_n) = COUPLING(mode_n)/2
```

```
%%%%%%%%%%%%%%%%%%%%%%%%%%

% --- Capacitance Matrix

%%%%%%%%%%%%%%%%%%%%%%%%%%


CAPACITANCE(mode_n) = -2*wp*Lp*es33/hp;


%Separate to two single layer

CAPACITANCE(mode_n) = CAPACITANCE(mode_n)/2


%%%%%%%%%%%%%%%%%%%%%%%%%%

% --- Damping Matrix

%%%%%%%%%%%%%%%%%%%%%%%%%%


drr = 0.012;    %Damping ratio

DAMPING = 2*(drr)*sqrt(MASS*STIFFNESS);


disp('Generating Results')


%%%%%%%%%%%%%%%%%%%%%%%%%%

% --- Forcing Term (droplet)

%%%%%%%%%%%%%%%%%%%%%%%%%%


position = L2;    %Impact position

buffer = PhiT(mode_n);
```

```
summode=subs(buffer,x,position);

tau = droplet_diameter/droplet_v;   %Impact duration

ff =  (droplet_mass*droplet_v)/(tau);

TOTAL_FORCE(mode_n) = -(1-ee)*summode*ff;   %Average impact force

Minv = inv(MASS);

STIFFNESSs = STIFFNESS;

DAMPINGs = DAMPING;

DAMPINGs = (round(DAMPINGs*1000)/1000);

COUPLINGs = COUPLING;

CAPACITANCEs = CAPACITANCE;

TOTAL_FORCEs = TOTAL_FORCE;


%State space model


A = [0 1 0 0; ...

     -(STIFFNESSs*Minv) -(DAMPINGs*Minv) -Minv*COUPLINGs -Minv*COUPLINGs;...

     0 -COUPLINGs'/CAPACITANCEs 1/(R*CAPACITANCEs) 0;...

     0 -COUPLINGs'/CAPACITANCEs 0 1/(R*CAPACITANCEs)];

B = [0 ; Minv*TOTAL_FORCEs ; 0 ; 0];

C = [0 0 1 1];

D = 0;

SYS = ss(A,B,C,D);
```

```
%%%%%%%%%%%%%%%%%%%%%%%%%%%%%%%%

% --- Single droplet excitation

%%%%%%%%%%%%%%%%%%%%%%%%%%%%%%%%


time_max = 0.3;

dt = 1/2500;

t = 0:dt:time_max;

time = 1;

[AA BB] = size(t) ;

BB = BB+1;


while time < BB

    if t(time)<tau

    nu(time) = 1;

    else

        nu(time)=0;

    end

    time = time + 1;

end


Voltage =  lsim(SYS,nu,t);

plot(t,Voltage)
```

Appendix C

Actual rain voltage graphs

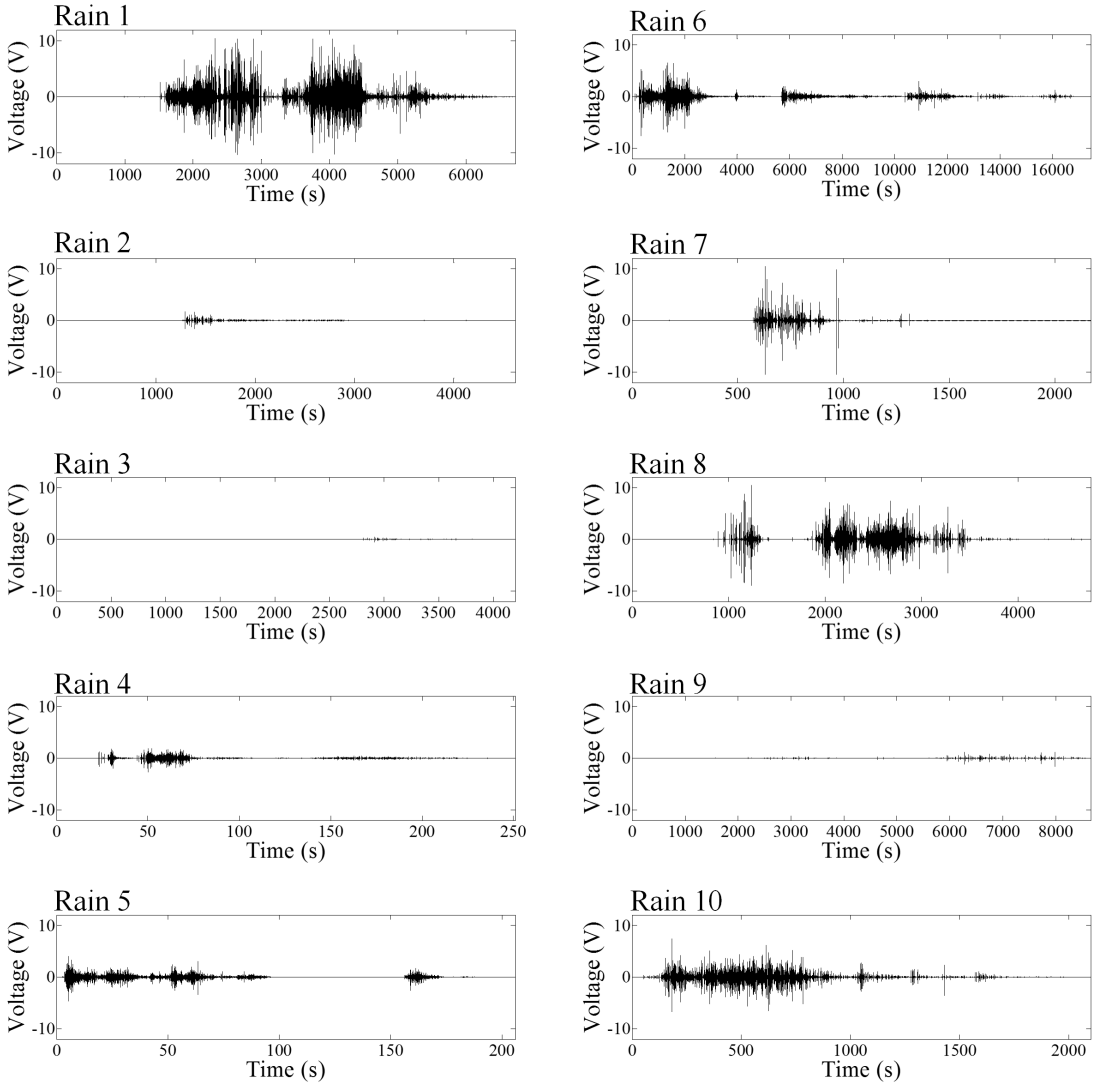


Figure C.1: Voltage time response graphs recorded from 10 actual rains